Magnetism in $Ni_{80}Fe_{20}$ and $Ni_{80}Fe_{20}$/NiO Nano-stripes

by

Mueed Ahmad Mirza

A thesis submitted to the Faculty of Graduate Studies of

The University of Manitoba

in partial fulfilment of the requirements of the degree of

Master of Science

Department of Physics and Astronomy

University of Manitoba

Winnipeg

Abstract

$Ni_{80}Fe_{20}$ and $Ni_{80}Fe_{20}$/NiO films and nano-stripes were characterized magnetically through AC and DC susceptibility measurements, and hysteresis loops as a function of field and temperature. While the near-pattern films were characterized in the in-plane configuration only, the nano-stripes were characterized in parallel, transverse and the perpendicular field configurations. The effects of the constrained geometry on the coercivity, exchange bias field, and the superparamagnetic blocking temperature were studied. It was determined that the coercivity, exchange bias field and the superparamagnetic blocking temperature can be controlled, not only by using a patterned media instead of a plane film, but also by the orientation of that pattern.

Acknowledgements

Upon the completion of this thesis, I have a deep feeling of gratitude for all those who helped me directly or indirectly. It would have been very hard, if not impossible without their timely and untiring help.

I would like to extend my deep gratitude to my supervisor Johan van Lierop who deserves the lion's share of the credit for the successful completion of this. I would also like to thank Dr. Sharma who took a personal interest in my progress. I would like to thank my thesis committee members Dr. John Page and Dr. Cyrus Shafai for taking their valuable time to go through my thesis and helping me finish my thesis through their suggestions. Susan, Renée and Wanda, made the amazingly efficient administrative staff, and always helped me in an accurate and timely manner. Gilles, the knowledge database, who knew everything from the MPMS to the o-ring of the vacuum pump, was just amazing and always ready to guide. My colleagues Ryan, Liz and Resta, made me feel comfortable in the lab and the office and always provided me with guidance and support.

I want to express my deep appreciation for my friends Dr. Afzal, Atif, Bashir, Imran, and Khalid who guided and helped me a lot to get settled in this new country with a whole new environment. Life would have been really hard without their selfless support. Thanks also go to my parents, brother and sister, who always remembered me in their prayers and encouraged me a lot. I would like to express my deep appreciation and gratitude for my wife Mahpara who has always been by my side during the toughest times.

Mueed Ahmad Mirza

May 2012

Dedicated to

Johan, Afia & Mahmud

who helped the evolution of my knowledge in Physics

Table of Contents

Table of Tables

Table of Figures

Chapter One: Introduction to the Thesis

The never-ending efforts for smaller devices with greater storage and computation capabilities have been fuelling progress in device miniaturization. The reduced dimensionality of a magnetic system can result in magnetic properties different from the bulk. Advanced fabrication technologies have made it possible to prepare magnetic microstructures and nanostructures with well defined geometries. The study of nanostructured magnetic materials has seen a tremendous amount of effort being put in this field over the last few decades.

Nanoscience deals with the study of phenomena related to objects of dimensions in the range from 1 to 100 nm. Molecules, viruses, integrated circuit components and the grains in magnetic-recording film media are examples of objects with these sizes [1]. The study of the magnetic properties of objects with at least one dimension in a nanoscale range is termed nanomagnetism. The scope of nanomagnetism spans the magnetism of zero-dimension (nano-dots), one dimension (nano-wires and nano-rods), two dimension (thin films) and three dimension (nano-particles) nano-size objects as well as macroscopic systems that contain nanoscopic objects [1].

Many materials, e.g. Permalloy, have had their magnetic properties studied exhaustively in their bulk form. However, the advent of nanomagnetism has opened a whole new area of research in these materials at the nanoscale. In this project, polycrystalline $Ni_{80}Fe_{20}$ thin film and nano-stripes were studied, and $Ni_{80}Fe_{20}$ coupled to NiO in the form of a thin film and nano-stripes was also studied to examine the exchange coupling effects in addition to coupling effects between the stripes.

1.1 Magnetism in $Ni_{80}Fe_{20}$ and NiO

The two types of magnetism which are of significance for this work are ferromagnetism and antiferromagnetism. $Ni_{80}Fe_{20}$ is a ferromagnet while NiO is an antiferromagnet.

In antiferromagnetic (AFM) materials, the nearest neighbour magnetic ions align favourably their moments anti-parallel to one another. This type of magnetism is usually found in the systems that can be considered to be two interpenetrating sublattices with moments pointing in opposite directions. Superexchange is responsible for antiferromagnetism in NiO, illustrated in Fig. 1.1. Nickel has an atomic number 28, hence Ni^{+2} in NiO has 8 *d* electrons. The nickel atoms in NiO are arranged in an octahedral coordination and the five degenerate *d* orbitals split under the influence of the crystal field. Three orbitals d_{xy}, d_{yz} and d_{zx} are low energy orbitals because they point 45º from the adjacent oxygen atoms and are known as t_{2g} orbitals. Two orbitals d_{z^2} and $d_{x^2-y^2}$ are high energy orbitals as they point towards the adjacent oxygen atoms and are known as e_g orbitals. Both e_g orbitals contain one electron each. The $d_{x^2-y^2}$ electron interacts covalently with the electron with opposite spin in the *p* orbital of neighbouring oxygen ions. Since the electrons in the *p* orbital of oxygen have opposite spins, their interaction

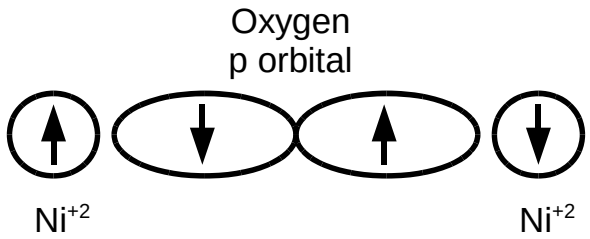

Figure 1.1: Antiferromagnetic spin alignment as a result of superexchange in NiO

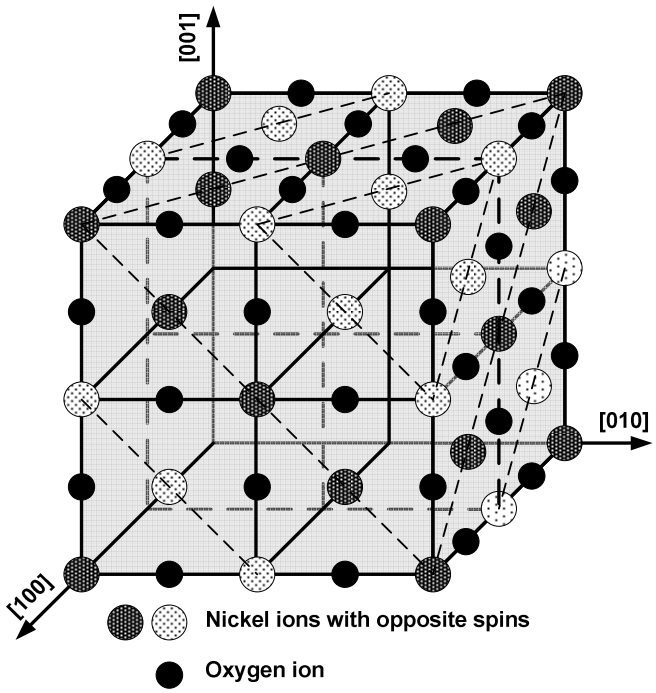

Figure 1.2: Antiferromagnetic structure of NiO. Ions on the three faces only are shown for the sake of clarity

with $d_{x^2-y^2}$ electrons of nickel ions at both sides results in the antiferromagnetic alignment of the spins of the nickel ions [3]. Above a certain material-specific temperature, the Néel temperature (Fig. 1.3), this ordering is lost and the material undergoes a transition from AFM to paramagnetic (PM) where thermal energy destroys the magnetic ordering by overcoming exchange interaction.

It is now well known that ferromagnetism (FM) is governed mainly by two contributions; quantum mechanical exchange interactions and conduction electrons, depending on the system. $Ni_{80}Fe_{20}$ is a 3d ferromagnet [4], like its constituents nickel and iron. In $Ni_{80}Fe_{20}$, the 3d electrons form a band structure with the 4s electrons and are

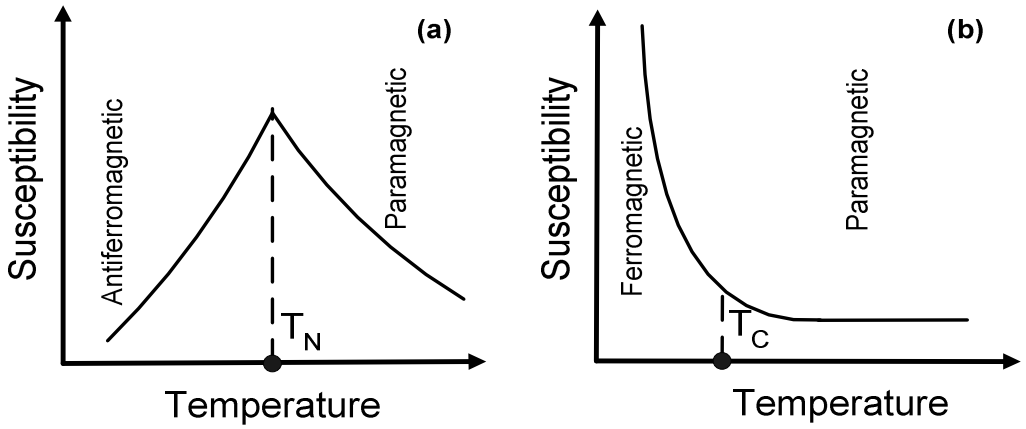

Figure 1.3: Low field magnetic susceptibility (magnetization/field) as a function of temperature showing (a) Néel temperature (T_N) and (b) Curie temperature (T_C)

responsible for the magnetism [5]. Iron and nickel have incomplete 3d shells. Due to strong crystal field interaction, the orbital momentum is quenched and hence only the spins are responsible for the ferromagnetism. The 3d electrons in nickel and iron are itinerant and the reason behind the ferromagnetic behaviour of $Ni_{80}Fe_{20}$. The FM materials undergo a transition from FM to PM above a material-specific temperature known as Curie temperature (Fig. 1.3).

Magnetic hysteresis is an important property of ferromagnetic materials and is characterized by the magnetization vs field (M vs H) curve. A typical hysteresis loop is shown in Fig. 1.4. The saturation magnetization is the maximum possible magnetization of a specimen. The remnant magnetization is the remaining magnetization of the specimen at zero field after it has been saturated magnetically. The coercivity is the magnetic field required to nullify the magnetization of the specimen. Ideally, a hysteresis loop is symmetric about the magnetization axis and hence coercivity is $(H_{C1}-H_{C2})/2 = H_{C1} = -H_{C2} = H_C$.

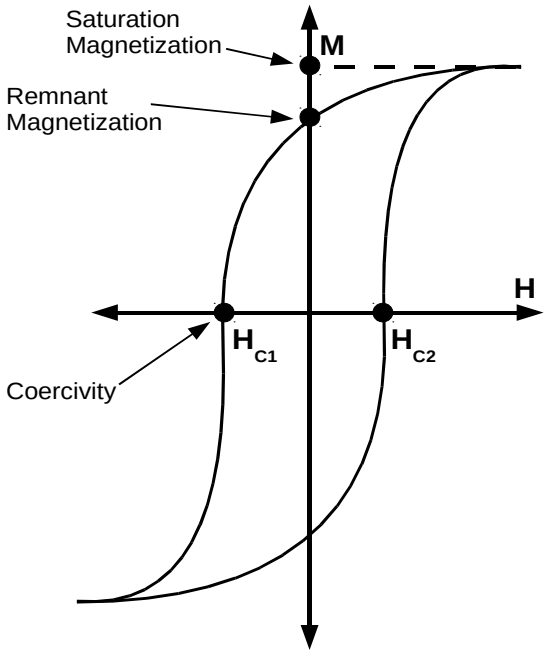

Figure 1.4: A typical hysteresis loop

In the case of FM/AFM layers, after cooling the material from a temperature higher than the Néel temperature in a field large enough to saturate the ferromagnetic material, the hysteresis loop is often not symmetric, but displaced along the applied field axis as shown in Fig. 1.5. This shift in the hysteresis loop along the applied field axis with respect to the zero field is called the exchange bias (H_{EX}) field and defined as $H_{EX}=(H_{C1}+H_{C2})/2$. It arises as a result of an interaction through the interfaces between the materials of different magnetic nature, e.g. a ferromagnet and antiferromagnet. The exchange bias field is described by [6]

$$H_{EX} = \frac{2J_{EX}\,\overline{S}_{FM}\cdot\overline{S}_{AFM}}{a_{FM}^{2} M_{FM} t_{FM}}$$

where $\overline{S}_{FM}$ and $\overline{S}_{AFM}$ are the spins of atoms at the FM/AFM interface and a_{FM} is the cubic lattice parameter of FM layer. M_{FM} is magnetization density of the FM layer while

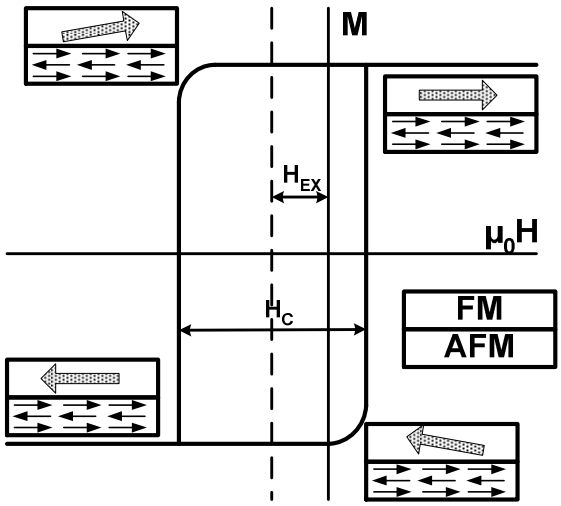

Figure 1.5: Behaviour of the magnetic moments of an exchanged bias system at different stages in the hysteresis loop

t_{FM} is the thickness of FM layer. J_{EX} is the interface coupling constant. This interaction modifies the behaviour of the ferromagnet in the presence of an applied field and hence a shift in the hysteresis loop is observed [1]. Figure 1.5 shows a schematic of a hysteresis loop for an exchange biased system. At the start (a) the sample is saturated. At (b) FM moments are inclined to follow the applied magnetic field but the moments in AFM layer exert a torque and hence offer resistance to magnetization reversal. An obvious result of this force is a shift in the loop towards a negative field.

Magnetic hysteresis appears as a result of rotation of magnetization and change in the number of domains. Magnetic domains are the small regions with moments aligned in the same direction. Normally ferromagnets are divided into domains aligned in different directions. The process and extent of domain formation is governed by the balance of the contribution of different energy terms.

1.2 Energetics at the nano-scale

A ferromagnetic system will be in equilibrium at its minimum total energy. The total energy, according to micromagnetic theory, is the sum of four main energies. These four energies are the Zeeman energy, the exchange energy, the stray field energy, and the anisotropy energy [1].

If a magnetized sample is moved from a zero external field into a magnetic field $\mu_o H$, some work needs to be done to keep the magnetization constant. The work required is called the Zeeman energy and given by

$$E_{ZEEMAN} = -\int_V \mu_0 \overline{M} \cdot \overline{H} dV$$

where $\overline{M}$ is the macroscopic magnetization of the sample, $\overline{H}$ is the applied field and V is the volume [7]. The Zeeman energy is at its minimum when the magnetization is aligned with the applied magnetic field as evident from the dot product in above relation.

In a typical ferromagnetic material, the moments prefer to keep aligned in the equilibrium magnetization direction and hence parallel alignment of neighbouring spins is preferred. Deviation from this ideal situation will cost energy which is known as exchange energy and is defined as

$$E_{EXCHANGE} = A \int \left(grad\ \overline{m} \right)^2 dV$$

where A is the exchange stiffness constant and $\overline{m}$ is the normalized magnetization $\overline{m} = \overline{M} / M_S$ [7].

Stray field energy is also known as magnetostatic energy, dipolar energy or demagnetization field energy [1], [7]. It is related to the field generated by the body itself.

The divergence of the magnetization results in this field, known as the demagnetizing field $\overline{H_d}$. The stray field energy is defined as [1]

$$E_{STRAY-FIELD} = -\frac{1}{2}\mu_0 \int_V \overline{H_d} \cdot \overline{M} dV$$

For almost every magnetic material, the energy of its magnetization state depends on the difference in the direction of the magnetization in an applied field and the preferential direction called the easy axis. The degree of this anisotropy is defined by the magnetocrystalline anisotropy.

Magnetocrystalline anisotropy results in hard and easy axes of magnetization in a single-crystal. It stems from the spin orbit interaction of the electrons. The electron orbitals are coupled to the crystal by the crystal field. So the interaction between these orbitals and electronic spins results in a preferential direction of spin alignment along certain crystallographic axes [8, 9]. The magnitude of the anisotropy constants, e.g. K_1, determines the strength of magnetocrystalline anisotropy. For $Ni_{80}Fe_{20}$, K is 270 J/m

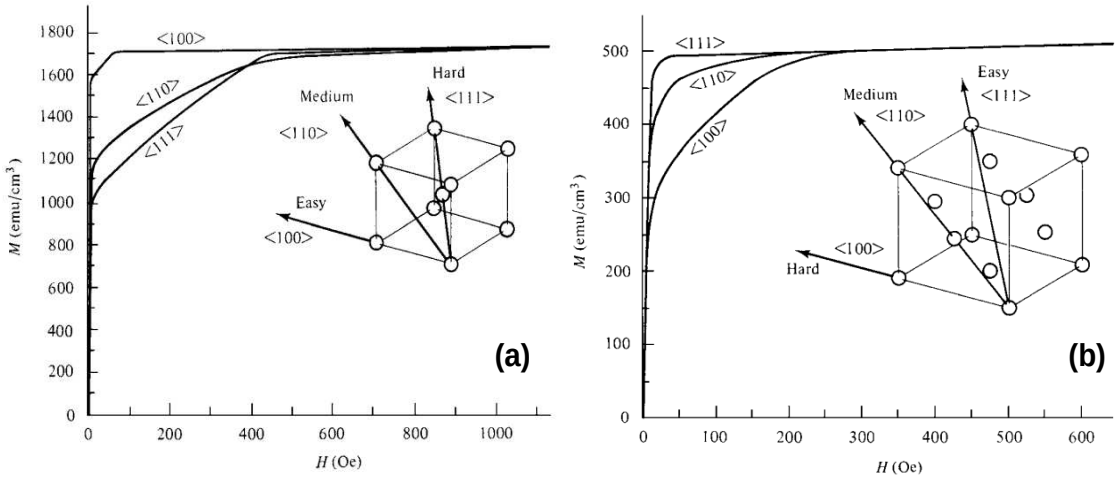

Figure 1.6: Magnetization curves of (a) iron and (b) nickel single crystals (used with permission from John Wiley & Sons, USA) [8]

= 2.7×10^3 erg/cm^3 [1]. Figure 1.6 shows the magnetization vs field curves for iron and nickel single crystals with crystal axes shown in the insets. The value of K is 4.8×10^4 J/m = 4.8×10^5 erg/cm^3 for iron and -4.5×10^3 J/m = -4.5×10^4 erg/cm^3 for nickel at room temperature [10]. For positive K, easy axes are along lattice axes while negative K implies the easy axes along the cube diagonals.

Surface anisotropy is caused by broken translation symmetry at the surface or an interface. The surface anisotropy is described by

$$E_S = K_S\left(1-\left(\bar{m}\cdot\bar{n}\right)^2\right)$$

where K_S represents the out of plane surface anisotropy constant and has the values in the range 10^{-3} to 10^{-4} J/m^2 or 10^{-6} to 10^{-7} erg/cm^2. $\bar{m}$ is normalized magnetization and $\bar{n}$ is surface normal [7].

It will be appropriate to discuss the characteristic lengths in the thin films before proceeding with a detailed overview of the different types of domains.

1.3 Characteristic length scales

The novel phenomena related to the field of nanomagnetism emerge because magnetism in nanoscopic objects is different from that in macroscopic objects. Nanoscopic objects have the dimensions comparable to the characteristic lengths, e.g. domain size. The surface-to-volume ratio is exceptionally high when we move from the macroscopic regime to the nanoscopic one. Due to the nanoscale dimensions, the presence of imperfections and defects becomes more important compared to macro-sized objects. These factors drive the magnetism at the nanoscale. The length scales relevant to

this work are the exchange length, the domain wall width, and the critical diameter of a single domain.

The exchange length is the minimum length scale over which the direction of the magnetization undergoes no appreciable variation [12]. The exchange length determines the distance range of spin alignment. It represents the characteristic length scale below which the division of the long range order into domains is not energetically favourable for the system [13]. The exchange length l_{ex} is [1]

$$l_{ex} = \sqrt{\frac{2A}{\mu_0 M_S^2}}$$

where

$A =$ Exchange stiffness constant. It represents the strength of the magnetic coupling and hence determines the difficulty for the deviation of a given spin from the direction of the exchange field [1]

$\mu_0 =$ Magnetic permeability of the free space = $4\pi \times 10^{-7}$ H/m

$M_S =$ Saturation magnetization.

Another important characteristic length is the domain wall that is defined as the

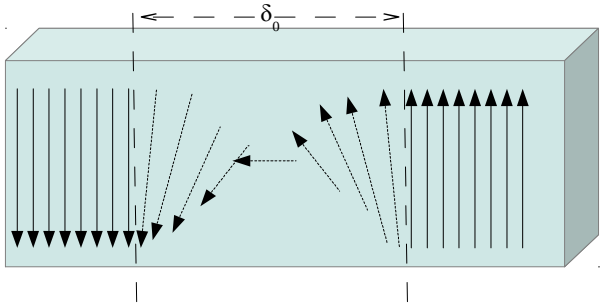

Figure 1.7: Domain wall width (δ_0)

region between two neighbouring domains. The magnetization changes direction from one easy crystallographic axis to another at or within the domain wall [8]. The domain wall width (Fig. 1.7), δ_0, can be determined from the relation [1]

$$\delta_0 = \pi\sqrt{\frac{A}{K}}$$

where K is uniaxial anisotropy energy.

The critical diameter is the maximum size of the object to be in a single domain configuration. Beyond this size, division of the object into different domains is energetically favourable. For magnetically soft materials (i.e. with low K) like $Ni_{80}Fe_{20}$, the critical radius is given by [14]

$$R_C \approx 2.121\sqrt{\frac{A}{2\pi M_S^2}}$$

For $Ni_{80}Fe_{20}$, $A = 1.07\times10^{-11}$ J/m $= 1.07\times10^{-6}$ erg/cm and $M_S = 8.13\times10^{-5}$ A/m $= 813$ emu/cm^3. Substituting the values in above relation, we get $R_C \approx 10.8$ nm. So the critical diameter is $D_C = 21.6$ nm.

1.4 Domain walls in thin films

The Bloch wall, Néel wall and the cross tie wall are the three common types of domain walls in thin films. In a Bloch wall (Fig. 1.8a), the magnetization rotates in a plane parallel to the plane of the wall. For a film with thickness beyond a critical limit, Bloch walls are energetically more favourable. However, in the case of thin films where the exchange length is large compared to the film thickness, Néel walls (Fig. 1.8b) are energetically more favourable in which the magnetization rotates in a plane perpendicular to the plane of the wall [1]. A cross tie wall (1.8c) is a combination of the Bloch and the

Néel walls. It appears in thin films with the thickness range between those energetically favourable for Bloch and Néel walls.

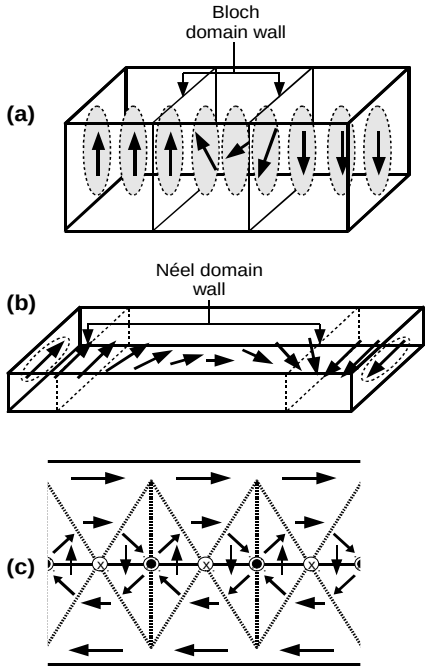

Figure 1.8: The (a) Bloch (b) Néel and the (c) cross-tie domain walls

The presence of domains can result in an overall zero or negligible magnetization. The balance of the contribution of different energy terms is the basic reason behind the division of a ferromagnetic material into domains. An increase in the number of domains results in low magnetostatic energy of the system, however, this can not continue indefinitely. The region of transition between the two neighbouring domains, i.e. the domain wall, is a region with high energy and hence causes an increase in the exchange and anisotropy energy [1].

1.5 An Overview of Previous Work in $Ni_{80}Fe_{20}$ and NiO Film Systems

As this work focuses on the magnetic behaviour of nano-stripes and thin films made of $Ni_{80}Fe_{20}$ and NiO, it will be appropriate to discuss previous work in this area. The nano-stripes can present different magnetic behaviour because of the related shape anisotropy and the size constraints. A multi-phase magnetization reversal can result from the stripes of different material or sizes coupled together. McCord et al. [14] studied the magnetization reversal in alternately occurring $Ni_{81}Fe_{19}$ and Cr^{+} ion implanted $Ni_{81}Fe_{19}$ stripes; both types of stripes being 1μm wide. The hysteresis loop showed that the magnetization reversal was a two phase process. The magnetization reversal, studied by magneto-optical domain imaging, appeared to occur through a head-on domain wall motion along the stripe axis in which domain alignment started from one end of the stripe and grew in the direction of the magnetic field. Fassbender et al. [16] showed that, for alternately occurring $Ni_{81}Fe_{19}$ and Cr ion implanted $Ni_{81}Fe_{19}$ stripes each of width 10 μm, a multi-domain structure appeared during magnetization reversal. However, this was not the case for the stripes of width 1 μm where the switching process parallel to the stripe direction proceeded via head-on domain wall movement. Adeyeye et al. [17] observed a two-phase magnetization reversal behaviour in the hysteresis loop while studying alternating 2 μm wide stripes of $Ni_{80}Fe_{20}$ and cobalt of thickness 20 nm and 40 nm respectively. Goolaup et al. [18] studied the effect of homogeneity of stripe width on the magnetization reversal. They found that the easy axis hysteresis loop showed a two phase behaviour for the alternating width (w) nano-wires (Δw = 250 nm) while for the stripes with the same width, the hysteresis loop showed a single phase behaviour. The edge-to-edge distance between the nano-wires in both cases was 70 nm. They also found that an

increase in the thickness of the wires from 20 nm to 60 nm resulted in an increase in the coercivity. Theis-Brohl et al. [19] have reported a two-phase magnetization behaviour in the case of $Co_{70}Fe_{30}/Mn_{83}Ir_{17}/Cu$ with alternating stripes bombarded with He^{+} ions. Figure 1.9 shows a two phase hysteresis loop for $Ni_{80}Fe_{20}$ nano-stripes with the applied

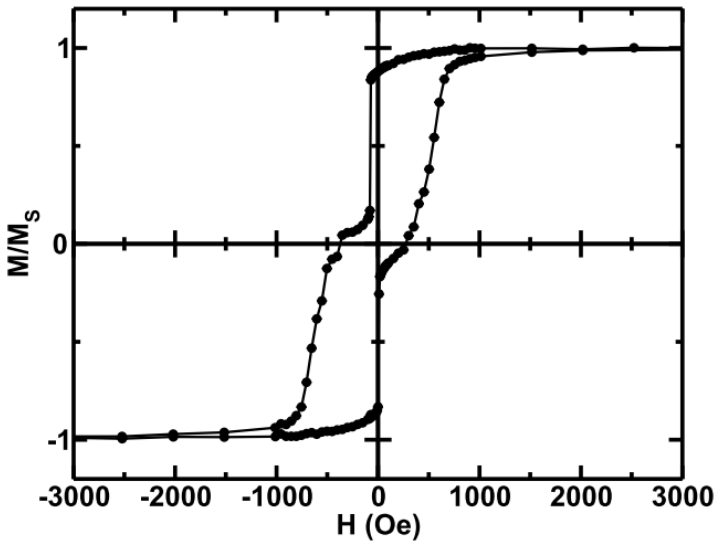

Figure 1.9: Normalized hysteresis loop for $Ni_{80}Fe_{20}$ nano-stripes at 10 K with magnetic field applied along the axes of the stripes (error bars are smaller than the symbols)

field along the stripes axes. The two phase behaviour of the hysteresis loop appeared because of the existence of patterned and un-patterned regions in the sample. The existence of stripes resulted in an enhanced coercivity, in case of the magnetic field applied along the easy axis of magnetization, as compared to the unpatterned material which is reported by several groups [18-31].

An interesting phenomenon is the existence of exchange bias in the $Ni_{80}Fe_{20}$ thin films. As the thickness of the film is reduced to a certain limit, surface effects become significantly prominent and important. Surface magnetization is obviously different from the bulk and hence acts as a source of exchange bias in the $Ni_{80}Fe_{20}$ thin film [34, 35].

Exchange bias in the $Ni_{80}Fe_{20}$/NiO bilayers emerges from the exchange interaction at the interface of the two layers [36-38]. Zhao et al. [39] showed that, in the case of the $Ni_{80}Fe_{20}$/NiO bilayers, the uncompensated spins are essential for the appearance of the exchange bias. However the theory by Meiklejohn and Beans [40] explaining the exchange bias on the basis of uncompensated spins fails because the exchange coupling exists for the compensated spins as well. This fact along with the order of magnitude too small exchange bias field than the expected value from calculation by Malozemoff [41, 42] indicated the importance of the AFM domain formation [43]. Attempts were made to explain the exchange bias by proposing domains perpendicular and parallel to the interface. The existence of exchange coupling at FM/AFM interface shows that these AFM domains affect the formation of the domains in the FM.

Mauri et al. [43] studied the relation between the exchange bias and the AFM layer thickness. For a thickness less than a critical value, the anisotropy energy of the AFM was small and the AFM magnetization at the interface just followed the FM magnetization. It resulted in an enhanced coercivity; however no exchange bias was seen. The interfacial exchange energy was overcome by the anisotropy energy above the critical thickness. This resulted in stable AFM magnetization at the interface which, in turn, caused the exchange bias. An increase in the layer thickness resulted in an increase

in the number of domain walls which played a major role in determining the exchange bias. With a further increase in the thickness there came a point where it was more favourable for the AFM layer to have larger and fewer domains. This resulted in the decrease in the exchange bias.

There are contradicting reports about the effect of lateral size reduction on the exchange bias field as compared to the plane film. While some groups [44-46] claim an enhancement in the exchange bias field in the stripes as compared to the thin films, some others [47, 48] report otherwise. Nemoto et al. [49] showed for $Ni_{81}Fe_{19}$/NiO wires of widths from 0.2 μm to 0.4 μm that the exchange bias field increased with the decrease in the wire width. However, Fraune et al. [47] have shown an increase in the exchange bias field with an increase in the wire width at room temperature. While at 5 K, the exchange bias field was independent of the wire width.

The emergence of the exchange bias is influenced significantly by the magnetic field applied during the field cooling as this field establishes a strong unidirectional anisotropy [50], however exchange bias can appear even without applying an external field because of the magnetization of the FM layer [51].

1.6 Why $Ni_{80}Fe_{20}$ and $Ni_{80}Fe_{20}$/NiO thin film and nano-stripes?

As a part of this project, polycrystalline $Ni_{80}Fe_{20}$ thin films and nano-stripes were studied alone and coupled to NiO. $Ni_{80}Fe_{20}$ is a material of industrial and research importance and has been extensively studied because of its low coercivity, high magnetic susceptibility, low remagnetization losses, low magnetostriction and high anisotropic magnetoresistance [52, 53]. The high Néel temperature (525 K) [54] of NiO makes it a technologically important material to provide exchange coupling to the $Ni_{80}Fe_{20}$ in the

magnetic recording industry. NiO is chemically stable and has high resistivity [55, 56]. The $Ni_{80}Fe_{20}$/NiO spin valve system provides high sensitivity [56]. From the technological point of view, a material with minimum coercivity and maximum exchange bias field is important. In this project, $Ni_{80}Fe_{20}$ and the $Ni_{80}Fe_{20}$/NiO nano-stripes were studied to understand the effect of the constrained geometry on the coercivity and the exchange bias field. Magnetometery and susceptometery techniques were employed in order to characterize the magnetic behaviour of the thin films and nano-stripes systems.

Chapter Two: Experimental Techniques

2.1 Sample Preparation

The samples were prepared by Hsuan-Rong Huang under the supervision of Dr. Ko-Wei Lin at the Department of Material Science and Engineering, National Chung Hsing University, Taiwan. Figure 2.1 shows a schematic diagram of the Dual Ion Beam Deposition System used to prepare the $Ni_{80}Fe_{20}$ and the $Ni_{80}Fe_{20}$/NiO samples. Commercial $Ni_{80}Fe_{20}$ and Nickel sources were used as targets. The Kaufman source was used to focus an argon (Ar) ion beam onto the $Ni_{80}Fe_{20}$ or Ni target for the cleaning or in-situ ion bombardment during NiO deposition. The End-Hall source was used with a fixed voltage to ensure constant ion-beam bombardment energy during NiO deposition. The pressure was first reduced to 4×10^{-7} Torr, and deposition was done at 5×10^{-4} Torr. The O_2/Ar ratio in the End-Hall ion source was kept fixed at 16% and it was operated at an anode of voltage 70 V and an anode current of 0.68 A. For the Kaufman ion source, the argon flow was 3 sccm while the beam voltage was 804 V and the current was 7.5 mA.

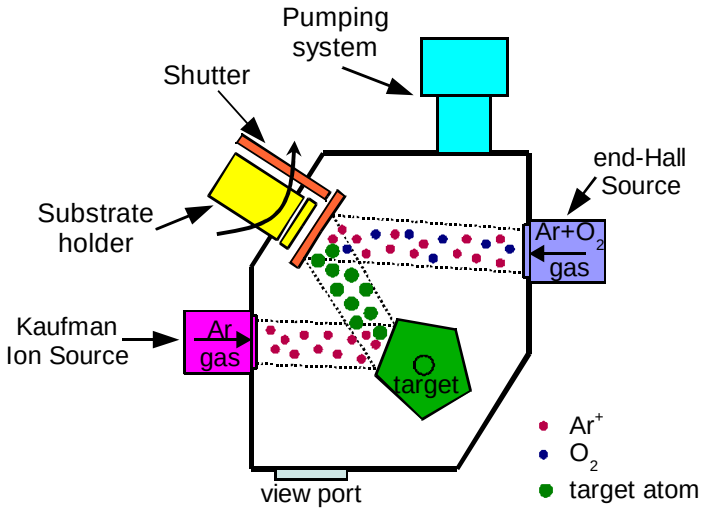

Figure 2.1: Schematic diagram of a Dual-ion Beam Deposition System

$Ni_{80}Fe_{20}$ and $Ni_{80}Fe_{20}$/NiO nano-stripes were prepared onto a template which consisted of a patterned hydrogen silsesquioxane (HSQ) film on the top of a silicon oxide substrate, as shown in Fig. 2.2. The 50 nm thick and 76 nm-period line/space structure (Fig. 2.2) in HSQ was made using EUV-IL (Extreme Ultraviolet Interference Lithography) at the Paul Scherrer Institute (PSI), Switzerland by Eulitha Corp. EUV-IL provided high resolution (~ 10 nm) and yielded precise positioning of the stripes. Figure

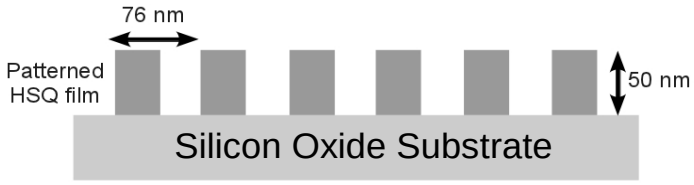

Figure 2.2: A schematic diagram of the template used for the nano-stripe deposition

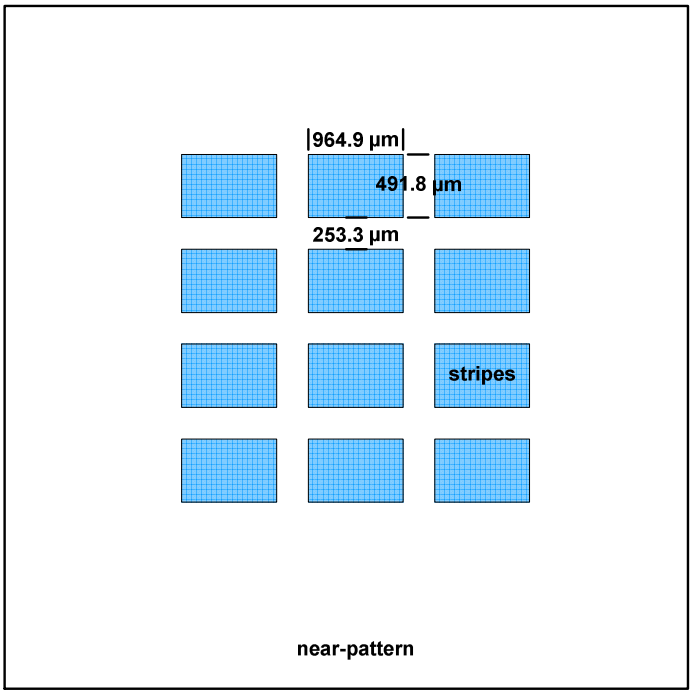

Figure 2.3: A schematic diagram of the exposed film. The shaded areas represent the patterned regions. Film size was 3 cm × 3 cm.

2.3 shows a schematic of the nano-stripes sample with the dimensions of patterned areas. The dimensions were extracted from a scanning electron microscopy image of the exposed film provided by Eulitha Corp. The size of the developed film was 3 cm × 3 cm.

2.2 Structural and compositional characterization techniques

Transmission electron microscopy (TEM) and scanning electron microscopy (SEM), was performed to have insight into the microstructure and composition of the samples.

2.2.1 Transmission Electron Microscopy (TEM)

The JEOL JEM-2010 (Fig. 2.4a), operating at 200 kV and equipped with a LaB_6 electron gun, was used for the microstructural characterization of the samples. The JEM-

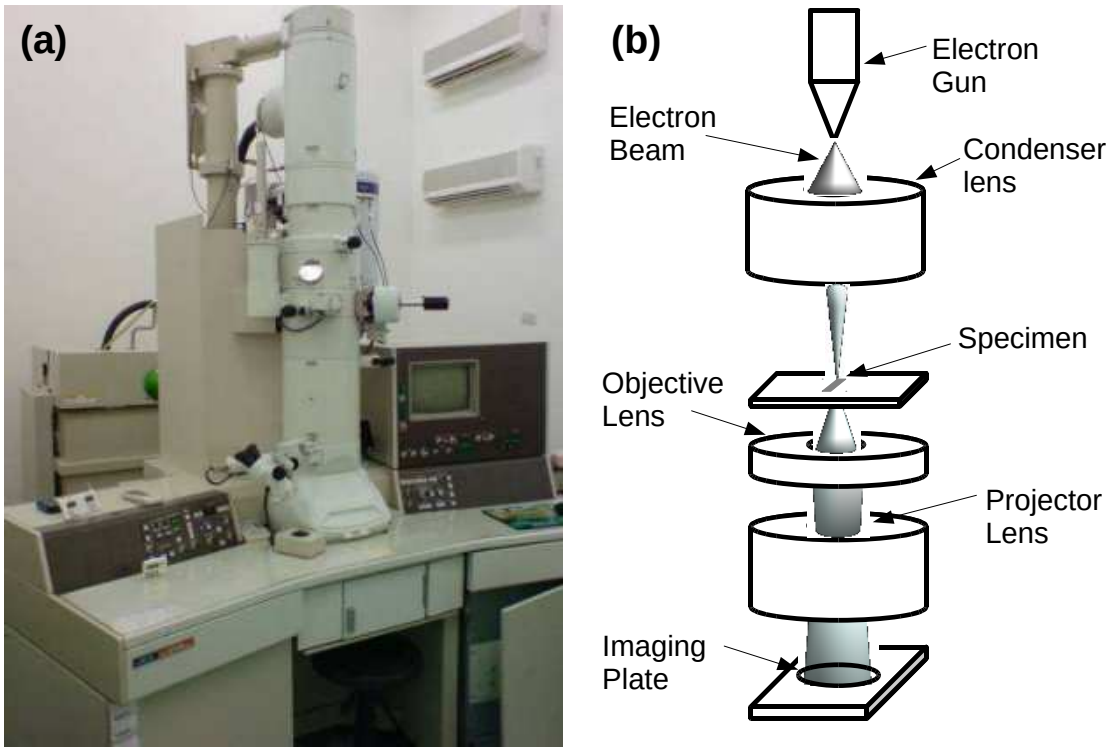

Figure 2.4: TEM (a) JOEL JEM-2010 (b) Layout of optical components of a basic TEM

2010 can provide high resolution imaging with 0.23 nm point resolution.

Figure 2.4b shows the layout of the optical components in a basic TEM. An electron gun at the top produces the beam of electrons. The condenser aperture allows the formation of the electron beam to the desired size and location for interaction with the sample. A typical TEM is equipped with three stages of lenses, i.e. condenser lens, objective lens and projector lens. Finally, the image is formed on the phosphor screen at the bottom. In general, this screen is replaced by an image recording system [57].

2.2.2 Scanning Electron Microscope

A scanning electron microscope (SEM) was used for the structural characterization of the template and the nano-stripes. Fig. 2.5 shows a simplified diagram

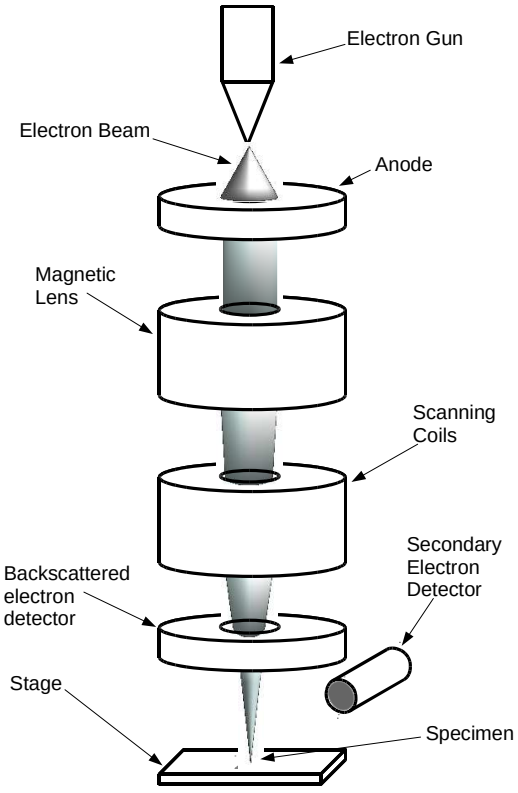

Figure 2.5: Schematic of the SEM components

of the SEM showing its components. The electrons emitting from the electron source (tungsten filament, LaB_6 etc) are accelerated through a typical accelerating voltage of 30 kV. After passing through the magnetic lens, the electron beam falls on the specimen. The electron beam, on striking the surface, produces some backscattered electrons, some lower energy secondary electrons, a few Auger electrons and characteristic x-rays which are detected by respective detectors [58, 59].

2.3 Magnetic characterization techniques

The magnetic characterization of the samples included AC and DC susceptibility and hysteresis loop (M vs H) measurements. This magnetic characterization was performed with the commercial superconducting quantum interference device (SQUID) magnetometer, Quantum Design MPMS-XL, using a reciprocating sample option (RSO) which provided a sensitivity of 5×10^{-9} emu [60].

SQUID operation is based on flux quantization and Josephson tunnelling [62]. The MPMS-XL employs a radio-frequency SQUID (rf-SQUID) for the magnetic measurements. In the rf-SQUID, a single Josephson junction is connected in a

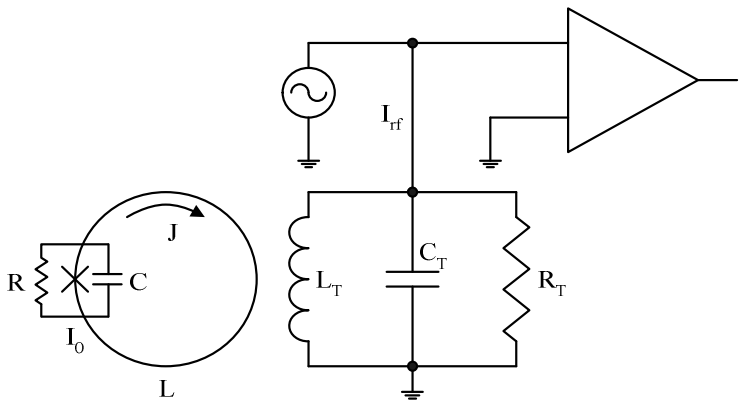

Figure 2.6: A schematic of the rf-SQUID

superconducting loop. This loop is inductively coupled to the inductor (L_T) of a tank circuit. An AC current source oscillating at a resonant frequency (20 MHz to 10 GHz) drives this tank circuit. Figure 2.6 shows a schematic diagram of an rf-SQUID. The measured flux is superimposed over some dc bias flux. This flux results in a change of the average value of the phase across the Josephson junction which causes a change in the impedance for the rf drive oscillations. This causes a variation in the amplitude of the rf voltage across the tank circuit. This variation is then amplified and filtered. The output voltage is proportional to the measured flux.

In the MPMS-XL, the sample moves through the superconducting pickup coils (Fig. 2.7). These pickup coils are connected to the SQUID with superconducting wires. The current from the detection coils is fed to the SQUID sensor by inductive coupling. The SQUID electronics produces an output voltage that is proportional to the current

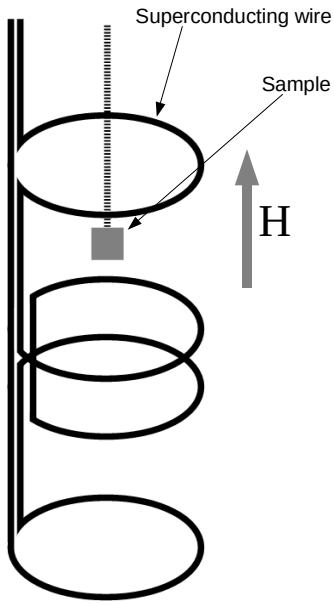

Figure 2.7: A schematic of the superconducting detection/pickup coils

flowing in the SQUID input coil working as a highly sensitive current-to-voltage convertor [63].

The measurement of a sample magnetization is performed by moving the sample through the pickup coils (Fig. 2.7). These coils are located at the center of the magnet outside the sample chamber. The magnetization of the moving sample produces an electric current in the pickup coils. Any change in the magnetic flux results in a variation in the persistent current in the closed circuit formed by the detection coils, the connecting wires and the SQUID input coil. This variation in the current in the pickup coils produces corresponding variations in the SQUID output voltage which is proportional to the magnetic moment of the sample [64].

2.3.1 The Superconducting Magnet

The MPMS uses a superconducting magnet wound in a solenoid configuration. The magnet is constructed as a closed superconducting loop and hence allows it to be charged up to a specific current. Once charged, the magnet can operate during a measurement in persistent mode without any external current source or power supply [64]. The Quantum Design MPMS-XL used in this work provides a magnetic field range of $\pm$ 5.5 T with high homogeneity about the sample space (0.048% over 3 cm scan length [65]).

2.3.2 Magnetic Measurements

As a part of the sample preparation for these measurements, the film was first cut of the proper size and enclosed in a gelatine capsule and immobilized. The capsule was then inserted in a clear straw of length 13.5 cm (Fig. 2.8) so that the sample was near the middle of the detection coil when installed in the MPMS. Due to the geometry of the

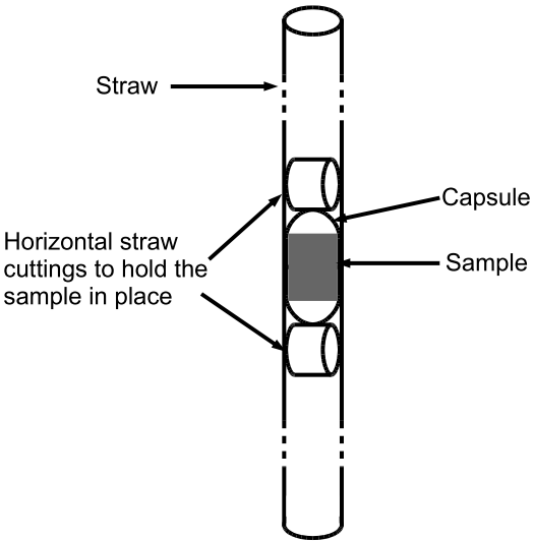

Figure 2.8: The sample holder assembly showing the sample inside the capsule

pickup coils, a sample of size of 3 mm in all three dimensions is recommended. To keep the gelatine capsule fixed at its location, two straw pieces were fitted at both sides of the capsule as shown in the Fig. 2.8. The straw was closed with plugs at both sides and attached to the graphite sample rod. The sample was then inserted in the sample holder space while keeping the airlock valve closed. As the final stage of the sample installation, the sample space was purged and then the airlock valve was opened. After this, the sample rod was lowered into the sample space and secured to the actuator shoe at the end outside the sample chamber.

The sample has to be centered properly to ensure that all four pickup coils sense the magnetic moment of the sample. Figure 2.9 illustrates the centering procedure. If properly centered, the sample should be at the bottom dashed line (Fig. 2.9a). As the sample moved through the pickup coils, SQUID response to its magnetization was plotted (Fig. 2.9b). Figure 2.9c shows the SQUID response as a function of the scan

length which shows that the sample was not centered and hence needed adjustment. If the cases when the adjustment was within the limit of the transport mechanism, the automatic adjustment function of MPMS MultiVu software was enough. However in the case when required adjustment was beyond the limits of the transport mechanism, the sample had to

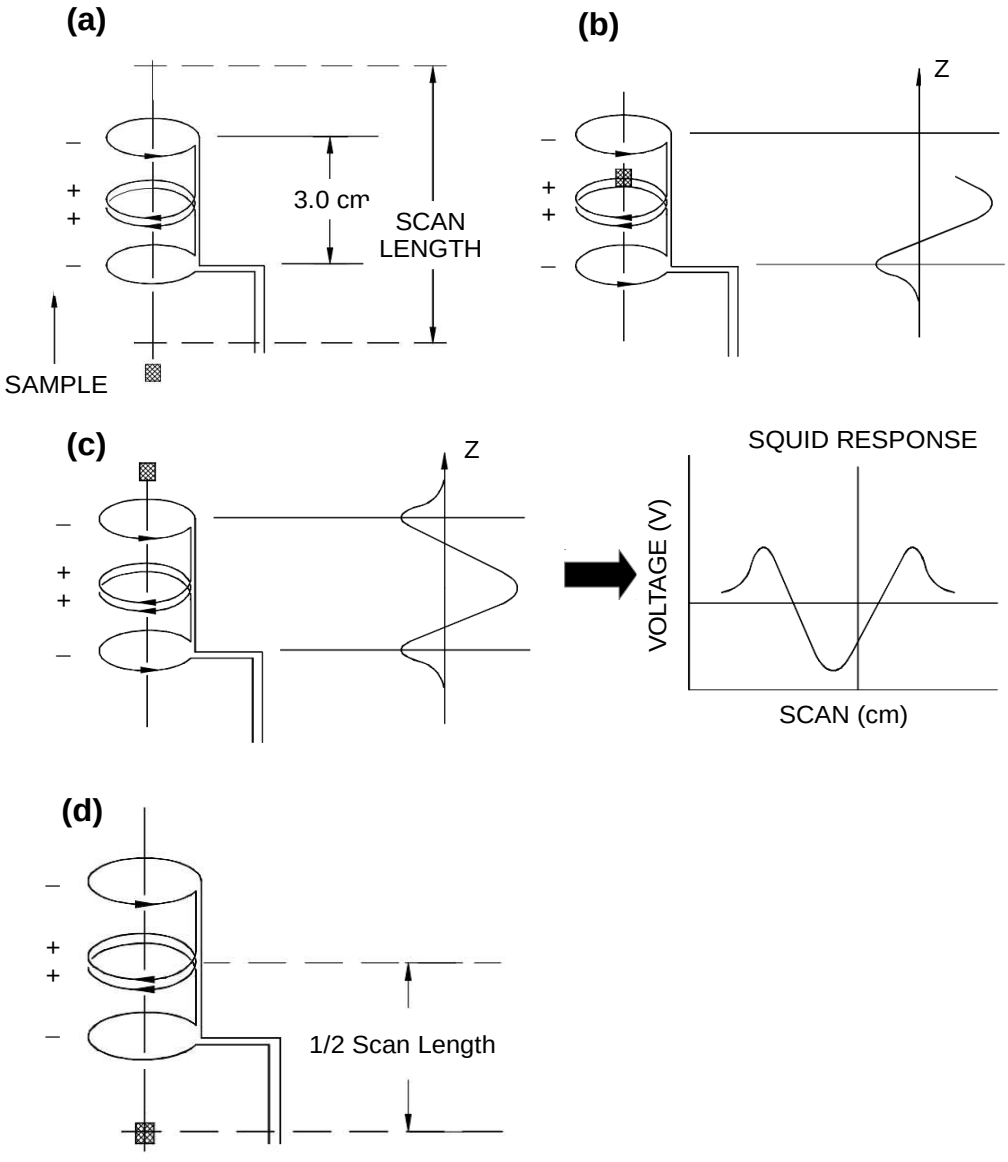

Figure 2.9: DC centering and voltage response from the SQUID (used with permission from Quantum Design, USA) [66]

be removed from MPMS. The position of the gelatine capsule was adjusted depending on the measured center position. For a 6 cm scan length, if the measured center was at a position above 3 cm, e.g. 3.6 cm, the gelatine capsule was moved upward and vice versa. After this manual adjustment, the sample was installed and centered again.

The measured magnetization of the sample depends on its initial magnetization, the remnant field in the magnet and the quantity of the material. To address the problem of the initial magnetization, centering was performed at different fields e.g. 0 Oe, 10 Oe, 100 Oe, 500 Oe so that it was ensured that the signal was actually from the sample and not the straw or gelatine capsule. At the higher fields the signal could switch from positive to negative polarity because the diamagnetic signal from the gelatine capsule and the substrate was large enough to overcome the positive signal from the ferromagnetic film. The diamagnetic signal from the straw was not important as it was cancelled due to the second derivative configuration of the pickup coils (Fig. 2.7). The remnant field in the MPMS magnet was the field trapped in the superconductor winding of the magnet after being charged to a high magnetic field. This issue was resolved using the "Magnet Reset" option in the MPMS MultiVu software which served the purpose by quenching the field.

2.3.2.1 AC Susceptibility

For an AC susceptibility measurement, a small AC drive field (small enough not to affect the intrinsic energy barrier in the system [67]) of frequency ω is applied. This drive field induces a time-dependent magnetization in the sample which is detected by the SQUID. For very low frequencies, AC susceptometery is most similar to DC magnetometery. In this case, the induced magnetic moment of the sample is give by $M_{AC} = (dM/dH)\, H_{AC}\, sin(\omega t)$ where $\chi = dM/dH$ is the slope of the magnetization as a function of

the applied field curve, called the susceptibility, H_{AC} is the amplitude of the driving field and ω is the driving frequency. The AC magnetization of the sample does not follow along the M vs H curve at higher frequencies because of the dynamic effects in the sample. The AC magnetic susceptibility measurement gives the magnitude of the susceptibility (χ) and the phase shift relative to the drive signal (φ). The in-phase component of the AC susceptibility is $\chi'(\omega) = \chi(\omega) \cos(\varphi)$ and the out-of-phase component is $\chi''(\omega) = \chi(\omega) \sin(\varphi)$ [68].

AC susceptibility is time-dependent measurement and the timescale is well defined which can be varied over several orders of magnitude i.e. from ~10^{-2} s^{-1} to 10^{3} s^{-1}. The real or in-phase component of AC susceptibility, $\chi'(\omega)$, indicates how well the magnetization of the system follows the applied field. The imaginary or out-of-phase component of AC susceptibility, $\chi''(\omega)$, represents the dissipative processes in the sample [68], [13].

In order to measure the AC susceptibility, the sample was first zero-field-cooled down to 5 K and then AC susceptibility measurement was done, after applying a drive field of 2.5 Oe, in the temperature range 5 – 400 K at frequencies 10 Hz, 500 Hz and 1000 Hz. The measurements were done at 10 K intervals with the temperature stabilized during the measurement. A sample script for an AC susceptibility measurement is given in Appendix A. The frequency dependent change in the AC susceptibility data corresponds to superparamagnetic blocking temperature [67]. A frequency independent peak in both the in-phase and out-of-phase measurements represents a Néel or Curie temperature of the sample depending on the magnetic nature of sample (FM or AFM).

2.3.2.2 DC Susceptibility

DC susceptibility is the time averaged magnetization of the sample as a function of the temperature in a constant applied magnetic field. It is a low-field technique and can give information about the Curie temperature (from a significant rise in the magnetization below the Curie temperature) and blocking temperature (from the bifurcation of zero-field-cooled (ZFC) and field-cooled (FC) M vs T measurements [11].

DC susceptibility as a function of temperature was measured over 5 K to 400 K. The magnetic field was 100 Oe. The sample was first cooled down to 5 K in the absence of any applied field as a part of ZFC measurement. Then the time averaged magnetization of the sample was measured in response to the 100 Oe applied field as the temperature was raised to 400 K in 10 K intervals with the temperature stabilized every 10 K. This was followed by cooling the sample again down to 5 K (FC measurement) and measuring the time averaged magnetization of the sample in response to the 100 Oe applied field. The sample was then heated to room temperature after setting the field to O Oe. A sample script for a M vs T measurement is given in Appendix B.

2.3.2.3 Hysteresis Loops (M vs H)

Hysteresis loops (M vs H) are very important to understand the magnetization reversal mechanism and macroscopic magnetic properties of the sample. The hysteresis loops were measured after field-cooling the sample to 5 K in the presence of 20 kOe magnetic field. The samples were field-cooled before measuring the hysteresis loops to study the magnetization reversal and exchange bias. Important information regarding the magnetization reversal mechanism and coercivity behaviour was gained from the measured hysteresis loops. In order to get maximum information, the loops were

measured with small field increments (5 Oe or 10 Oe) at the fields around the coercivity while larger field steps were used for measurements at larger fields. A sample script for hysteresis loop measurement is given in Appendix C.

Chapter Three: $Ni_{80}Fe_{20}$ nano-stripes

3.1 Structural Characterization

The structural characterization of the $Ni_{80}Fe_{20}$ nano-stripes was performed by Hsuan-Rong Huang at the Department of Materials Science and Engineering, National Chung Hsing University (NCHU), Taiwan under the supervision of Dr. Ko-Wei Lin.

3.1.1 Micro-structural Characterization

A scanning electron microscopy (SEM) image (Fig. 3.1b) showed a 25 nm separation (valley) between the 44 nm wide $Ni_{80}Fe_{20}$ nano-stripes. Figure 3.1a shows the cross-sectional view of the nano-stripes while Fig. 3.1b shows the planar view. A cross-sectional view of a single nano-stripe is shown in the inset of Fig. 3.1a. Results showed that the thickness of the deposited $Ni_{80}Fe_{20}$ was 12 nm at the top, 9 nm at the sides, and 10 nm in the space between the stripes (valley).

A near-pattern film was the part of the un-patterned film around the stripes (Fig. 3.2) and hence underwent the same deposition process as the nano-stripes. Figure 3.2 shows the transmission electron microscope (TEM) bright-field (a) and dark-field (b)

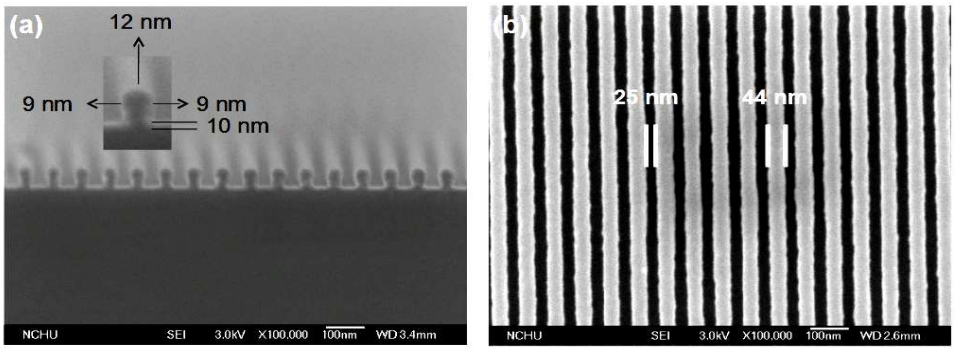

Figure 3.1: SEM images of the $Ni_{80}Fe_{20}$ nano-stripes (a) cross-sectional view, a single stripe is shown in the inset with the thickness of the deposited region. (b) planar view, width of the stripe and the valley is shown.

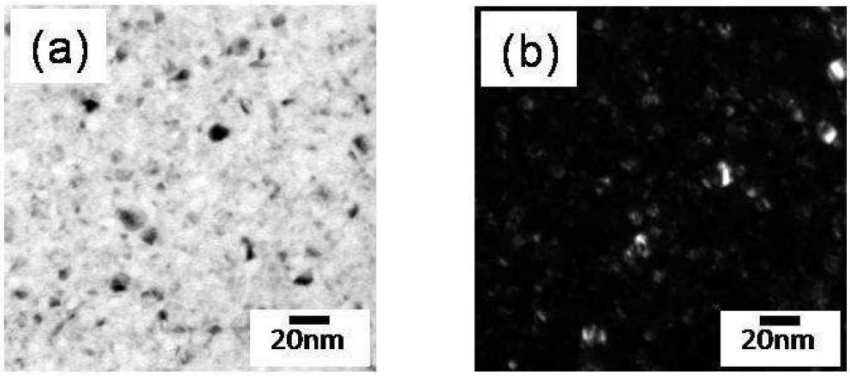

Figure 3.2: The (a) bright field and the (b) dark-field TEM images of the Permalloy near-pattern film.

images of the $Ni_{80}Fe_{20}$ near-pattern film. An 18 nm thick polycrystalline film was observed with the crystallite sizes between 5 nm and 15 nm.

3.2 Magnetic Characterization

Figure 3.3 shows the applied field (H) configurations for the parallel, transverse and perpendicular/out-of-plane measurements. The near-pattern film was characterized in

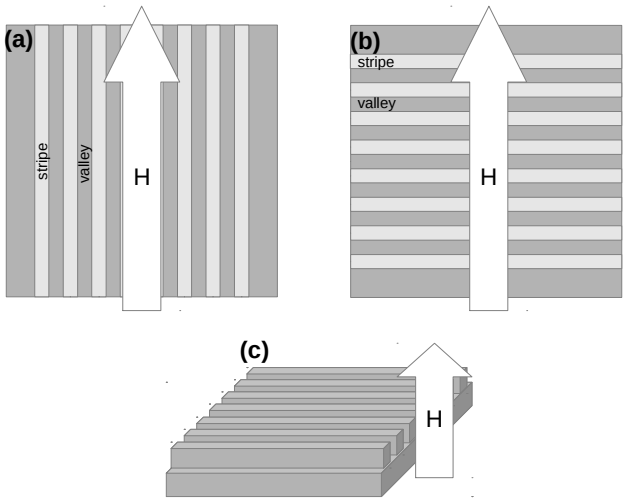

Figure 3.3: A schematic diagram of the applied field (H) configuration in the (a) parallel and (b) transverse and (c) perpendicular configuration.

the in-plane configuration only because the demagnetization field was the only difference between the in-plane and out-of-plane configuration.

3.2.1 $Ni_{80}Fe_{20}$ near-pattern film

In this section we shall discuss the magnetic characterization of the $Ni_{80}Fe_{20}$ near-pattern film that encompasses the AC and the DC susceptibility measurements and the hysteresis loops.

3.2.1.1 AC Susceptibility Analysis

The in-phase AC susceptibility measurement (Fig. 3.4a) shows two frequency dependant changes at 50 K and 150 K. As the sample was cooled to 5 K in the absence of any applied field, domains were frozen randomly. With the increase in the temperature from 5 K, the domains remained blocked until 30 K. The thermal energy was not enough to overcome the anisotropy energy of the domains. At 30 K, the in-phase AC susceptibility started increasing. At ~50 K, the system changed its magnetization from "blocked" to "superparamagnetic". This change to superparamagnetism resulted in the small peak also in the out-of-phase AC susceptibility measurement (Fig. 3.4b). At this temperature (50 K), available thermal energy was enough to overcome the anisotropy energy of the domains of smaller crystallites only. With the increase in the temperature, larger domains from the larger crystallites also relaxed resulting in a continuous increase in the in-phase signal (Fig. 3.4a). This crystallite size distribution resulted in a plateau in the in-phase AC susceptibility. At 250 K, the out-of-phase AC susceptibility (Fig. 3.4b) started decreasing while the in-phase AC susceptibility continued to increase which is, in addition to the frequency dependence, another characteristic of superparamagnetism [69].

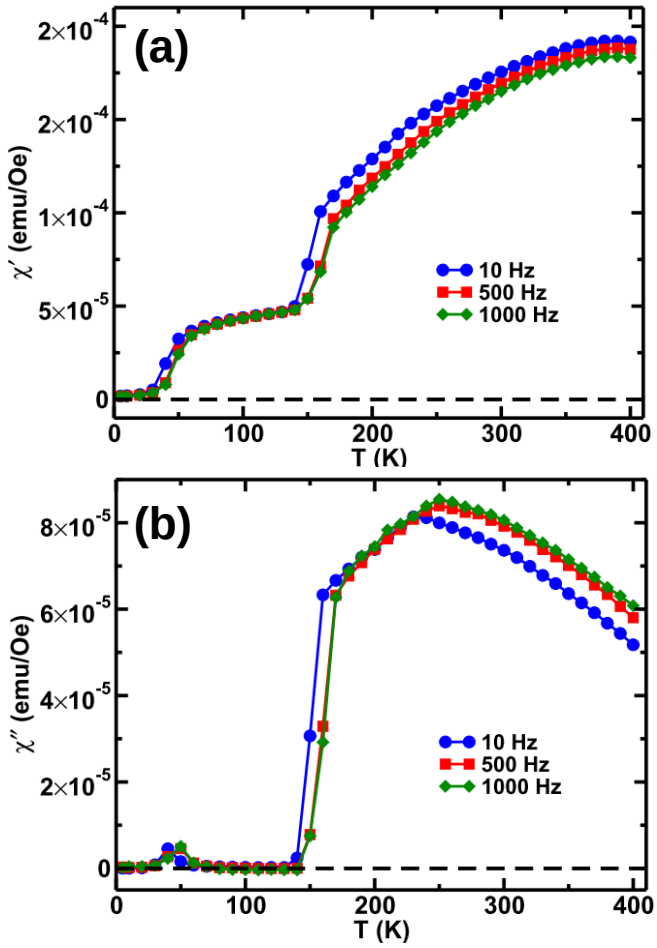

Figure 3.4: AC susceptibility data for the $Ni_{80}Fe_{20}$ near-pattern film showing the (a) in-phase (χ′) and the (b) out-of-phase (χ″) data at measuring frequencies of 10, 500 and 1000 Hz (error bars are smaller than the symbols)

3.2.1.2 DC susceptibility Analysis

Figure 3.5 shows the ZFC and the FC temperature dependence of magnetization of the $Ni_{80}Fe_{20}$ near-pattern film. The zero-field-cooling resulted in the magnetization of domains being frozen randomly resulting in the very low overall magnetization of the film at 5 K. With the increase in temperature from 5 K, the domains started relaxing. With the increase in the temperature, thermal energy permitted the domains to orient

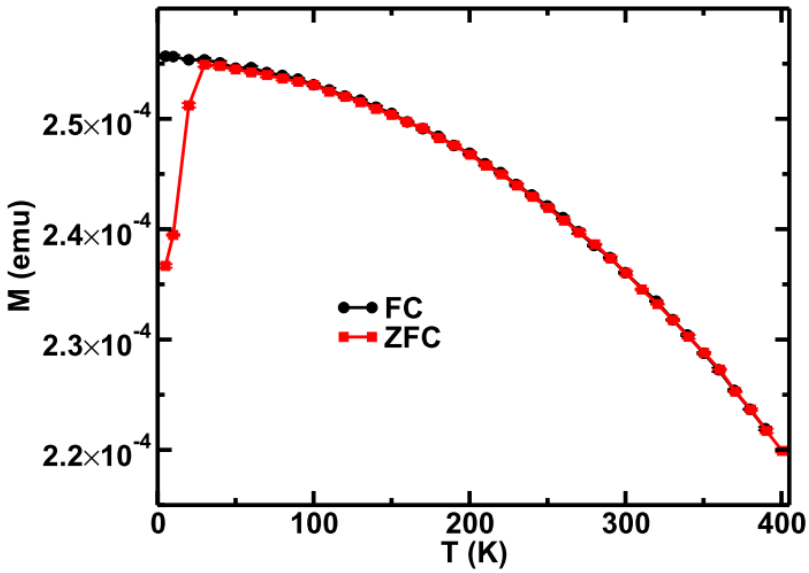

Figure 3.5: Low-field (100 Oe) ZFC and FC temperature dependence of the magnetization for the $Ni_{80}Fe_{20}$ near-pattern film parallel to *H*. (error bars are smaller than the symbols)

along the applied field direction. Being considerably smaller (5-15 nm) than the single domain critical size for the $Ni_{80}Fe_{20}$ (~22 nm), the crystallites of the sample were expected to be single-domain. At low temperatures, the thermal energy was enough to overcome the anisotropy barrier of smaller domains only. However, with the increase in the temperature till 30 K, domains of the larger crystallites were able to relax and be aligned along the applied field resulting in continuous increase in the overall moment of the sample. At 50 K, the ZFC and the FC curves merged together which indicated that no irreversibility in the magnetization was expected at and above 50 K in the presence of the 100 Oe applied field. This showed a superparamagnetic character to the magnetic response [69] and was in agreement with the AC susceptibility measurements. At this stage, the anisotropy barrier of the domains was overcome by the thermal energy and the

only force affecting the alignment of the domains was that from the applied magnetic field. That was why the ZFC and the FC measurements were the same beyond 50 K. With the increase in temperature, increasing thermal fluctuations resulted in a gradual decrease in the magnetization of the sample until 400 K.

For the FC measurement, until 50 K, the sample magnetization was superparamagnetic and hence the magnetization of the sample kept increasing with the decreasing temperature because of the decrease in thermal fluctuations. As the temperature was further decreased below 50 K, a bifurcation was observed between the ZFC and the FC measurements because the applied field aligned the domains during the cooling process resulting in an increased magnetization of the sample.

3.2.1.3 Hysteresis loops

Figure 3.6 shows hysteresis loops for the $Ni_{80}Fe_{20}$ near-pattern film at different temperatures in a parallel field configuration. Figure 3.7 shows the same hysteresis loops after the subtraction of the high field susceptibility (Fig. 3.8) from the substrate and the sample holder, while Fig. 3.9 shows the same hysteresis loops over the applied field range of $\pm$500 Oe.

Some coercivity was observed at 10 K and 25 K, however by 50 K the coercivity reduced to zero. The crystallite size distribution resulted in a coercivity at the lower temperatures, i.e. 10 K and 25 K because at the lower temperatures, thermal energy was not enough to overcome the anisotropy barriers of all the domains and hence the need of a higher magnetic field to rotate larger domains resulted in a non-zero coercivity [72]. At the higher temperatures, the thermal energy was enough to overcome the anisotropy barrier of the domains of the crystallites so the applied magnetic field was able to align

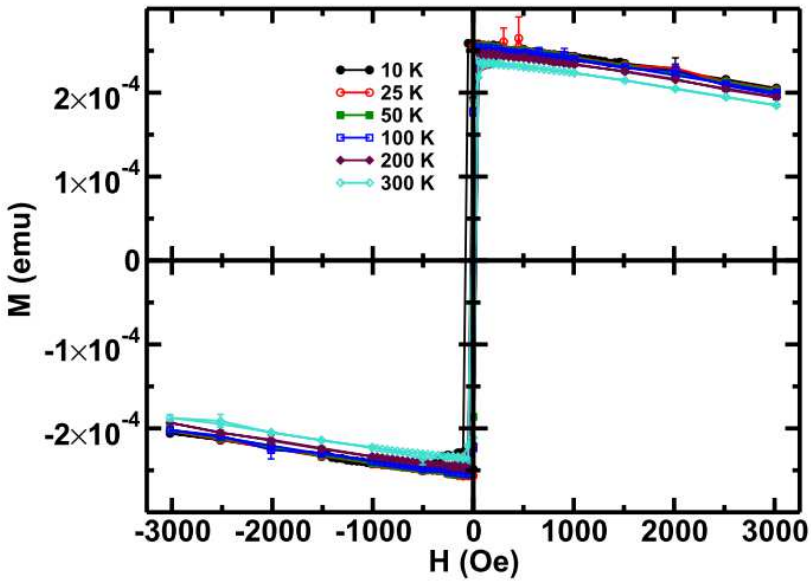

Figure 3.6: Hysteresis loops (20 kOe field-cooled) for the $Ni_{80}Fe_{20}$ near-pattern film before subtracting the high field susceptibility

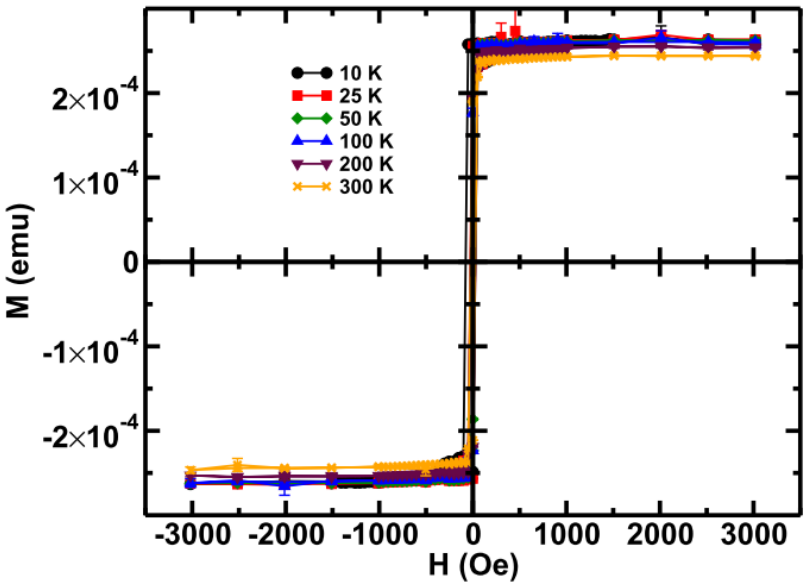

Figure 3.7: Hysteresis loops (20 kOe field-cooled) for the $Ni_{80}Fe_{20}$ near-pattern film after subtracting the high field susceptibility

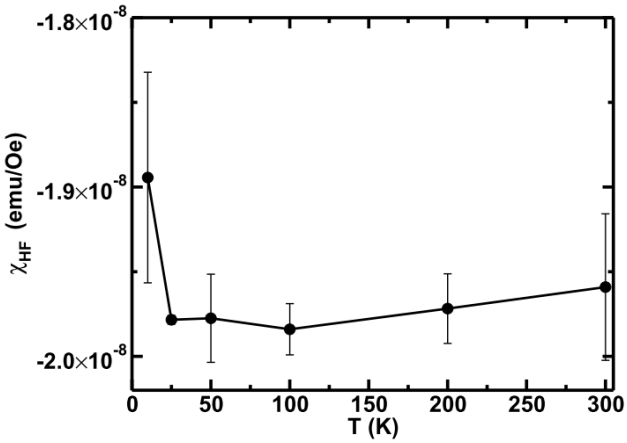

Figure 3.8: High-field diamagnetic susceptibility (χ_{HF}) from the substrate and sample holder assembly

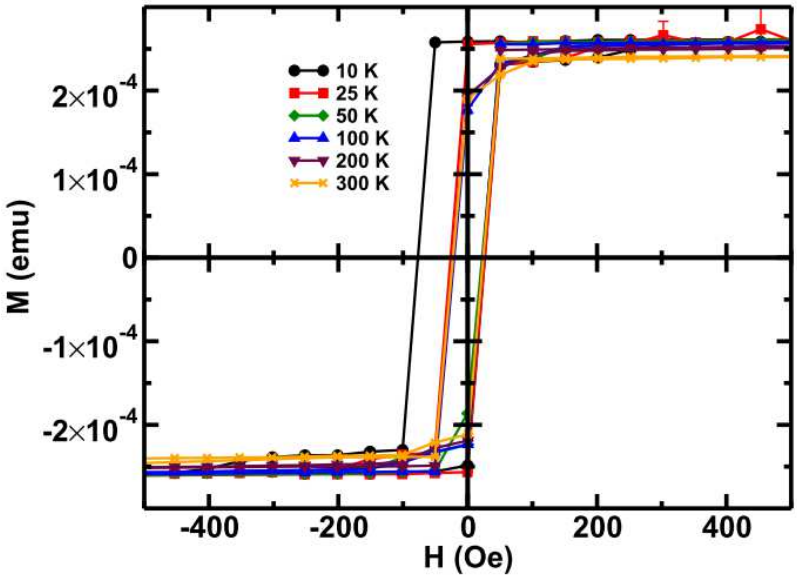

Figure 3.9: Hysteresis loops (field-cooled 20 kOe) for the $Ni_{80}Fe_{20}$ near-pattern film, magnified in the applied field range ±500 Oe

the domains' magnetization and hence the coercivity vanished by 50 K. This was in agreement with the AC and the DC susceptibility measurements. The crystallite size distribution resulted in an asymmetric behaviour of the loop along the magnetization axis

in the intermediate fields while going form +H to –H and from –H to +H. For example, considering the hysteresis loop at 10 K, magnetization was different in the applied field range from -100 Oe to -400 Oe as compared to that from -400 Oe to -100 Oe. At very low temperature, the domains were blocked because of the low thermal energy and hence a larger magnetic field was required to align all the domains in the direction of the applied field. As the direction of the applied field was reversed a smaller applied field was able to align the domain in smaller crystallites only. With an increase in the magnitude of applied field, domains in the larger crystallites also aligned along the applied field (Fig. 3.9).

The coercivity was not measurable at 50 K as the thermal energy was enough to overcome the anisotropy barrier of the domains, which was in agreement with the AC and the DC susceptibility measurement.

An interesting phenomenon was the non-zero exchange bias field in the $Ni_{80}Fe_{20}$ film (Fig. 3.10b). This was, most likely, because of a surface effect [34, 35]. The surface magnetization was different from the bulk of the film and played an important role at low

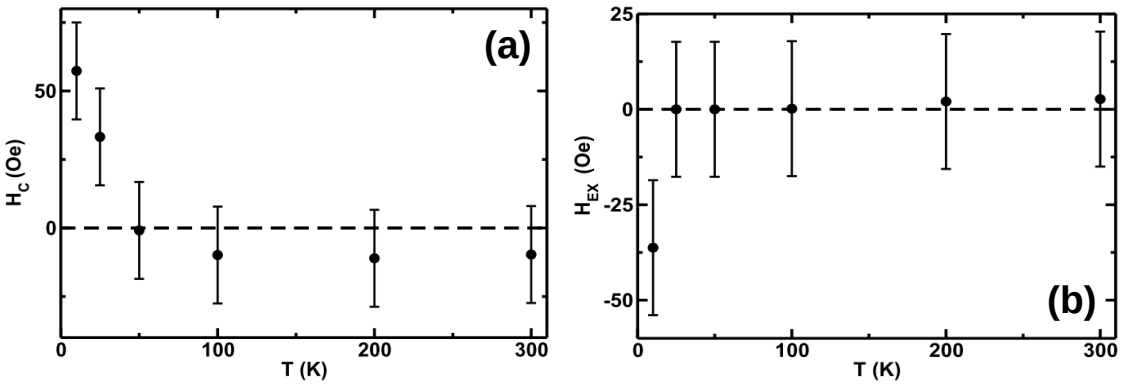

Figure 3.10: Temperature dependence of (a) the coercivity (H_C) and (b) the exchange bias field (H_{EX}) for the $Ni_{80}Fe_{20}$ near-pattern film

temperatures where thermal energy was smaller than the surface anisotropy energy. This difference of the magnetization behaviour, as a result of pinning of the magnetization, caused the non-zero exchange bias field. The exchange bias field dropped to zero at 25 K because the thermal energy was able to overcome the surface anisotropy energy at this temperature.

3.2.2 $Ni_{80}Fe_{20}$ nano-stripes in the parallel configuration

This section will encompass the magnetic characterization of the $Ni_{80}Fe_{20}$ nano-stripes in a parallel field configuration (Fig. 3.3a) describing the AC and the DC susceptibility measurements and the hysteresis loops.

3.2.2.1 AC susceptibility Analysis

The in-phase and the out-of-phase AC susceptibility data (Fig. 3.11) showed a frequency dependant change in the temperature range 220–270 K. That frequency dependent change in the AC susceptibility shows that at this point, the sample became superparamagnetic [69]. At that temperature, thermal energy was enough to overcome the anisotropy barriers of the domains and the domains' magnetization started following the applied AC field. A prominent change in the out-of-phase AC susceptibility indicated the dissipative processes in the sample at this temperature as the domains started depinning and following the applied AC field and the domain walls were trying to move. This suggested hysteresis at and below this temperature.

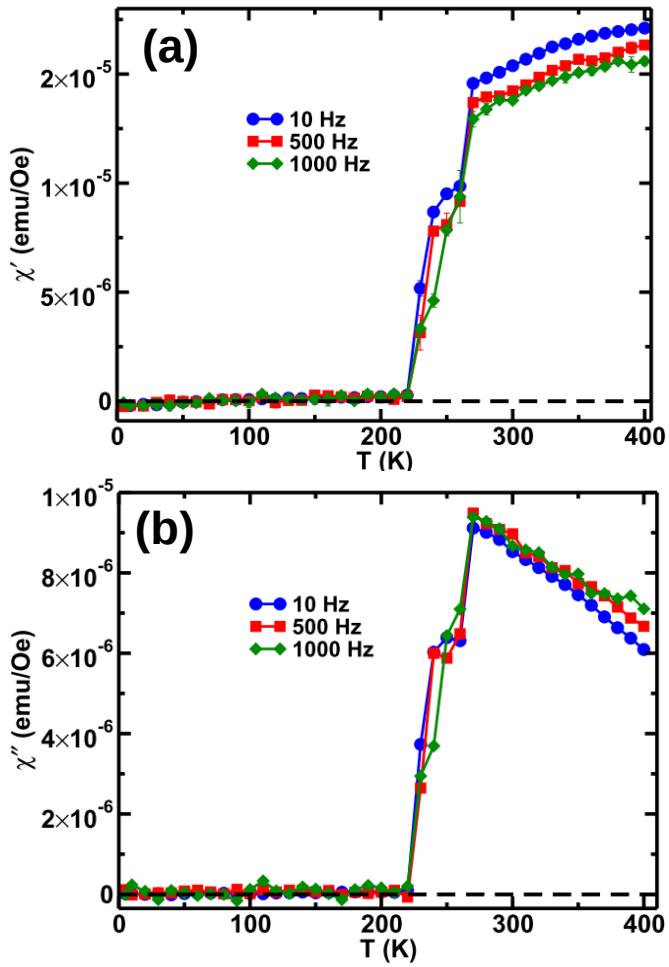

Figure 3.11: AC susceptibility data for the $Ni_{80}Fe_{20}$ nano-stripes in parallel configuration showing the (a) in-phase (χ′) and the (b) out-of-phase (χ″) signals with measuring frequencies 10, 500 and 1000 Hz (error bars are smaller than the symbols)

3.2.2.2 DC Susceptibility Analysis

In the ZFC case (Fig. 3.12), as the magnetic field was applied and the temperature was increased from 5 K, the magnetization of the sample reached its maxima at 90 K. However, at this point, ZFC and the FC measurements did not merge. This indicated the

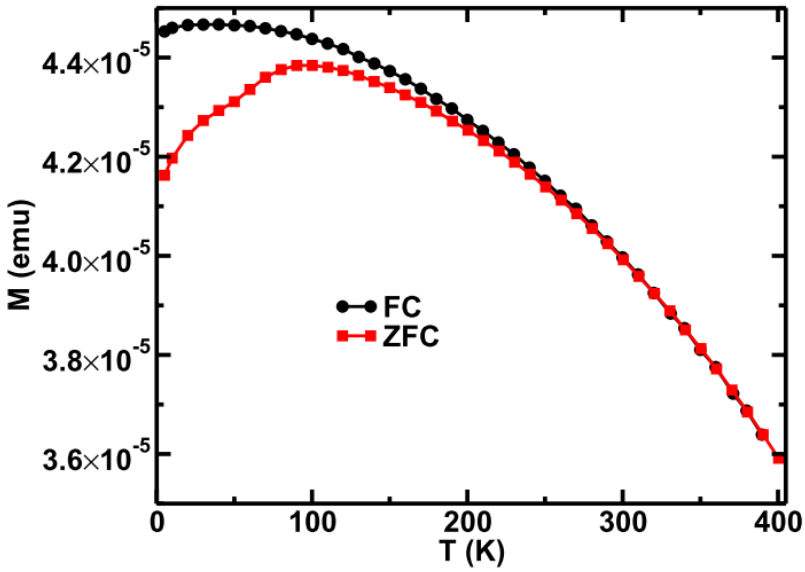

Figure 3.12: Low-field (100 Oe) ZFC and FC temperature dependence of the magnetization of the $Ni_{80}Fe_{20}$ nano-stripes in the parallel field configuration (error bars are smaller than the symbols)

inability of the domains to align in the direction of applied field. This likely stemmed from a magnetic interaction between the neighbouring nano-stripes. With a further increase in the temperature, the ZFC and the FC measurements merged by 280 K indicating the change of magnetization from “blocked” to “superparamagnetic”. As the temperature started decreasing from 400 K, the FC data was the same as the ZFC data till 280 K because only the magnetic field was affecting the domains’ alignment as the sample was superparamagnetic. A bifurcation appeared at 280 K which indicated the irreversibility of the magnetization behaviour. The magnetization of the sample kept on increasing below this temperature as domains were freezing with their magnetization set by the applied field.

3.2.2.3 Hysteresis loops

Figure 3.13 shows hysteresis loops at different temperatures for the $Ni_{80}Fe_{20}$ nano-stripes, after field-cooling the sample in a parallel field configuration. The noisy data at high magnetic fields resulted from the SQUID's response to the overwhelming diamagnetic signal from the substrate and the sample holder assembly. Figure 3.14 shows the same hysteresis loops after the subtraction of the high field susceptibility (Fig. 3.15) of the substrate and the sample holder assembly while Fig. 3.16 shows the same hysteresis loops in the applied field range of -1500 Oe to 1000 Oe.

The shape of the hysteresis loops clearly suggested two magnetic phases in the sample, i.e. applied field dependence of the magnetization from a patterned area with stripes and the near-pattern area around the stripes. Magnetization reversal, in this case, was clearly a two step process. Consider the hysteresis loop at 5 K. Due to the existence of the stripes, the loop was different when the applied field changed from +750 Oe to -1000 Oe as compared to that when the applied field changed from -1000 Oe to +750 Oe. Application of the saturating magnetic field in the parallel field configuration resulted in alignment of the domains along the easy axis of the stripes. Upon the reversal of the applied field, due to the coupling between the neighbouring stripes, the reversal of domains and their propagation along the stripe was blocked. This magnetic coupling resulted in a low magnetization in the low applied field ranges, e.g. -1000 Oe to +750 Oe for the hysteresis loop at 5 K. A larger magnetic field was able to align the domains in the stripes as well. The hysteresis loop being asymmetric along the magnetization axis resulted in the non-zero coercivity in the range of measurement (Fig. 3.17a); however, the exchange bias field (Fig. 3.17b) dropped to zero at 50 K similar to the $Ni_{80}Fe_{20}$ near-

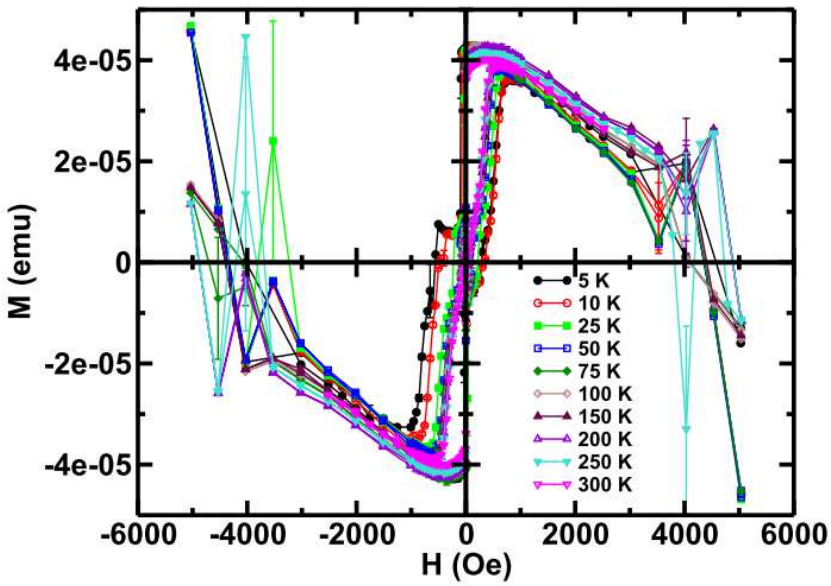

Figure 3.13: Hysteresis loops (20 kOe field-cooled) for the $Ni_{80}Fe_{20}$ nano-stripes in a parallel configuration before subtracting the high field susceptibility.

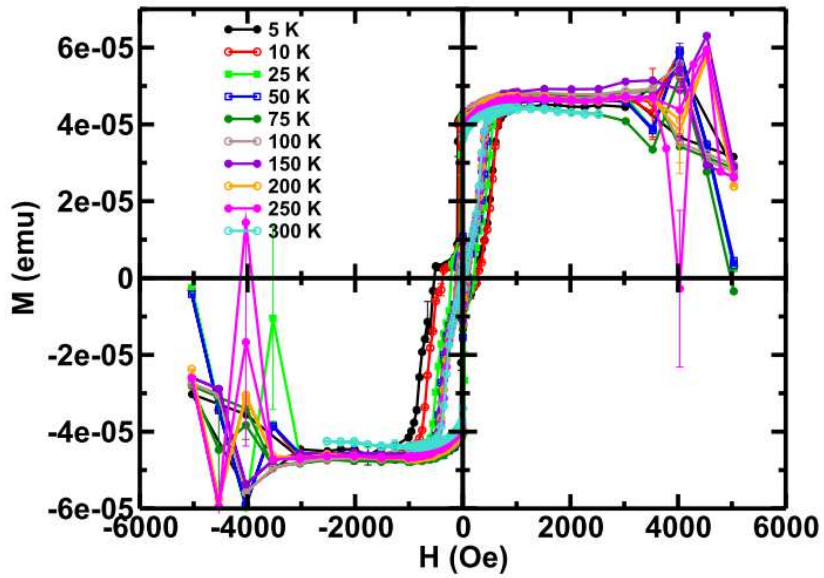

Figure 3.14: Hysteresis loops (20 kOe field-cooled) for the $Ni_{80}Fe_{20}$ nano-stripes in a parallel configuration after subtracting the high field susceptibility.

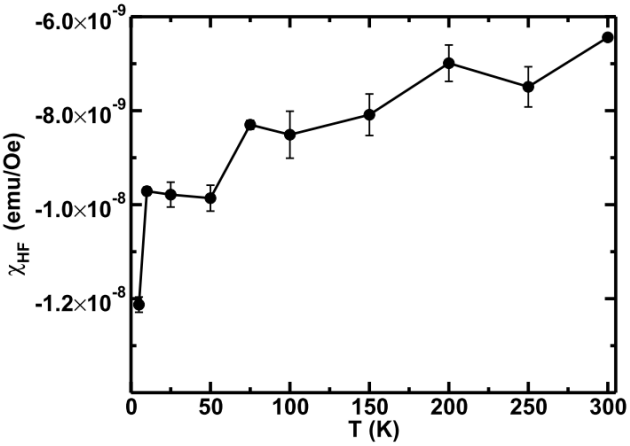

Figure 3.15: High-field diamagnetic susceptibility (χ_{HF}) from the substrate and the sample holder assembly

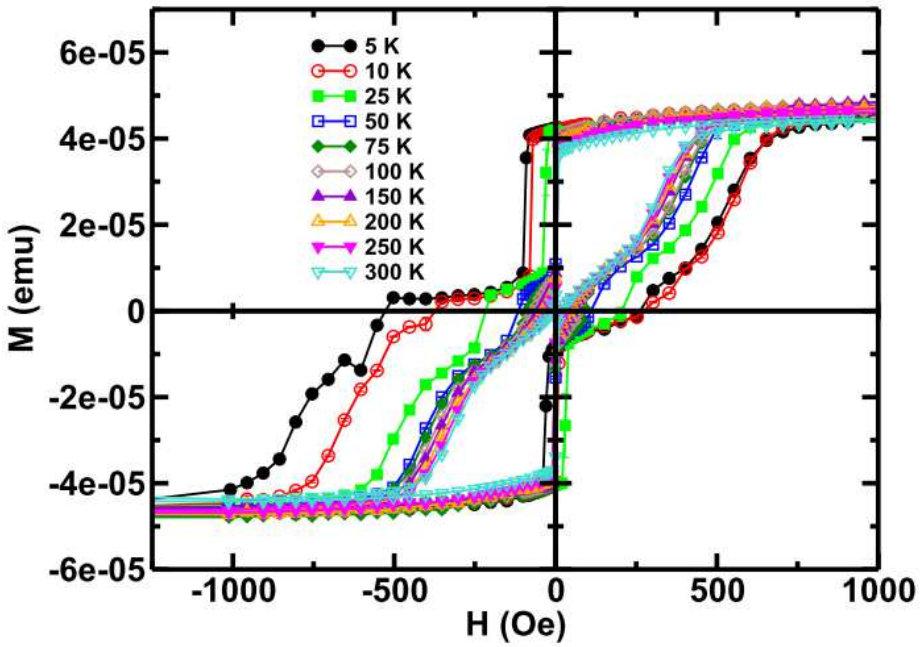

Figure 3.16: Hysteresis loops (20 kOe field-cooled) for the $Ni_{80}Fe_{20}$ nano-stripes in the parallel field configuration over -1500 – 1000 Oe applied field range. (error bars are smaller than the symbols)

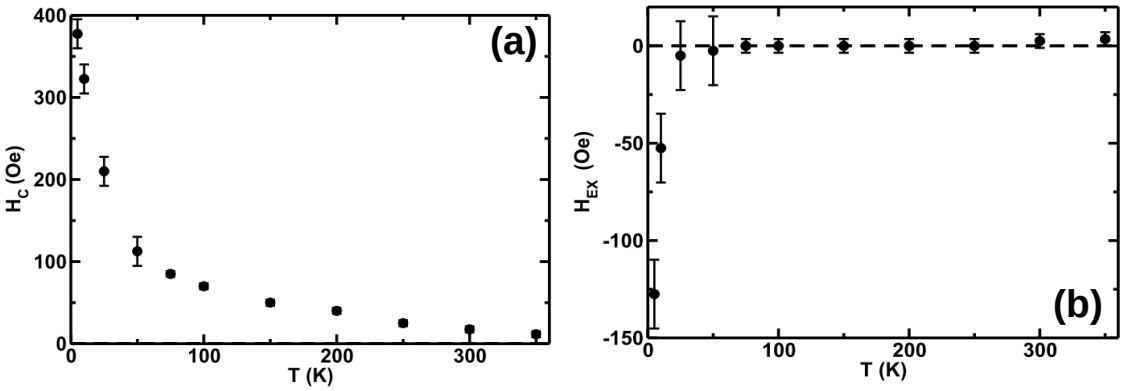

Figure 3.17: Temperature dependence of the (a) coercivity (H_C) and the (b) exchange bias field (H_{EX}) for the $Ni_{80}Fe_{20}$ nano-stripes in the parallel field configuration.

pattern film because of the surface magnetization effect [34, 35]. This surface effect along with the magnetic interaction between the nano-stripes resulted in a non-zero exchange bias field at 5 K, 10 K and 25 K. However, by 50 K the thermal energy was able to overcome the anisotropy barriers of the domains and the exchange bias field was not measureable.

3.2.3 $Ni_{80}Fe_{20}$ nano-stripes in the transverse configuration

This section will describe the magnetic characterization of the $Ni_{80}Fe_{20}$ nano-stripes in the transverse configuration (Fig. 3.3b) describing the AC and the DC susceptibility measurements and the hysteresis loops.

3.2.3.1 AC susceptibility Analysis

The in-phase and the out-of-phase AC susceptibility measurement (Fig. 3.18) showed a frequency dependant change at ~ 50 K. This frequency dependent change was the signature of superparamagnetism [69]. Since the magnetic field oscillated the domains in a direction perpendicular to the axis of the stripes (Fig. 3.3), the domains in

the side areas of the stripes were the most responsive to the applied field. The thickness of the deposited material was only 9 nm at the sides, which was less than the critical size of single domain. The near-pattern area and the top areas of the stripes were not expected to be influenced considerably by this AC magnetic field where an additional interaction

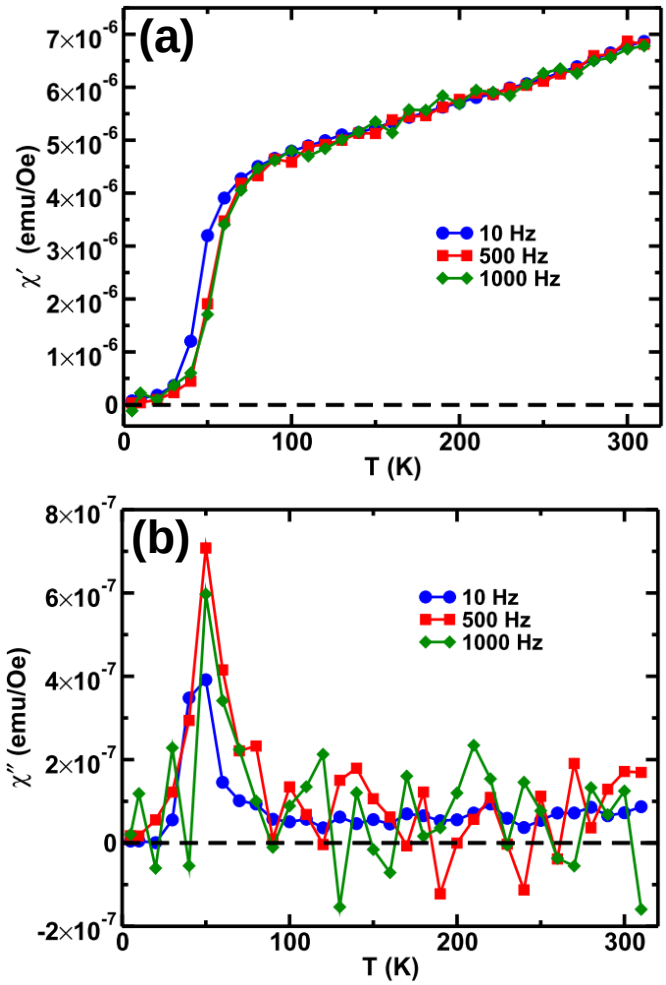

Figure 3.18: AC susceptibility data for the $Ni_{80}Fe_{20}$ nano-stripes in the transverse field configuration showing the (a) in-phase (χ′) and the (b) out-of-phase (χ″) signals at measuring frequencies of 10, 500 and 1000 Hz (error bars are smaller than the symbols)

among the crystallites was present perpendicular to the stripe axis and along the magnetic field axis. So the blocking temperature was considerably lower than that in the case of the parallel configuration because of the depinning of the domains in the side areas at low thermal energy and the magnitude of the in-phase and out-of-phase signal was also order of magnitude less than that in parallel configuration because most of the response was coming from the side regions only.

3.2.3.2 DC susceptibility Analysis

As the temperature started increasing in the presence of the applied magnetic field, the ZFC magnetization rose abruptly until 40 K (Fig. 3.19). However, the FC and the ZFC magnetization did not merge until the maximum temperature of 400 K. This big difference between FC and ZFC measurements emerged because of the local field result-

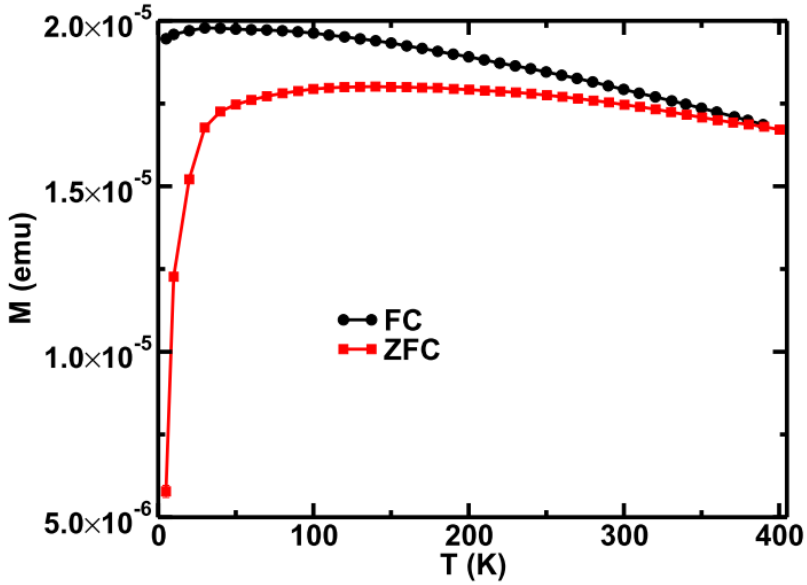

Figure 3.19: Low-field (100 Oe) ZFC and FC temperature dependence of magnetization for the $Ni_{80}Fe_{20}$ nano-stripes in the transverse field configuration(error bars are smaller than the symbols)

ing from the interaction between the neighbouring stripes. As this magnetization needed more energy as compared to that in the case of the parallel configuration, the magnetization increased a little until 120 K. After this temperature, a competition between the relaxation of more domains and the thermal fluctuations resulted in a slow decrease in the ZFC curve. The overall moment of the film was considerably higher in the case of the FC DC susceptibility measurement because during the field-cooling, the domains were freezing under the influence of the applied magnetic field.

3.2.3.3 Hysteresis loops

While coercivity was present at 5 K, 10 K and 20 K, by 50 K the coercivity was no longer measureable. At lower temperatures, the available thermal energy was enough to overcome the anisotropy barrier of the smaller domains only so higher magnetic field was required to attain the maximum magnetization in the sample. At higher temperature,

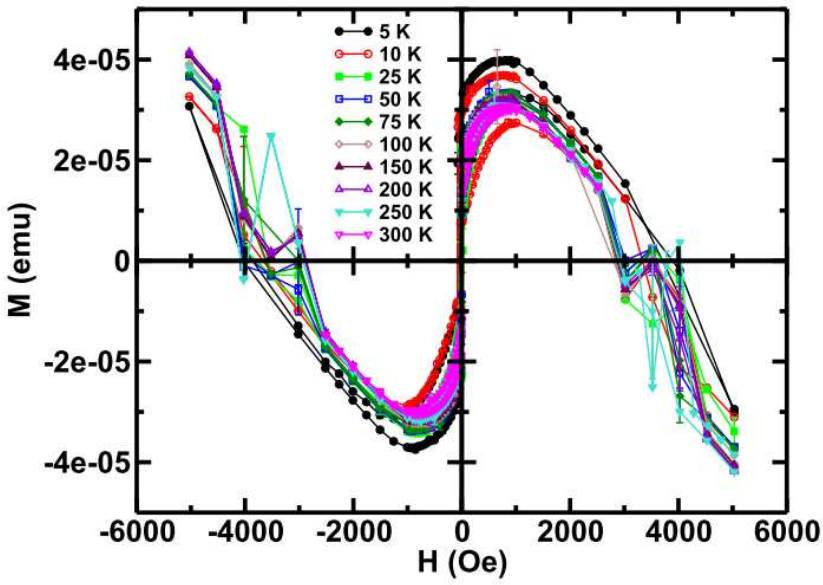

Figure 3.20: Hysteresis loops (20 kOe field-cooled) for the $Ni_{80}Fe_{20}$ nano-stripes in a transverse configuration before subtracting the high field susceptibility.

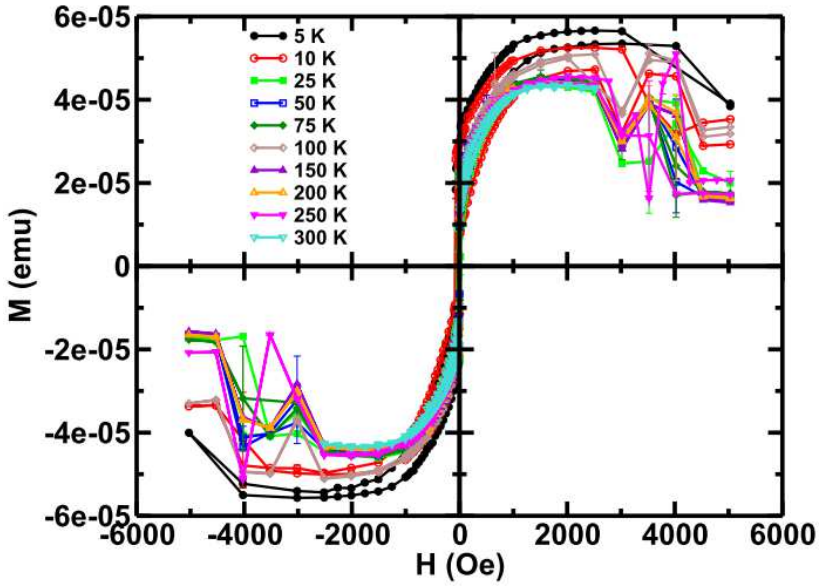

Figure 3.21: Hysteresis loops (20 kOe field-cooled) for the $Ni_{80}Fe_{20}$ nano-stripes in a transverse configuration after subtracting the high field susceptibility.

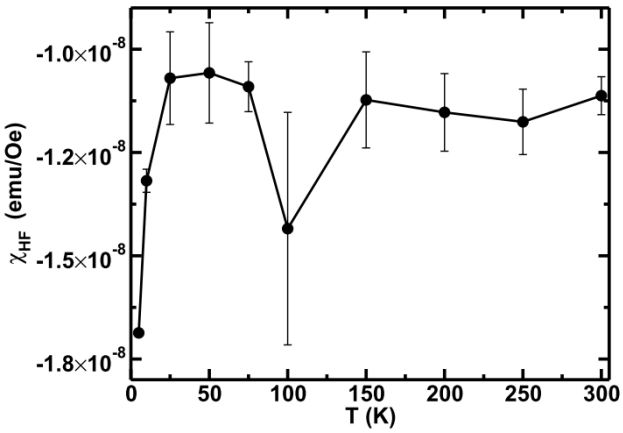

Figure 3.22: High-field diamagnetic susceptibility (χ_{HF}) from the substrate and the sample holder assembly

the thermal energy was large enough to overcome the anisotropy barrier of the larger domains and hence less magnetic field was required to achieve the maximum

magnetization of the sample. That is why the coercivity was at the maximum at 5 K and decreased with increase in temperature and eventually dropped to zero by 50 K.

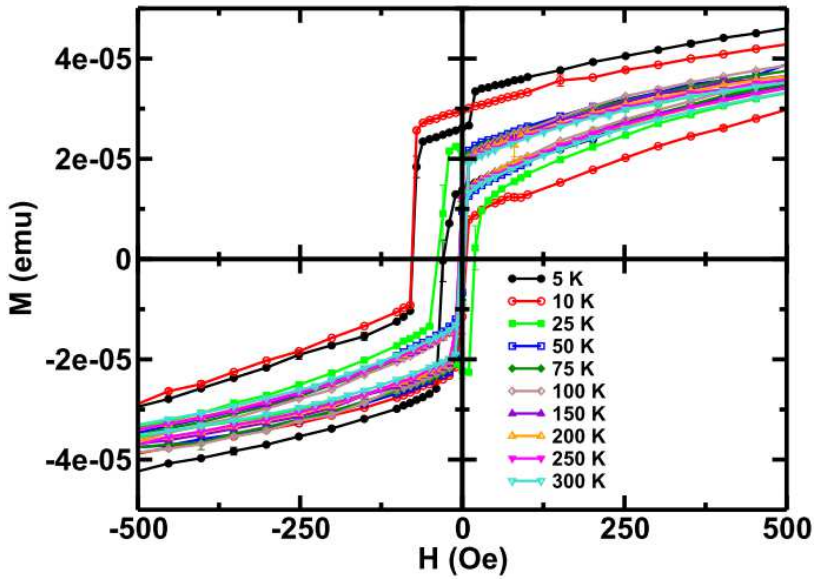

Figure 3.23: Hysteresis loop (20 kOe field-cooled) for the $Ni_{80}Fe_{20}$ nano-stripes in the transverse field configuration over ±500 Oe applied field range (error bars are smaller than the symbols)

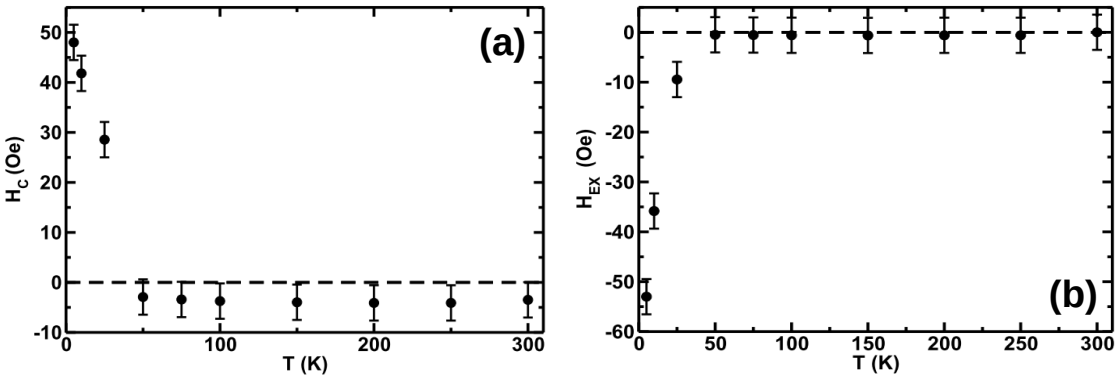

Figure 3.24: Temperature dependence of the (a) coercivity (H_C) and the (b) exchange bias field (H_{EX}) for the $Ni_{80}Fe_{20}$ nano-stripes in the transverse configuration.

The non-zero exchange bias field in the $Ni_{80}Fe_{20}$ nano-stripes in the transverse configuration (Fig. 3.24b) was, most likely, because of the surface effect [34, 35]. The surface magnetization was different from the bulk of the film and played an important role at low temperatures where thermal energy smaller than the surface anisotropy energy.

3.2.4 $Ni_{80}Fe_{20}$ nano-stripes in the perpendicular configuration

This section will deal with the magnetic characterization of the $Ni_{80}Fe_{20}$ nano-stripes in the out-of-plane/perpendicular applied field configuration taking the AC and the DC susceptibility measurements, and the hysteresis loops into account.

3.2.4.1 AC susceptibility Analysis

Neither the in-phase nor the out-of-phase data showed any temperature or frequency dependent change. As the demagnetization field was significantly large in this field configuration, the actual field determining the magnetization was much smaller than the applied field which resulted in a very low magnetic response to the applied field.

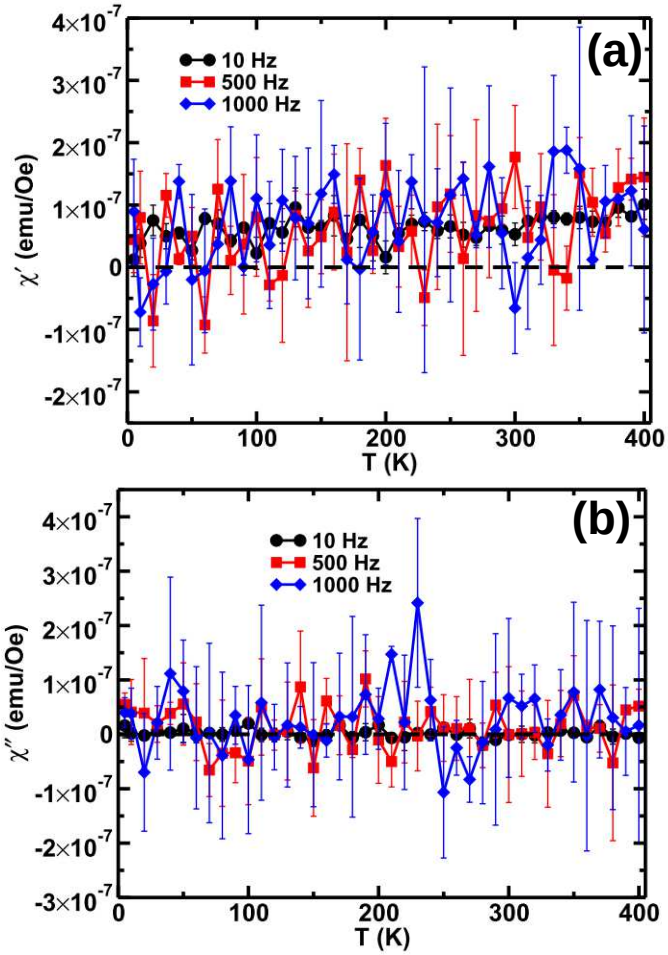

Figure 3.25: AC susceptibility data for the $Ni_{80}Fe_{20}$ nano-stripes in the perpendicular configuration showing the (a) in-phase (χ′) and the (b) out-of-phase (χ″) signals at measuring frequencies of 10, 500 and 1000 Hz

3.2.4.2 DC susceptibility Analysis

The ZFC and the FC data (Fig. 3.26) showed a gradually decreasing trend, a characteristic of ferromagnetic material. However since the ZFC and the FC measurements were almost the same, the domains remained aligned with applied magnetic field. Thinner than the critical diameter, the film along the applied field and the hard-axis magnetization resulted in a very low magnetization of the sample as compared

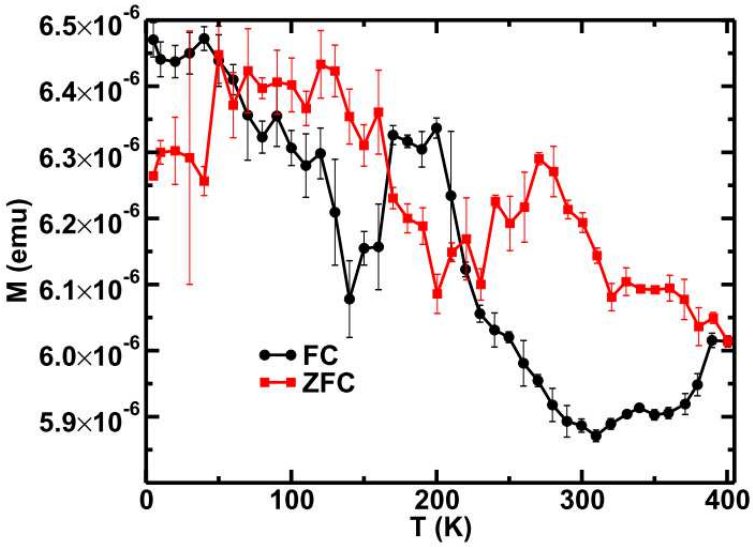

Figure 3.26: Low-field (100 Oe) ZFC and FC temperature dependence of magnetization for the $Ni_{80}Fe_{20}$ nano-stripes in the perpendicular configuration.

to the parallel and the transverse configuration (as suggested by the AC susceptibility measurement).

3.2.4.3 Hysteresis loops

Figure 3.27 shows hysteresis loops at different temperatures for the $Ni_{80}Fe_{20}$ nano-stripes after field-cooling the film in the perpendicular configuration. Since the substrate was out-of-plane with the applied field, we did not see any high field negative susceptibility. Figure 3.28 shows the same hysteresis loops in the applied field range $\pm$1000 Oe. Due to the small thickness of the material along the applied field direction, surface effects played an important role and a coercivity (Fig. 3.29a) was measured over the complete temperature range. The exchange bias field was zero throughout the experiment (Fig. 3.29b) which was because the pinning ability of the surface was not as strong as in the case of the near-pattern film as a consequence of the irregularity in the

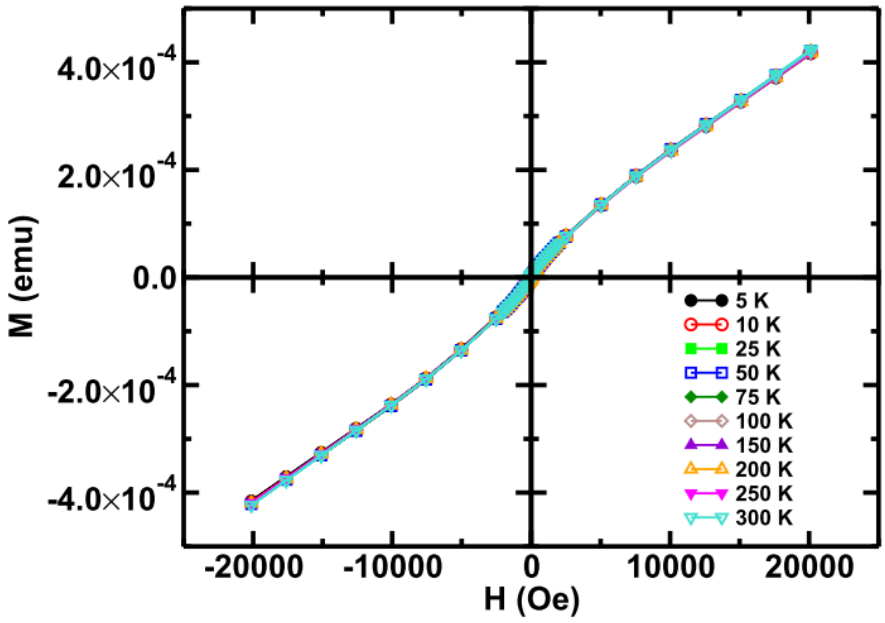

Figure 3.27: Hysteresis loops (20 kOe field-cooled) for the $Ni_{80}Fe_{20}$ nano-stripes in the perpendicular configuration (error bars are smaller than the symbols)

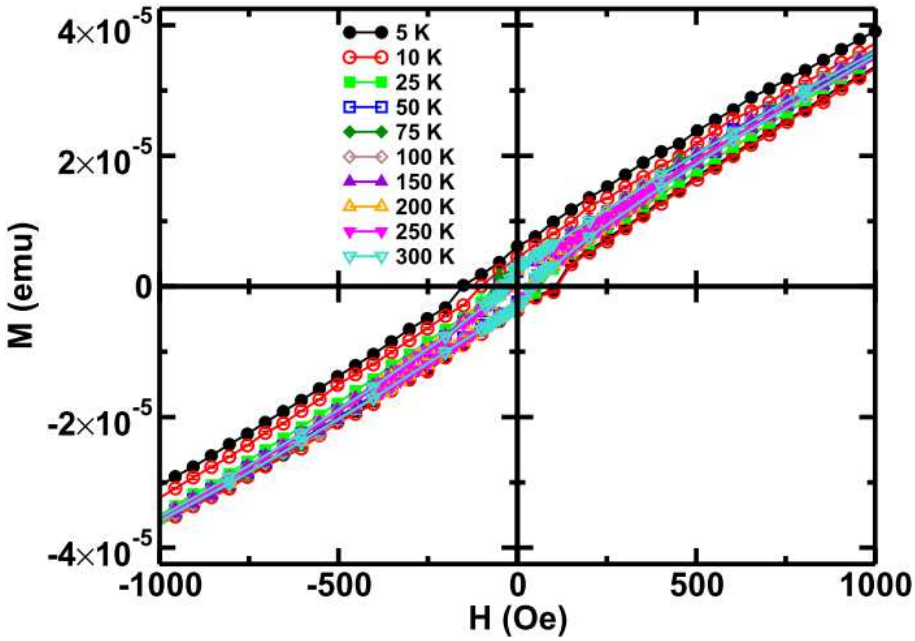

Figure 3.28: Hysteresis loops (20 kOe field-cooled) for the $Ni_{80}Fe_{20}$ nano-stripes in the perpendicular configuration over a ±1000 Oe applied field range

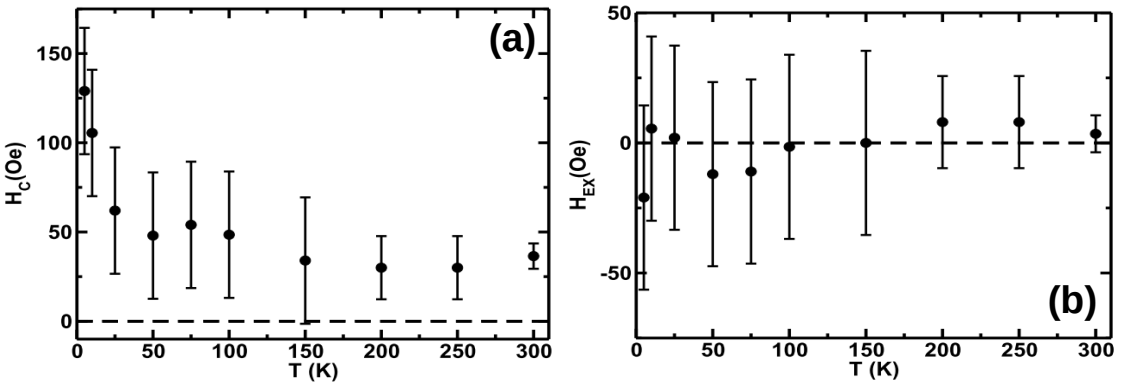

Figure 3.29: Temperature dependence of the (a) coercivity (H_C) and the (b) exchange bias field (H_{EX}) for the $Ni_{80}Fe_{20}$ nano-stripes in the perpendicular configuration.

surface caused by the stripes. The surface irregularity resulting from the pattern along with negligible effect of the coupling between the stripes in the perpendicular field configuration resulted in the exchange bias field not being measurable.

Chapter Four: $Ni_{80}Fe_{20}$/ NiO nano-stripes

4.1 Structural Characterization

The structural characterization of the $Ni_{80}Fe_{20}$/NiO nano-stripes was done at the Department of Materials Science and Engineering, National Chung Hsing University (NCHU), Taiwan by Hsuan-Rong Huang under the supervision of Dr. Ko-Wei Lin.

4.1.1 Micro-structural Characterization

A scanning electron microscopy (SEM) study showed a 10 nm separation (valley) between the 66 nm wide $Ni_{80}Fe_{20}$/NiO nano-stripes (Fig. 4.1b). Figure 4.1a and 4.1b shows the cross-sectional and the planar view of the nano-stripes, respectively. A cross-sectional view of a single nano-stripe is presented in the inset of Fig. 4.1a. Results showed that the thickness of the deposited material was 39 nm at the top, 18 nm at the sides and 20 nm in the space between the stripes.

Figure 4.2 shows the transmission electron microscope (TEM) bright-field (a) and dark-field (b) images of $Ni_{80}Fe_{20}$/NiO near-pattern film. The polycrystalline film with the

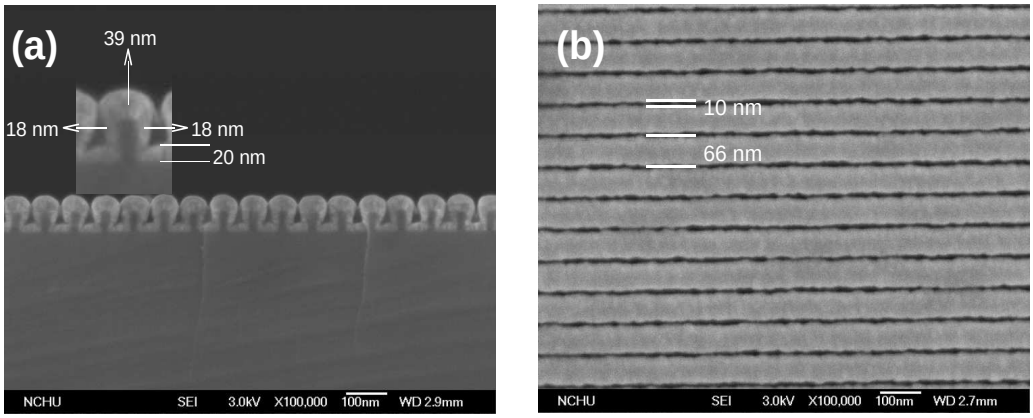

Figure 4.1: SEM images of the $Ni_{80}Fe_{20}$/NiO nano-stripes (a) cross-sectional view, a single stripe is shown in the inset with the thickness of the deposited region. (b) planar view, width of the stripe and the valley is shown.

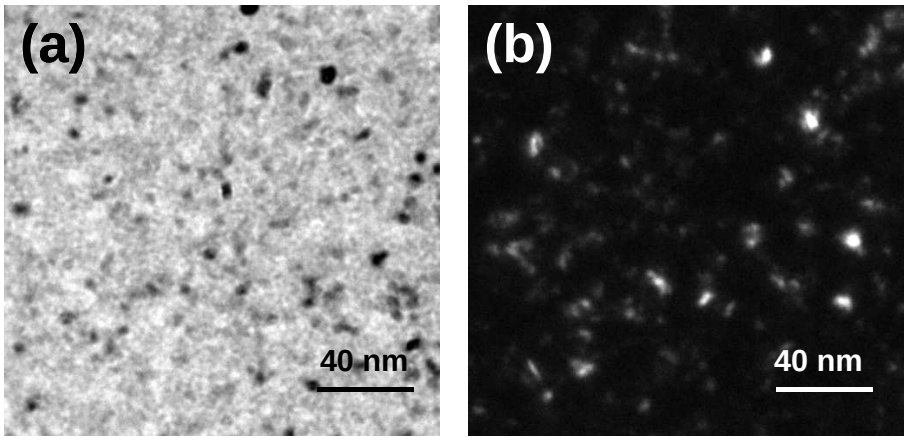

Figure 4.2: The (a) bright field and the (b) dark-field TEM images of the $Ni_{80}Fe_{20}$/NiO near-pattern film

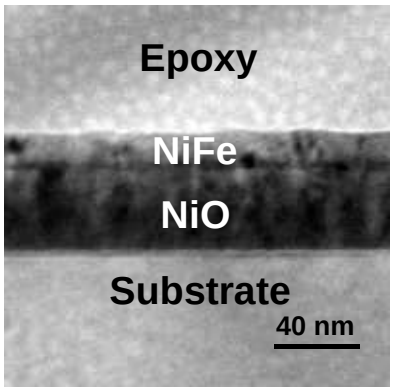

Figure 4.3: TEM image showing the cross-section of the $Ni_{80}Fe_{20}$/NiO near-pattern film

crystallite sizes between 2 nm and 9 nm was observed. Figure 4.3 shows a cross-section of the $Ni_{80}Fe_{20}$/NiO near-pattern film. The thickness of the $Ni_{80}Fe_{20}$ layer was 17 nm and that of NiO layer was 34 nm.

4.2 Magnetic Characterization

The magnetic characterization of the $Ni_{80}Fe_{20}$/NiO nano-stripes was performed in the field configurations similar to the $Ni_{80}Fe_{20}$ nano-stripes in the previous chapter. The

magnetic characterization of the near-pattern film was done to compare and understand the magnetization behaviour of the stripes. The near-pattern film was only characterized in the in-plane configuration because the demagnetization field was the only difference between the in-plane and out-of-plane configuration.

4.2.1 $Ni_{80}Fe_{20}$/NiO near-pattern film

In this section, the magnetic characterization of the $Ni_{80}Fe_{20}$/NiO near-pattern film is discussed which encompasses the AC and the DC susceptibility measurements and the hysteresis loops.

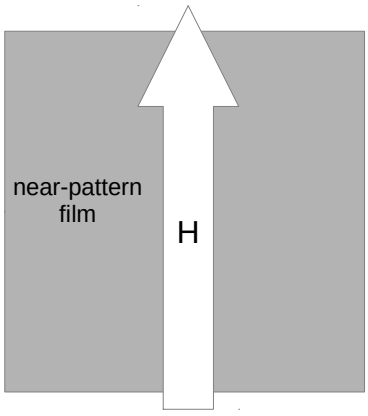

Figure 4.4: The $Ni_{80}Fe_{20}$/NiO near-pattern film and the magnetic field (H) configuration

4.2.1.1 AC susceptibility analysis

The in-phase AC susceptibility data (Fig. 4.5a) shows an increasing trend over the temperature range of the measurement because the domains continued to relax as the temperature increased from 5 K. However, due to the exchange coupling between the $Ni_{80}Fe_{20}$ and the NiO layer, the magnetic response was orders of magnitude less than that for $Ni_{80}Fe_{20}$ near-pattern film. The out-of-phase AC susceptibility shows an upward trend

at ~350 K which may be because of reduced Néel temperature and the small grain size of NiO crystallites [70, 71].

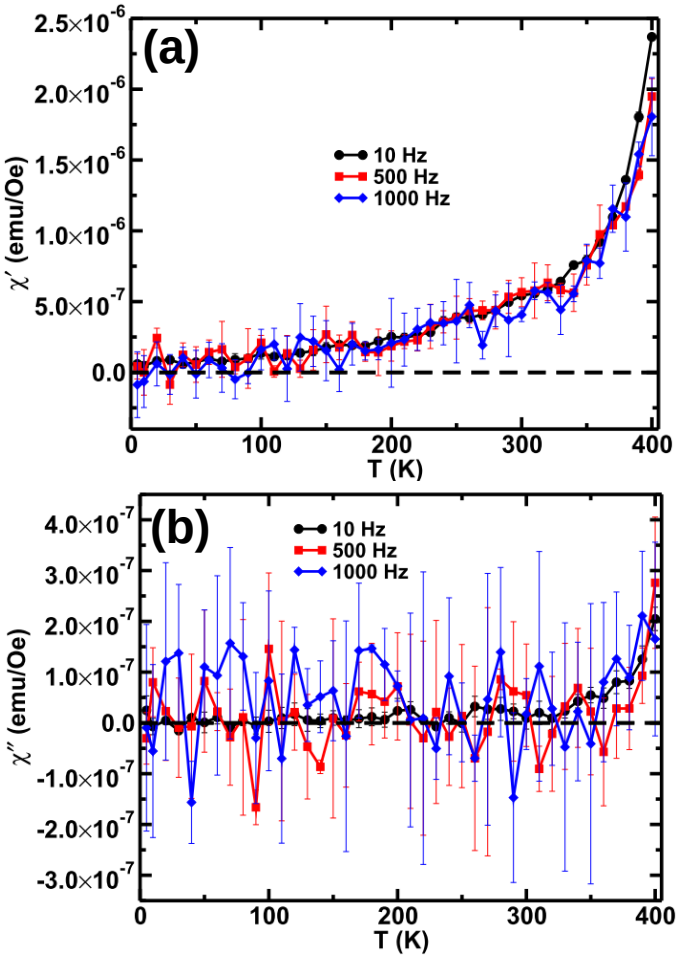

Figure 4.5: AC susceptibility data for the $Ni_{80}Fe_{20}$/NiO near-pattern film showing the (a) in-phase (χ′) and the (b) out-of-phase (χ″) data at measuring frequencies of 10, 500 and 1000 Hz

4.2.1.2 DC susceptibility analysis

Figure 4.6 shows the ZFC and the FC temperature dependence of magnetization. The Néel temperature of NiO is 525 K [54] and the Curie temperature of the $Ni_{80}Fe_{20}$ is 853 K [73] so no magnetic transition was expected in our experimental range of the

temperature. As the temperature was made to increase from 5 K (Fig. 4.6), domains started aligning along the applied field resulting in the increase in the overall moment of the film. The ZFC magnetization changed very slowly between 50 K and 150 K which might be because of the requirement of the energy to overcome the pinning of the domains at the $Ni_{80}Fe_{20}$-NiO interface.

The exchange coupling and the distribution of the grain size at the interface resulted in a distribution of the strength of the $Ni_{80}Fe_{20}$-NiO coupling at the interface. This distribution in the exchange coupling strength resulted in the distribution of the number of $Ni_{80}Fe_{20}$ domains aligning along the applied field. The requirement of different energy values to align the $Ni_{80}Fe_{20}$ domains along the field resulted in a plateau

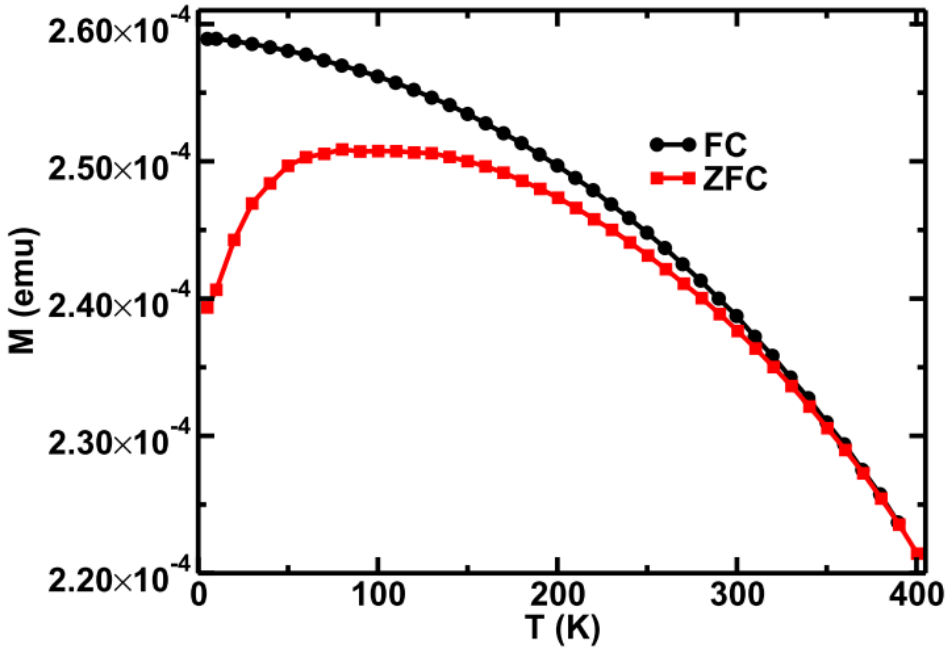

Figure 4.6: Low-field (100 Oe) ZFC and FC temperature dependence of the magnetization for the $Ni_{80}Fe_{20}$/NiO near-pattern film parallel to H. (error bars are smaller than the symbols)

in the ZFC measurement (Fig. 4.6). With an increase in the temperature, random thermal fluctuations in the $Ni_{80}Fe_{20}$ layer resulted in a decrease in the sample magnetization. At 350 K, the ZFC and the FC curves merged together which indicated that no irreversibility in the magnetization should be expected at and above 350 K in the presence of 100 Oe applied field. For the FC measurement, as the temperature started decreasing from 400 K, the magnetization of the sample started increasing because of the decrease in the thermal fluctuations. At 350 K, a bifurcation of the ZFC and the FC measurements was noticed because the applied magnetic field continued to align the $Ni_{80}Fe_{20}$ domains during the cooling process and hence the magnetization of the sample in the FC measurement was considerably larger than that in the ZFC measurement.

4.2.1.3 Hysteresis loops

Figure 4.7 shows hysteresis loops for the $Ni_{80}Fe_{20}$/NiO near-pattern film at different temperatures. The noisy data at high magnetic fields resulted from SQUID's response to the overwhelming diamagnetic signal from the substrate and the sample holder assembly. Subtraction of the high field susceptibility (Fig. 4.8) yielded the hysteresis loops shown in Fig. 4.9 while Fig. 4.10 shows the same hysteresis loops over the applied field range from -400 Oe to +200 Oe.

A non-zero coercivity was noticed at 5 K, 10 K and 25 K. However, at 50 K, the coercivity vanished. This behaviour was likely because of the crystallite size distribution in the $Ni_{80}Fe_{20}$ film with the same reasoning described for the coercivity behaviour of the $Ni_{80}Fe_{20}$ near-pattern film in the section 3.2.1.3. The exchange bias field did not drop to zero within the temperature range of the measurement because the Néel temperature of NiO (525 K [74]) was greater than the maximum temperature (400 K) and hence the NiO

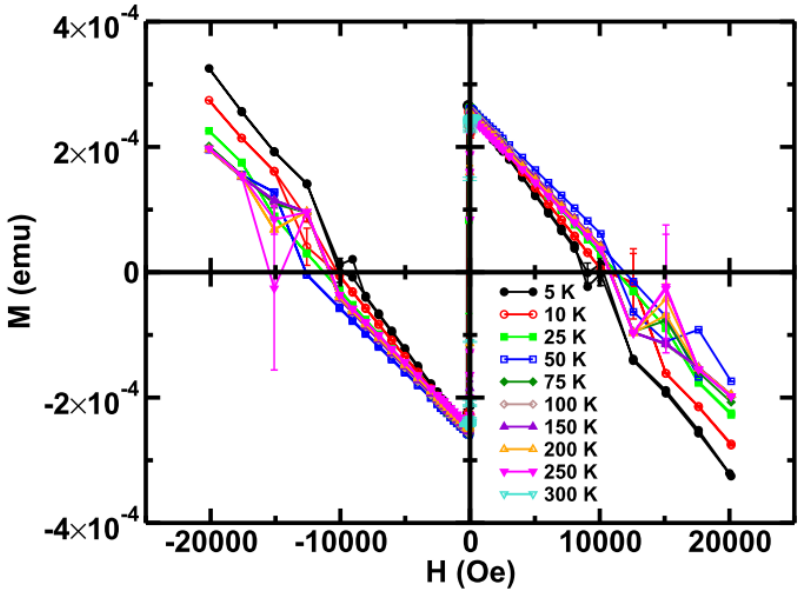

Figure 4.7: Hysteresis loops (20 kOe field-cooled) for the $Ni_{80}Fe_{20}$/NiO near-pattern film before subtracting the high field susceptibility.

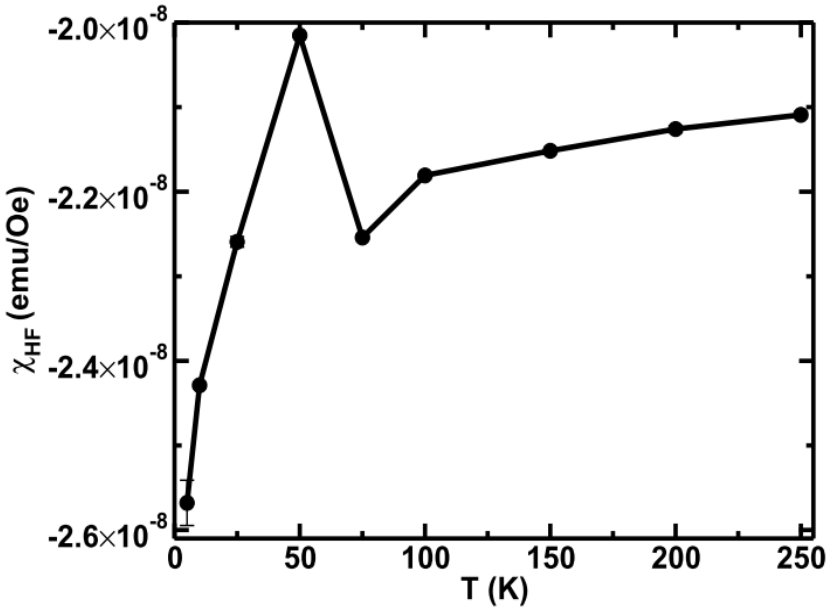

Figure 4.8: High-field diamagnetic susceptibility (χ_{HF}) from the substrate and the sample holder assembly

domains were frozen in the temperature range of the measurement.

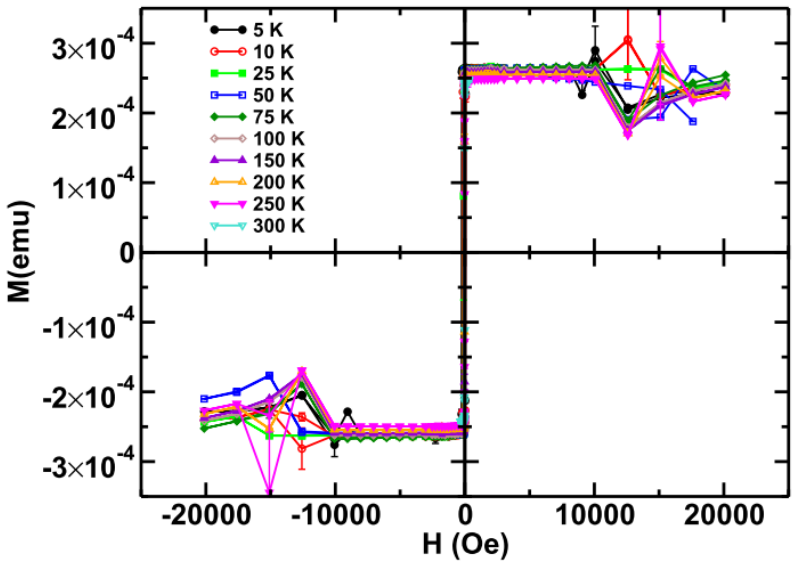

Figure 4.9: Hysteresis loops (20 kOe field-cooled) for the $Ni_{80}Fe_{20}$/NiO near-pattern film after subtracting the high field susceptibility.

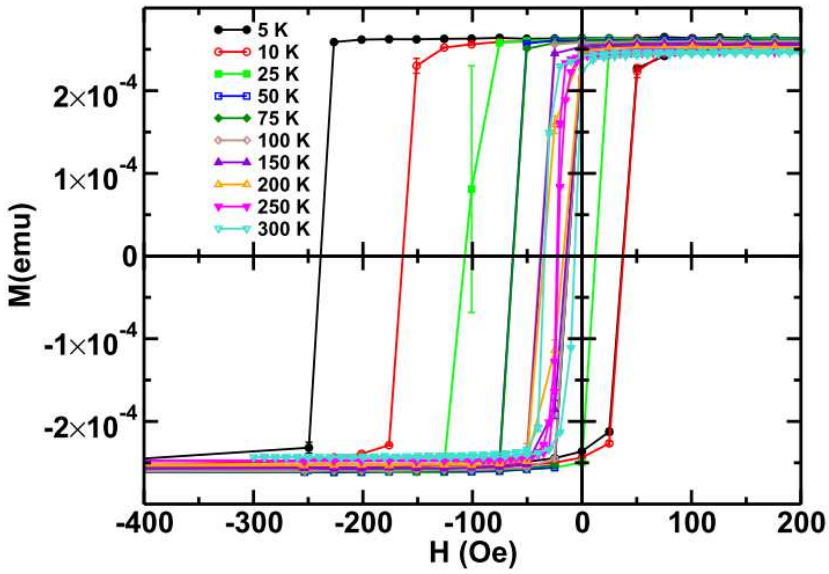

Figure 4.10: Hysteresis loop (field-cooled 2 kOe) for the $Ni_{80}Fe_{20}$/NiO near-pattern film in the field range -400 Oe to 200 Oe (error bars are mostly smaller than the symbols)

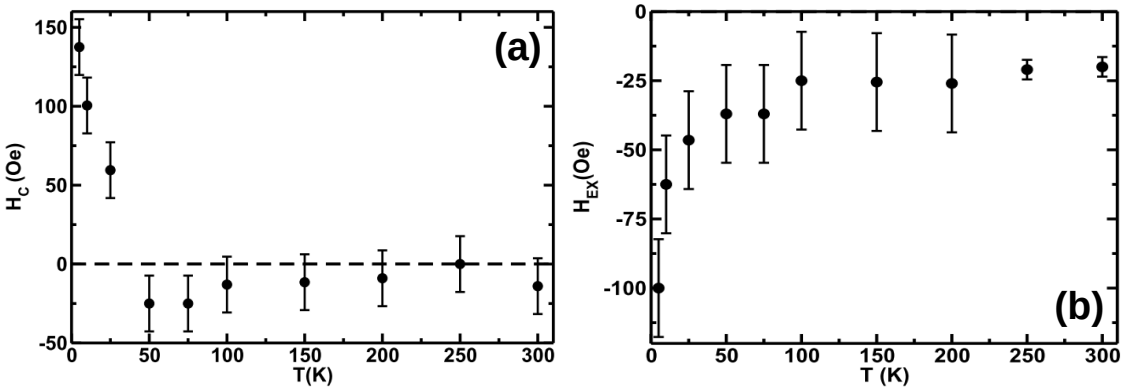

Figure 4.11: Temperature dependence of (a) the coercivity (H_C) and (b) the exchange bias field (H_{EX}) for the $Ni_{80}Fe_{20}$/NiO near-pattern film

4.2.2 $Ni_{80}Fe_{20}$/NiO nano-stripes in the parallel configuration

This section will encompass the magnetic characterization of the $Ni_{80}Fe_{20}$/NiO nano-stripes in the parallel field configuration (Fig. 4.12), describing the AC and the DC susceptibility measurements and hysteresis loops.

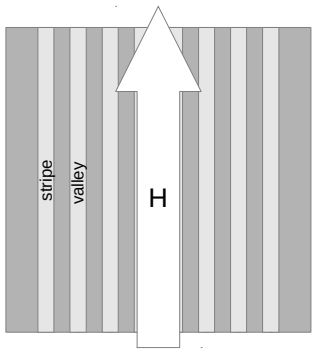

Figure 4.12: The $Ni_{80}Fe_{20}$ nano-stripes in the parallel field configuration

4.2.2.1 AC susceptibility analysis

The in-phase and the out-of-phase AC susceptibility (Fig. 4.13) did not show any change in the temperature range of the measurement. In the parallel configuration, the applied AC field tried to oscillate the domains along the preferred direction of

magnetization, i.e. the easy axis which needed high energy as seen in the case of the $Ni_{80}Fe_{20}$ nano-stripes in the parallel configuration. In addition to this easy-axis magnetization, exchange coupling between the $Ni_{80}Fe_{20}$ and the NiO layer also offered resistance to the domains' response in accordance with the applied alternating field. As a result, neither the in-phase nor the out-of-phase AC susceptibility showed any change in the temperature range of the measurement.

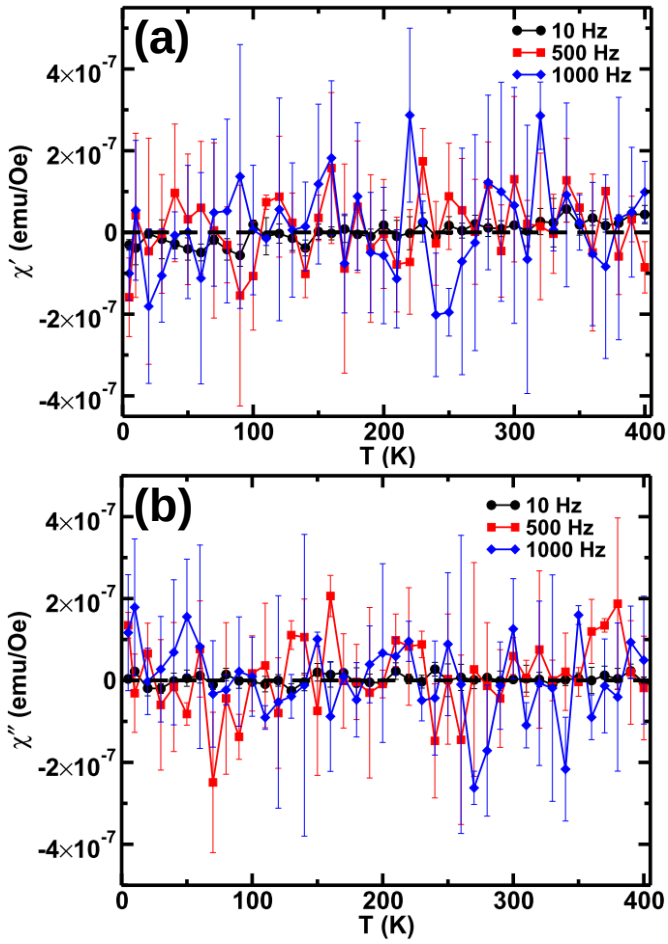

Figure 4.13: AC susceptibility data for the $Ni_{80}Fe_{20}$/NiO nano-stripes in the parallel configuration showing the (a) in-phase (χ′) and the (b) out-of-phase (χ″) signals with measuring frequencies 10, 500 and 1000 Hz

4.2.2.2 DC susceptibility analysis

The ZFC DC susceptibility data (Fig. 4.14) showed very small changes in the magnetization of the sample until 60 K. Since the stripes of width 66 nm were 10 nm apart, in addition to the exchange coupling between the $Ni_{80}Fe_{20}$ and the NiO layer, strong magnetic coupling between the stripes offered resistance to the alignment of the domains by the applied field. By 70 K, the overall magnetization of the film started decreasing because of the thermal fluctuations. At 350 K, the ZFC and the FC magnetizations merged, indicating the irreversibility of magnetization beyond that temperature in the presence of a 100 Oe applied magnetic field. As the film was cooled from 400 K for the FC measurement, a decrease in the thermal fluctuations resulted in a gradual increase in the overall magnetization of the film. Since the domains were freezing

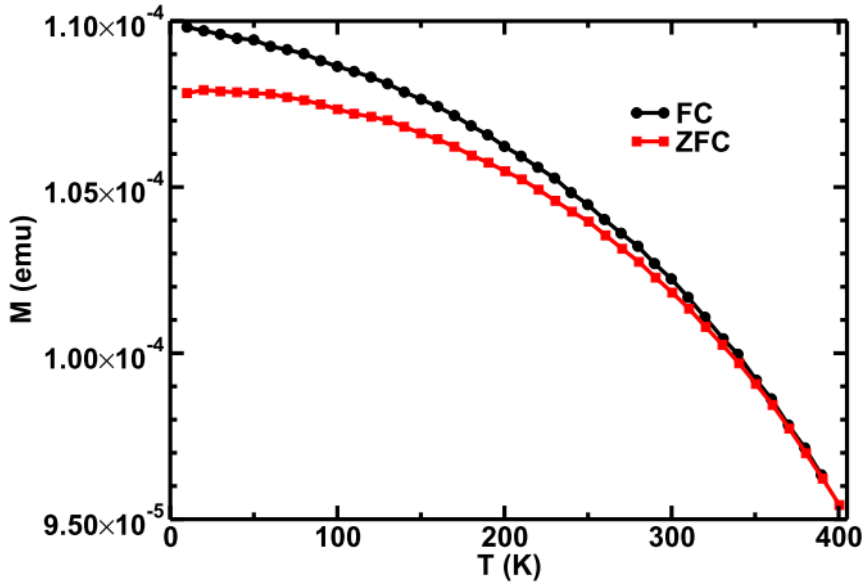

Figure 4.14: Low-field (100 Oe) ZFC and FC temperature dependence of the magnetization of the $Ni_{80}Fe_{20}$/NiO nano-stripes in the parallel field configuration. (error bars are smaller than the symbols)

under the influence of the applied field during the cooling process, the FC measurement showed a increasing magnetization of the film at the temperatures below the bifurcation of the ZFC and the FC data at 350 K.

4.2.2.3 Hysteresis loops

Like the $Ni_{80}Fe_{20}$ nano-stripes in the parallel field configuration, the shape of the hysteresis loops suggested clearly two magnetic phases in the sample, i.e. applied field dependence of the magnetization from a patterned area with stripes and the near-pattern area around the stripes. As the applied field changed its polarity, the magnetization in the near-pattern region aligned along the applied field. However, due to the exchange coupling between the $Ni_{80}Fe_{20}$ and the NiO layer and the magnetic coupling between the stripes, the reversal of the domains and their propagation along the stripe was blocked. As a result, the magnetization was different over the applied range from -750 Oe to -1000 Oe as compared to that over the range from -1000 Oe to -750 Oe. The same was observed along the positive applied field axis. The couplings between the stripes and between the layers resulted in non-zero coercivity over the temperature range of the measurement (Fig. 4.19a). The non-zero exchange bias field over the temperature range of the measurement showed that NiO magnetization was not affected by the magnetic field and continued to provide exchange coupling to the $Ni_{80}Fe_{20}$ film. The exchange coupling between the two layers resulted in enhanced exchange bias field as compared to the $Ni_{80}Fe_{20}$ nano-stripes in the parallel field configuration because the exchange coupling between the $Ni_{80}Fe_{20}$ and the NiO layer was stronger than the surface effect in the case of the $Ni_{80}Fe_{20}$ nano-stripes in the parallel configuration.

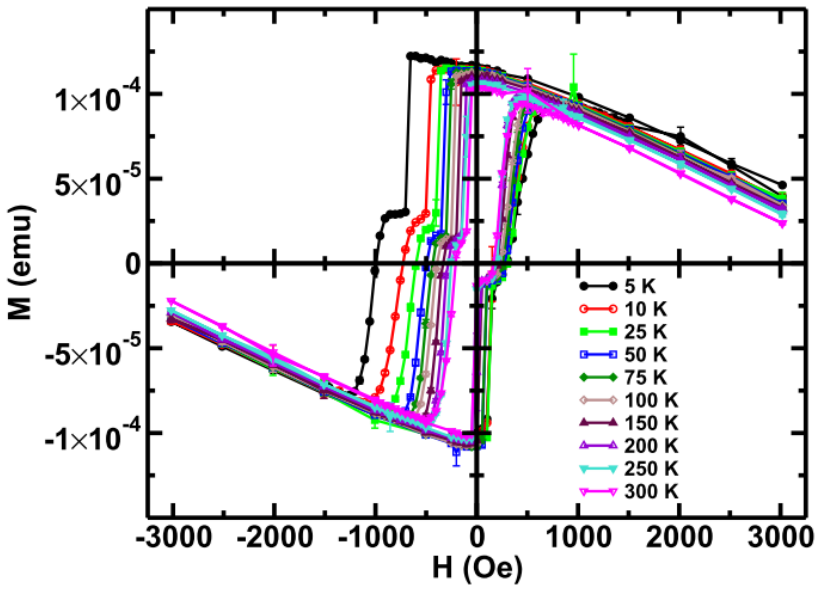

Figure 4.15: Hysteresis loops (20 kOe field-cooled) for the $Ni_{80}Fe_{20}$/NiO nano-stripes in a parallel configuration before subtracting the high field susceptibility.

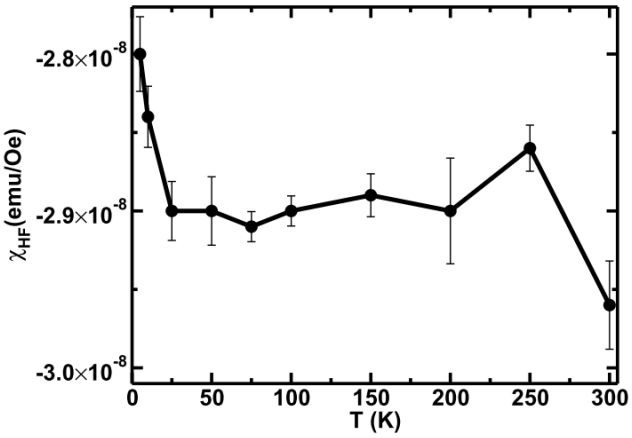

Figure 4.16: High-field diamagnetic susceptibility (χ_{HF}) from the substrate and the sample holder assembly

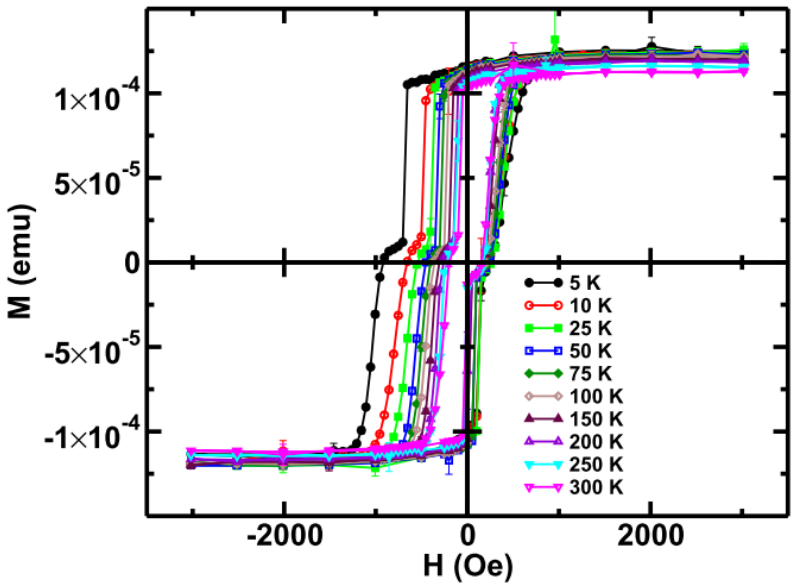

Figure 4.17: Hysteresis loops (20 kOe field-cooled) for the $Ni_{80}Fe_{20}$/NiO nano-stripes in a parallel configuration after subtracting the high field susceptibility.

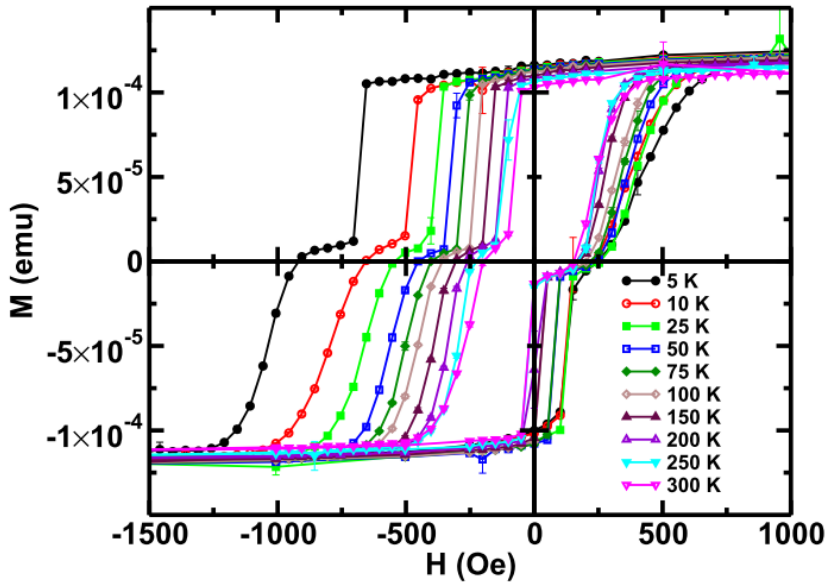

Figure 4.18: Hysteresis loops (20 kOe field-cooled) for the $Ni_{80}Fe_{20}$/NiO nano-stripes in the parallel field configuration over the applied field range -1500 Oe to 1000 Oe.

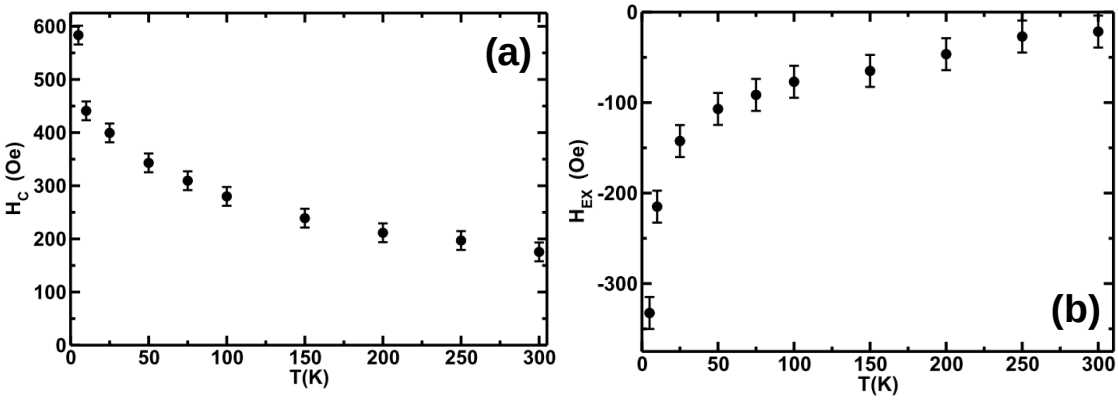

Figure 4.19: Temperature dependence of (a) the coercivity (H_C) and (b) the exchange bias field (H_{EX}) for the $Ni_{80}Fe_{20}$/NiO nano-stripes in the parallel configuration

4.2.3 $Ni_{80}Fe_{20}$/NiO nano-stripes in the transverse configuration

This section will describe the magnetic characterization of the $Ni_{80}Fe_{20}$/NiO nano-stripes in the transverse configuration (Fig. 4.20) describing the AC and the DC susceptibility measurements and the hysteresis loops.

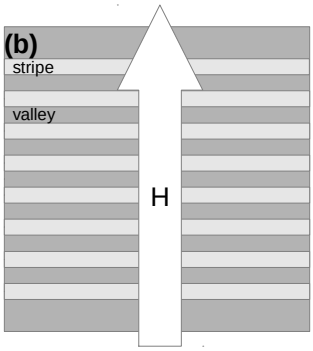

Figure 4.20: The $Ni_{80}Fe_{20}$ nano-stripes in the transverse field configuration

4.2.3.1 AC susceptibility analysis

The in-phase AC susceptibility (Fig. 4.21a) continued to increase in the temperature range of the measurement as the domains continued to relax with the

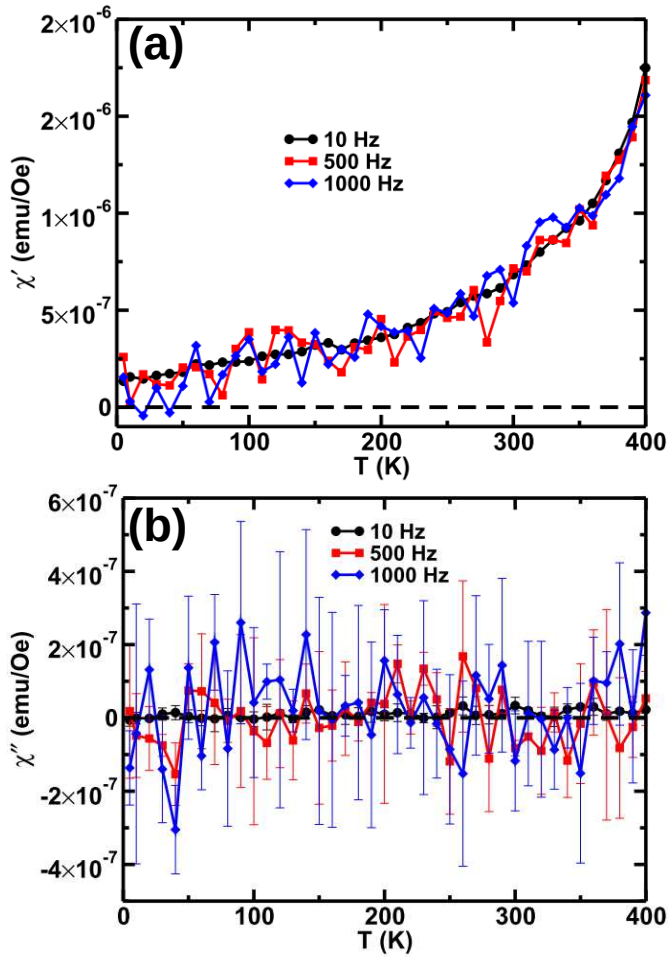

Figure 4.21: AC susceptibility data for the $Ni_{80}Fe_{20}$/NiO nano-stripes in the transverse field configuration showing the (a) in-phase (χ′) and the (b) out-of-phase (χ″) signals at measuring frequencies of 10, 500 and 1000 Hz

increase in the temperature. Due to the small spacing between the stripes, the magnetic coupling between them was strong. The near-pattern region, hence, was mainly responsible for the in-phase signal. Despite the strong magnetic coupling between the stripes, some of the domains in the patterned area were able to respond to the oscillating magnetic field, as shown by the in-phase AC susceptibility measurement.

4.2.3.2 DC susceptibility analysis

For the ZFC measurement, as the temperature was increased after applying the magnetic field in the transverse configuration, the domains started relaxing and aligning along the applied field, resulting in a continuous rise in the magnetization of the film. This continuous rise indicated the blocking of the domains' magnetization. This blocking could be attributed to two factors. One factor was the magnetic coupling between the stripes which needed more energy to be overcome. The second factor was the exchange coupling between the $Ni_{80}Fe_{20}$ and the NiO layer. This coupling acted as a hindrance to the alignment of the domains along the applied field. The FC measurement yielded a higher magnetization as compared to the ZFC measurement because during the cooling process, the domains were freezing with their alignment set by the applied field.

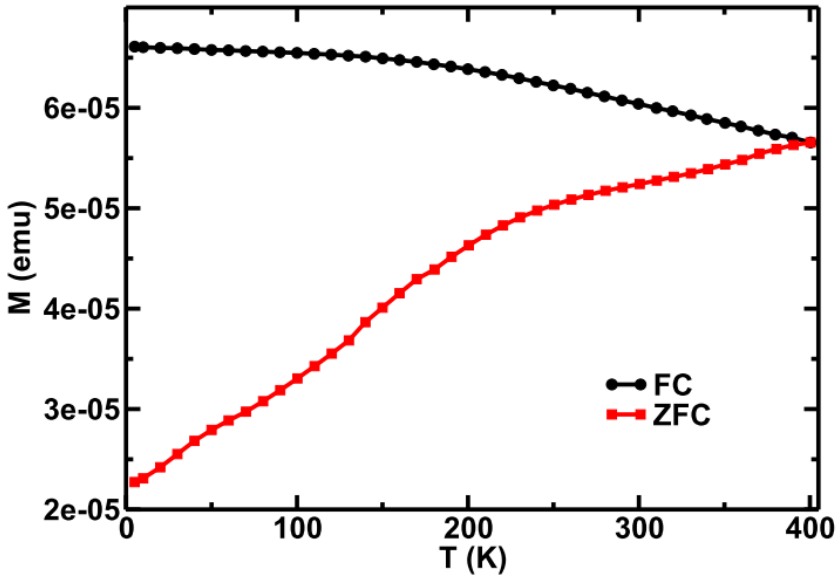

Figure 4.22: Low-field (100 Oe) ZFC and FC temperature dependence of the magnetization for the $Ni_{80}Fe_{20}$/NiO nano-stripes in the transverse field configuration (error bars are smaller than the symbols)

Since the exchange coupling between the $Ni_{80}Fe_{20}$ and the NiO layer was the same as that in parallel configuration, the magnetization perpendicular to the stripe axes and the demagnetization field was the reason for the magnetization of the film being lower than that for the parallel configuration (Fig. 4.13) over the temperature range of the measurement.

4.2.3.3 Hysteresis loops

Consider the hysteresis loop at 5 K (Fig. 4.25). Field cooling caused the alignment of the domains in the NiO film to some extent because field cooling was started from a temperature (400 K) below the Néel temperature of NiO (525 K [74]). This alignment resulted in a preferred direction of magnetization through the exchange coupling between the $Ni_{80}Fe_{20}$ and the NiO film at the interface. As the magnetic field reversed its direction, the magnetization did not follow because of the magnetic coupling between the stripes. This coupling was mainly between the side areas of neighbouring stripes as those were the areas along the applied field direction. Due to the size distribution of the crystallites and the coupling between the stripes, the magnetization switching was gradual as shown by the loop.

The exchange coupling between the $Ni_{80}Fe_{20}$ and the NiO layer resulted in an enhanced coercivity as compared to the $Ni_{80}Fe_{20}$ nano-stripes in the transverse configuration because due to the exchange coupling between the $Ni_{80}Fe_{20}$ and the NiO layer, higher magnetic field was required to switch the $Ni_{80}Fe_{20}$ magnetization in the film as compared to the $Ni_{80}Fe_{20}$ nano-stripes. This exchange coupling also resulted in enhanced exchange bias field as compared to the $Ni_{80}Fe_{20}$ nano-stripes for the same

reason. With the increase in the temperature, both the coercivity and the exchange bias field continued to decrease because more and more thermal energy was available to

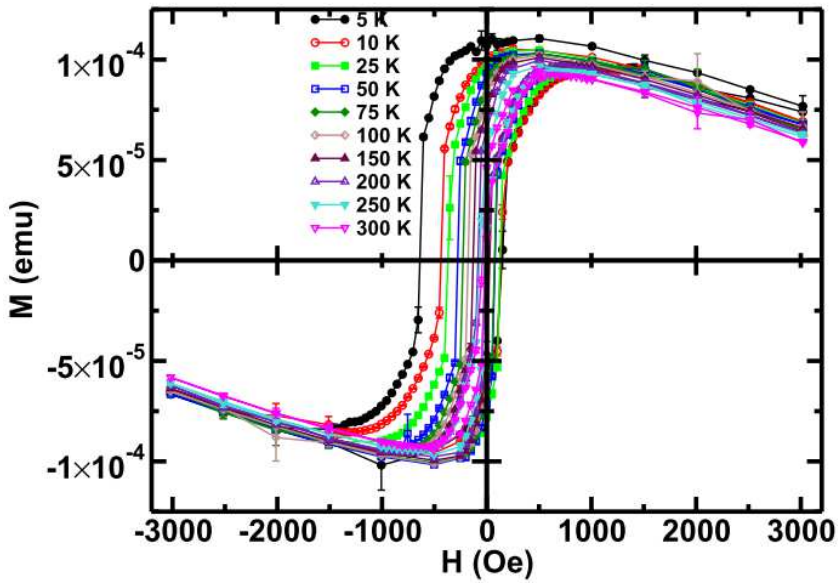

Figure 4.23: Hysteresis loops (20 kOe field-cooled) for the $Ni_{80}Fe_{20}$/NiO nano-stripes in a transverse configuration, before subtracting the high field susceptibility.

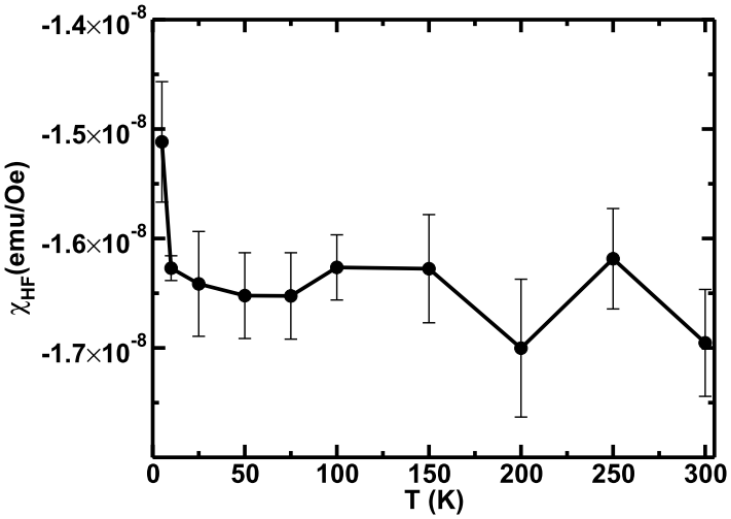

Figure 4.24: High-field diamagnetic susceptibility (χHF) from the substrate and the sample holder assembly

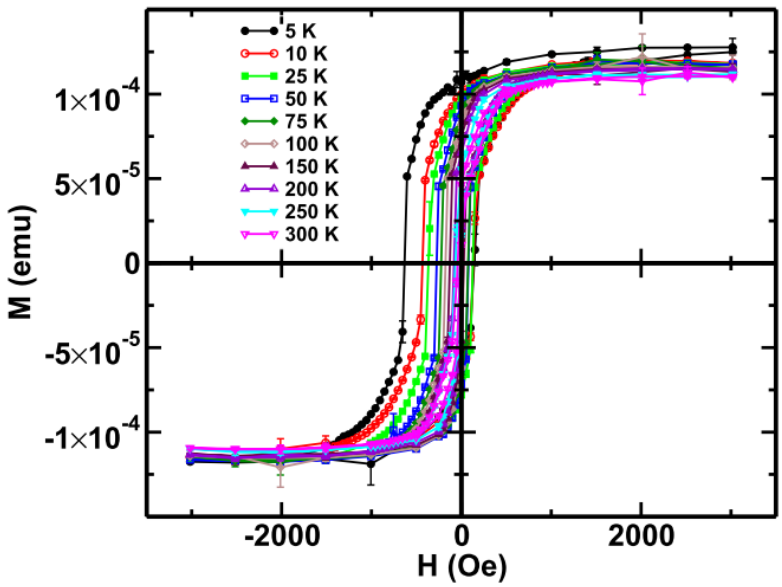

Figure 4.25: Hysteresis loops (20 kOe field-cooled) for the $Ni_{80}Fe_{20}$/NiO nano-stripes in a transverse configuration, after subtracting the high field susceptibility.

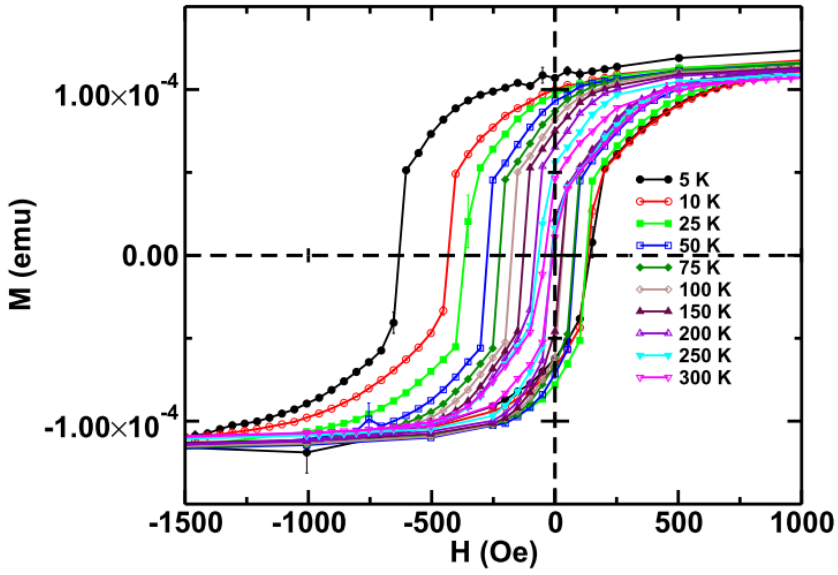

Figure 4.26: Hysteresis loop (20 kOe field-cooled) for $Ni_{80}Fe_{20}$/NiO nano-stripes in transverse configuration over the applied field range -1500 Oe to 1000 Oe.

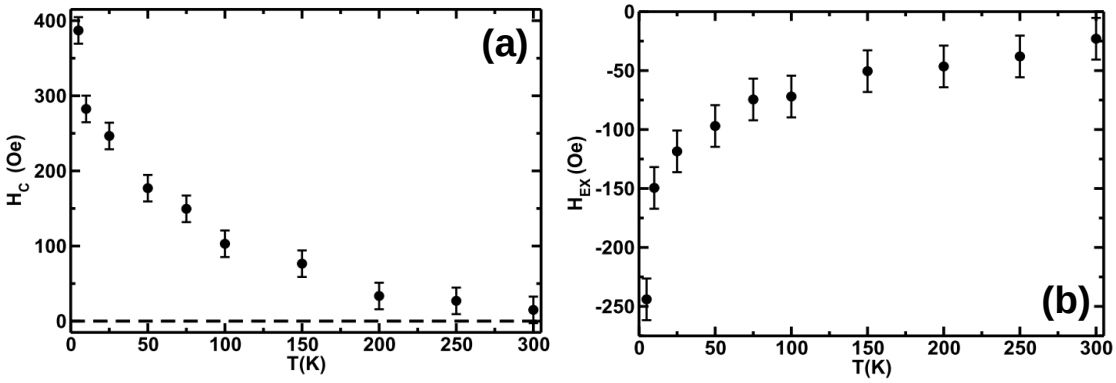

Figure 4.27: Temperature dependence of (a) the coercivity (H_C) and (b) the exchange bias field (H_{EX}) for the $Ni_{80}Fe_{20}$/NiO nano-stripes in the transverse configuration.

overcome the exchange coupling between the two layers and the anisotropy barriers of the domains.

4.2.4 $Ni_{80}Fe_{20}$/NiO nano-stripes in the perpendicular configuration

This section will describe the magnetic characterization of the $Ni_{80}Fe_{20}$/NiO nano-stripes in the perpendicular configuration taking into account the AC and the DC susceptibility measurements and the hysteresis loops. Figure 4.28 shows the schematic of the nano-stripes in the perpendicular field configuration.

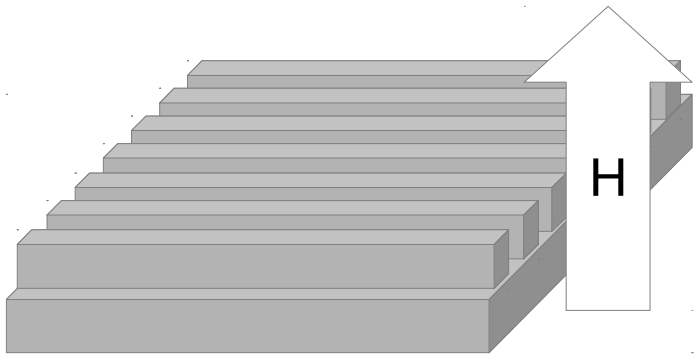

Figure 4.28: The $Ni_{80}Fe_{20}$/NiO nano-stripes in the perpendicular field configuration

4.2.4.1 AC susceptibility analysis

Neither the in-phase (Fig. 4.29a) nor the out-of-phase (Fig. 4.29b) data for the $Ni_{80}Fe_{20}$/NiO nano-stripes in the perpendicular configuration showed any temperature or frequency dependent change. This indicated that the superparamagnetic blocking temperature was higher than the maximum temperature of the measurement.

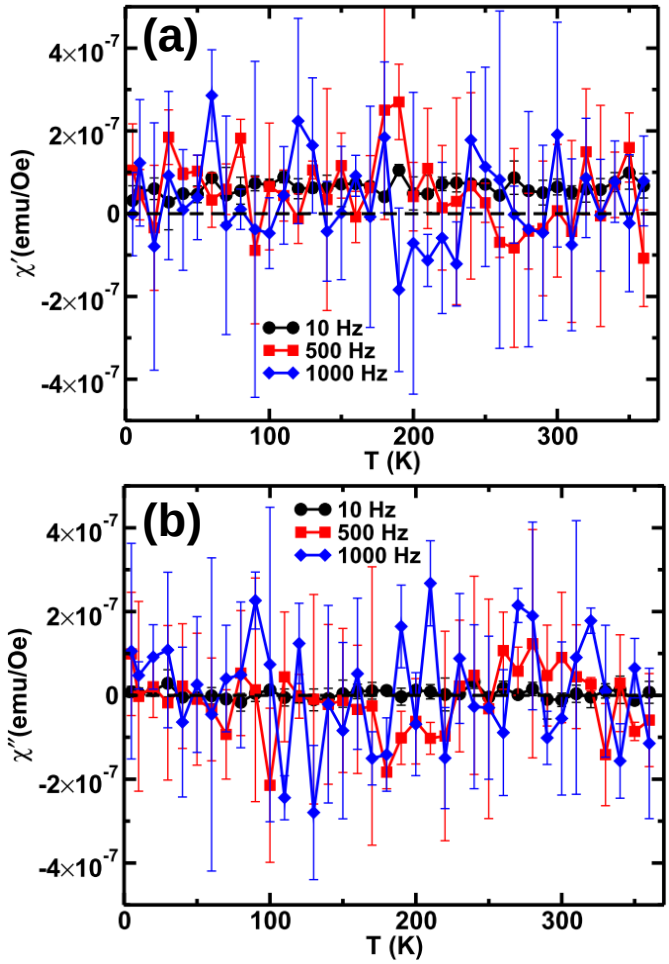

Figure 4.29: AC susceptibility data for the $Ni_{80}Fe_{20}$/NiO nano-stripes in the perpendicular configuration showing the (a) in-phase (χ′) and the (b) out-of-phase (χ″) signals at measuring frequencies of 10, 500 and 1000 Hz

4.2.4.2 DC susceptibility analysis

As the temperature was made to increase after applying magnetic field perpendicular to the plane of the film, increasing thermal energy continued to overcome the anisotropy barriers of the domains and the magnetization of the film kept increasing. The increasing trend in the ZFC measurement (Fig. 4.30), until 260 K, was likely because of relaxation of the domains in the near-pattern area of the film. The magnetization of the film remained almost stable from 260 K to 330 K. This was likely because of the relatively stronger pinning of the domains in the patterned region resulting from, in addition to the exchange coupling between the two layers, the magnetic coupling between the stripes and the magnetocrystalline anisotropy as the magnetic field was applied perpendicular to the easy-axis of the stripe-magnetization. At 330 K, the thermal energy was enough to overcome the anisotropy barriers in the domains in the patterned area and

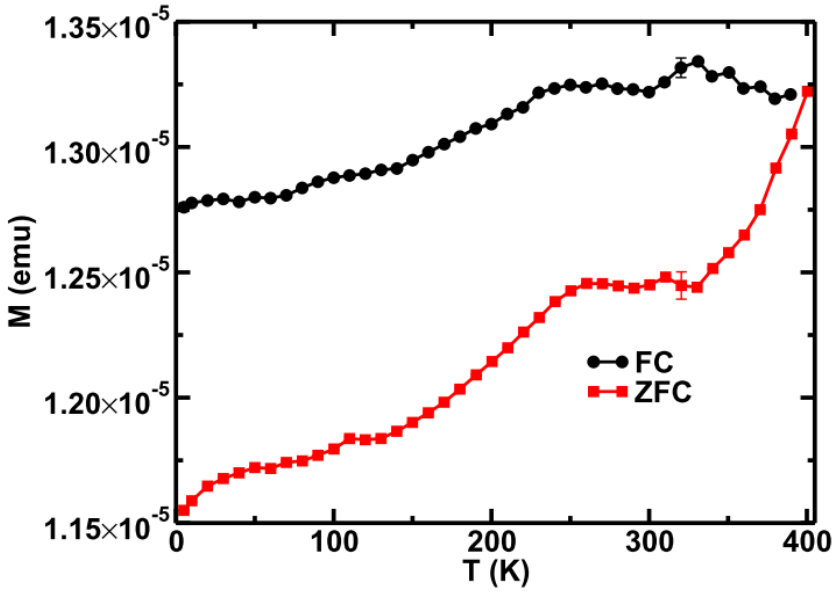

Figure 4.30: Low-field (100 Oe) ZFC and FC temperature dependence of the magnetization for the $Ni_{80}Fe_{20}$/NiO nano-stripes in the perpendicular configuration.

an increase was observed in the ZFC measurement till 400 K. As the film was cooled from 400 K for the FC measurement, cooling of the domains in the patterned area under the influence of the applied field resulted in a small increase in the magnetization of the sample. Since the magnetic field was applied perpendicular to the plane of the film, the exchange coupling between the $Ni_{80}Fe_{20}$ and the NiO layer had a profound influence on the magnetization of the sample. The magnetization of the sample, after a small decrease, remained stable from 330 K to 230 K because the exchange coupling affected the domains alignment as the thermal fluctuations reduced as a result of the decrease in the temperature. However as the temperature was decreased below 230 K and the thermal fluctuations decreased further, a competition between the magnetic field and the exchange coupling between the two layers resulted in a gradual decrease in the magnetization of the film. A large demagnetization field along with the exchange coupling between the $Ni_{80}Fe_{20}$ and the NiO layer resulted in a low magnetization of the film as compared to the same film in the parallel and the transverse configuration. This will be discussed later in the Discussion of Results (Chapter 5).

4.2.4.3 Hysteresis loops

Figure 4.31 shows hysteresis loops at different temperatures for the $Ni_{80}Fe_{20}$ nano-stripes. No high field negative susceptibility was measured because the substrate was out-of-plane with applied field. Figure 4.32 shows the same hysteresis loops in the applied field range $\pm$1000 Oe. Due to the small thickness of the material along the applied field, exchange coupling between the two layers played an important role and non-zero coercivity (Fig. 4.33a) was noticed in the temperature range of the measurement. The

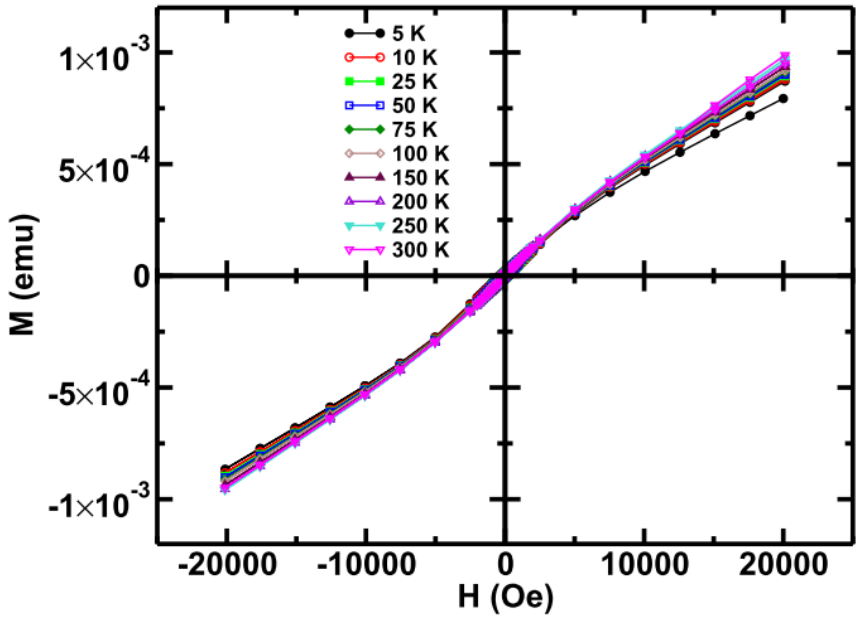

Figure 4.31: Hysteresis loops (20 kOe field-cooled) for the $Ni_{80}Fe_{20}$/NiO nano-stripes in the perpendicular configuration (error bars are smaller than the symbols)

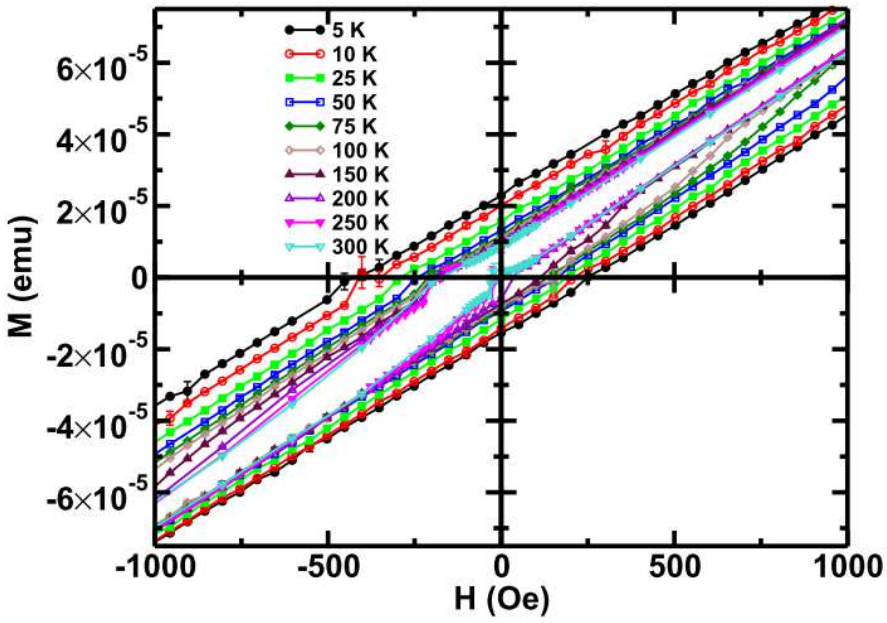

Figure 4.32: Hysteresis loops (20 kOe field-cooled) for the $Ni_{80}Fe_{20}$/NiO nano-stripes in the perpendicular configuration over a ±1000 Oe applied field range

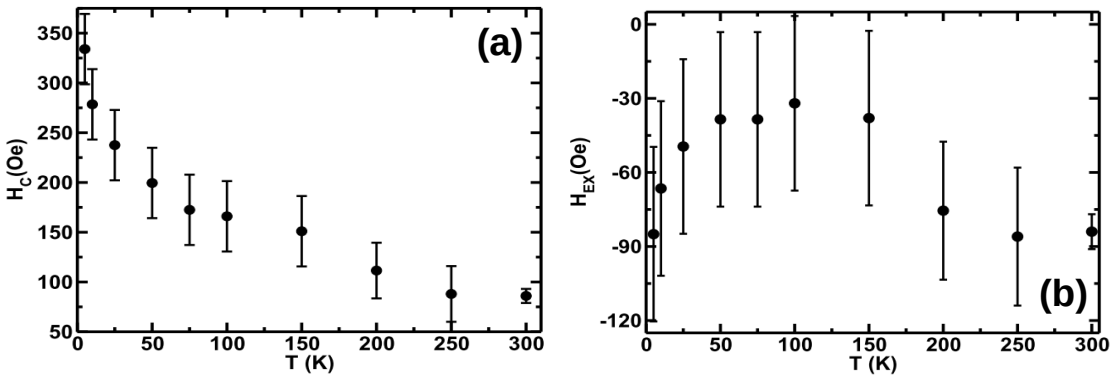

Figure 4.33: Temperature dependence of (a) the coercivity (H_C) and (b) the exchange bias field (H_{EX}) for the $Ni_{80}Fe_{20}$/NiO nano-stripes in the perpendicular field configuration.

coercivity continued to decrease with the increase in the temperature because of the increasing thermal energy to overcome the anisotropy barriers in the film. The exchange bias field was very small through-out the experiment (Fig. 4.33b) which was because of the existence of the stripes and the strong demagnetization field. The pinning ability of the surface was not as strong as in the case of the near-pattern film because of the irregularity resulting from the pattern. Furthermore, the sample was not saturated because of the demagnetization field. This surface irregularity along with negligible effect of the coupling between the stripes in the perpendicular field configuration and the unsaturated sample resulted in very small exchange bias field over the temperature range of the measurement (Fig. 4.33b).

The magnitude of the exchange bias field decreased until 150 K; however, at 200 K the exchange bias field magnitude increased and did not change at 250 K and 300 K. This happened because, until 200 K, main contribution to the exchange bias field was coming from the near-pattern region while the magnetic coupling between the stripes was

strong enough to be overcome by the low magnetic field (lower than the coercive field). As the temperature neared 200 K, the thermal energy was enough to overcome the anisotropy barriers of the domains in the nano-stripes. This contribution from the stripes at higher temperatures, already discussed in detail in the DC susceptibility analysis, played an important role in the magnetic behaviour of the sample by enhancing the pinning of the domains.

Chapter Five: Discussion of the Results

The change of the magnetization from blocked to the superparamagnetic was studied by employing AC and DC susceptibility measurement techniques. Figure 5.1 shows the in-phase and the out-of-phase AC susceptibility data for the $Ni_{80}Fe_{20}$ near-pattern film and the nano-stripes in the parallel and the transverse field configurations at

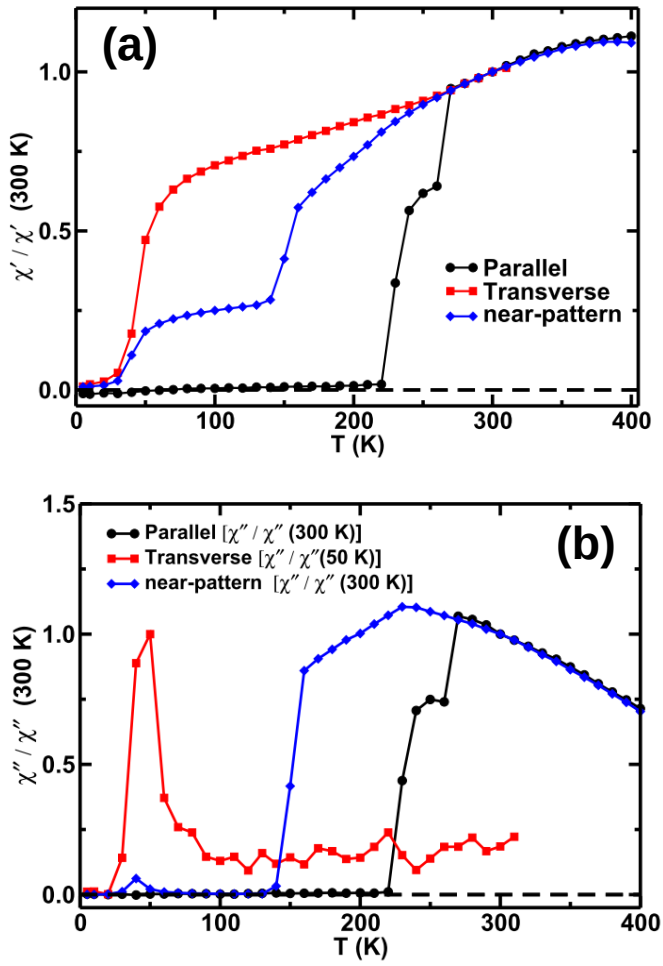

Figure 5.1: The (a) in-phase (χ′) and the (b) out-of-phase (χ″) AC susceptibility measurement (normalized to 300 K) for the $Ni_{80}Fe_{20}$ nano-stripes in the parallel and the transverse configuration and near-pattern film at 10 Hz (error bars are smaller than the symbols).

10 Hz. The data are normalized to 300 K to allow comparison. The in-phase AC susceptibility data showed two changes for the near-pattern at about 50 K and 150 K and for the transverse configuration near 50 K. The out-of-phase AC susceptibility data also showed the same behaviour. The AC susceptibility of nano-stripes in the parallel configuration showed an abrupt rise at 220 K which was also evident in the out-of-phase AC susceptibility scan. However, none of these changes seemed to be a magnetic transition since they were not found at the same temperature in all configurations and they were frequency dependent. Furthermore, the AC susceptibility data for nano-stripes in the perpendicular configuration did not show any temperature or frequency dependent change. This claim is also supported by the fact that Curie temperature (T_C) of face-centered cubic $Ni_{80}Fe_{20}$ is 853 K [73]. These observations emphasize the role of stripes, the interaction between neighbouring nano-stripes and orientation of the nano-stripes with respect to the applied field. While the superparamagnetic blocking temperature (T_B) is 50 K in the case of the near-pattern film and the nano-stripes in the transverse configuration, the nano-stripes in the parallel configuration did not turn superparamagnetic till 220 K. This is also evident from the out-of-phase AC susceptibility. Due to the absence of any pattern, the crystallite size distribution appeared to be an important factor and resulted in a plateau in the in-phase AC susceptibility. However in the case of the nano-stripes, the amount of magnetic material in the direction of the field and the orientation of the nano-stripes with respect to the field were the important factors. The nano-stripes in the parallel and the transverse configurations will be discussed further in detail in context with the nano-stripes in the perpendicular configuration.

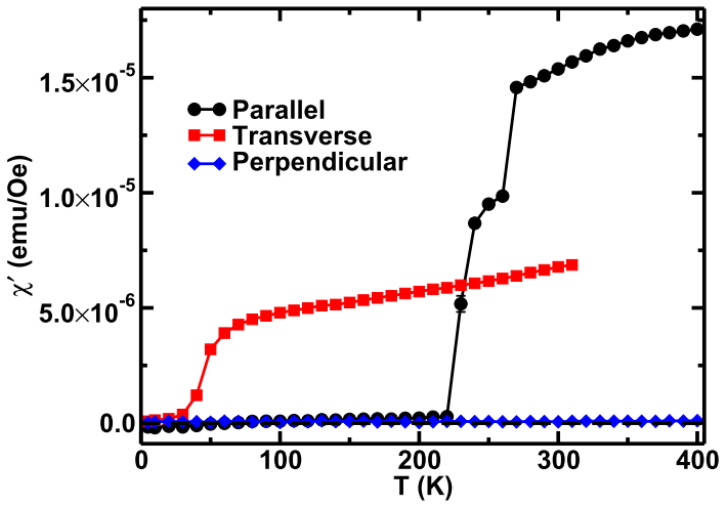

Figure 5.2: The in-phase (χ´) AC susceptibility data at 10 Hz for the $Ni_{80}Fe_{20}$ nano-stripes in the parallel, transverse and perpendicular field configurations (error bars are smaller than the symbols)

Figure 5.2 shows the in-phase AC susceptibility data for the $Ni_{80}Fe_{20}$ nano-stripes in the parallel, transverse and the perpendicular configuration at 10 Hz frequency. For the nano-stripes in the parallel configuration at 300 K, χ´ was more than double of that in the transverse configuration. On the other hand, the superparamagnetic blocking temperature in the transverse configuration was considerably smaller than that for the parallel configuration. The reason for this difference was that in the case of the parallel field configuration, the AC field attempted to oscillate the domains along the easy-axis, the preferred direction of magnetization. A strong coupling between the nano-stripes resulted in resistance from the domains to follow the applied AC field. On the other hand, in the case of the transverse field configuration, the field attempted to oscillate the domains along the hard axis. The coupling between the nano-stripes was not as strong as in the case of the parallel configuration. The amount of the magnetic material along the applied

field was considerably lesser than that in the case of the parallel field configuration. This was why the signal in the transverse field configuration was considerably smaller than that for the parallel configuration. Since the oscillating field attempted to oscillate the domains along the hard-axis, less thermal energy was required to overcome the coupling between the stripes as compared to that for the easy-axis (parallel configuration) and hence the superparamagnetic blocking temperature was very small (50 K) as compared to that for parallel field configuration (270 K).

The in-phase AC susceptibility data for $Ni_{80}Fe_{20}$/NiO nano-stripes and near-pattern film, however, showed entirely different behaviour. Figure 5.3 show a similarity between the nano-stripes in the transverse configuration and the near-pattern film. In the case of the near-pattern film, the field tried to oscillate the domains along the easy axis of the magnetization of the film. Due to the absence of a pattern, there was no blocking of the domains that could rise from the magnetic coupling between the stripes. The exchange coupling between the NiO and the $Ni_{80}Fe_{20}$ layers offered hindrance to the domains' response in accordance with the applied field. The pinned NiO and $Ni_{80}Fe_{20}$ domains at the interface do not follow the applied field and affect the neighbouring domains' response as well. With the increase in temperature, more and more energy was available to overcome the exchange coupling between the $Ni_{80}Fe_{20}$ and the NiO and hence the susceptibility continued to rise. In the case of the nano-stripes in the transverse configuration, the oscillating magnetic field caused the domains to fluctuate along the hard-axis of the magnetization of the stripes which were only 10 nm apart. Due to the very small spacing between the stripes, the magnetic interaction between the stripes was

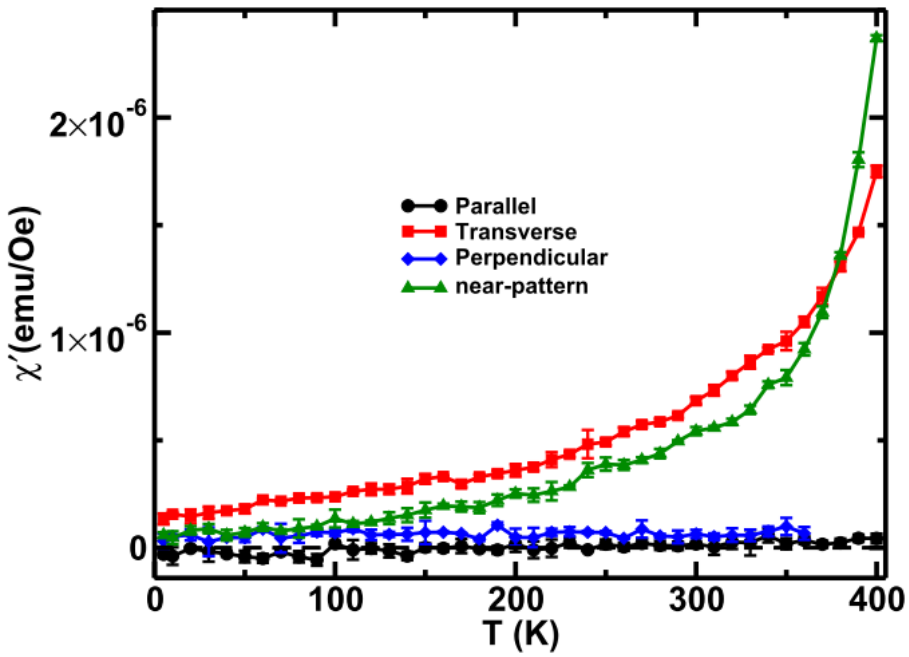

Figure 5.3: The in-phase (χ´) AC susceptibility data at 10 Hz for the Ni80Fe20/NiO near-pattern film and the nano-stripes in the parallel, transverse and the perpendicular field configuration

expected to be strong and hence the low 2.5 Oe AC magnetic field could not affect most of the domains in the stripes. The main contribution to the susceptibility was, therefore, from the near-pattern area of the film. That is why the in-phase data showed the same temperature dependent trend in both cases and almost the same magnitude of χ´. A slightly higher in-phase signal for the nano-stripes in the transverse configuration as compared to the near-pattern film till 370 K could be because of some contribution from the domains in the stripes which were along the magnetic field. However, at the temperatures higher than 370 K, χ´ for the near-pattern film was considerably higher than that for the nano-stripes in the transverse configuration. At high temperature, the weakening exchange coupling resulted in a quick rise in χ´; however, because of the

magnetic coupling between the stripes, the patterned area was not very responsive to the applied field. The nano-stripes in the parallel and the perpendicular configurations, however, showed negligible χ' in the temperature range of the measurement. In the case of the nano-stripes in the parallel configuration, the signal is low because the applied field attempted to oscillate the domains along the favourable direction of magnetization which resulted in very low signal because of the hindrance to domain fluctuations emerging from the magnetocrystalline anisotropy. In the case of the nano-stripes in the perpendicular configuration, the very small thickness of the magnetic material (less than the critical diameter) along the magnetic field resulted in very low signal because the $Ni_{80}Fe_{20}$ layer thickness was 16 nm and the single domain critical size for the $Ni_{80}Fe_{20}$ is 22 nm. In the case of the perpendicular configuration, the surface magnetization and the exchange coupling between the two layers played an important role so no change was observed in the temperature range of the measurement.

In the case of the $Ni_{80}Fe_{20}$ nano-stripes in the transverse field configuration, the temperature dependence of the coercivity and the exchange bias field showed that both the coercivity and the exchange bias field, just like those of near-pattern film, were not present at 50 K. The in-phase AC susceptibility also showed a frequency dependant change in the susceptibility at 50 K. In addition, the out-of-phase AC susceptibility showed maxima at ~50 K. These results all indicated the blocking temperature of 50 K for the nano-stripes. So at 50 K, the available thermal energy was enough to overcome the anisotropy barriers and domains were not pinned any more.

If we consider the $Ni_{80}Fe_{20}$ near-pattern film, the DC susceptibility data showed at 50 K the blocking temperature. This information was in agreement with the temperature

dependence of the coercivity and the AC susceptibility data. On the other hand, in the case of the $Ni_{80}Fe_{20}$ nano-stripes in the transverse configuration, both the coercivity and the AC susceptibility data showed T_B = 50 K which was not in agreement with the DC susceptibility data. In the case of the $Ni_{80}Fe_{20}$ nano-stripes in the parallel configuration, alignment of the nano-stripes along the applied magnetic field and the exchange coupling between the neighbouring nano-stripes made the difference of the nature (what is actually measured) of measurement techniques, i.e. DC susceptibility and AC susceptibility, more important. This strong interaction did not exist in the case of the near-pattern film and the nano-stripes in the transverse configuration; hence both the AC and DC magnetometery techniques, though different in nature, provided almost the same information about the blocking temperature.

Consider the DC susceptibility data for $Ni_{80}Fe_{20}$/NiO nano-stripes. The overall moment for the film at 400 K was $9.5\times10^{-5} \pm 5.7\times10^{-8}$ emu for the parallel configuration and $5.7\times10^{-5} \pm 9.6\times10^{-9}$ emu for the transverse configuration as compared to $1.3\times10^{-5} \pm 1.2\times10^{-8}$ emu for the perpendicular configuration. Furthermore, the moment for the FC measurement at 5 K was $1.1\times10^{-4} \pm 5.8\times10^{-8}$ emu for the parallel configuration and $6.6\times10^{-5} \pm 1.0\times10^{-8}$ emu for the transverse configuration as compared to $1.3\times10^{-5} \pm 1.6\times10^{-8}$ emu for the perpendicular configuration. One important factor behind this behaviour of magnetization is the demagnetization field which was the highest in the perpendicular configuration and the lowest in the parallel configuration. Furthermore, in the perpendicular configuration, due to single-domain-size thickness of magnetic material along the field, surface effects were prominent which resulted in a lower magnetization. In the parallel field configuration, application of the field along the

Table 5-1: Magnetization at 400 K (DC Susceptibility)

Field configuration	Magnetization (emu)
Parallel	$9.5\times10^{-5} \pm 5.7\times10^{-8}$
Transverse	$5.7\times10^{-5} \pm 9.6\times10^{-9}$
Perpendicular	$1.3\times10^{-5} \pm 1.2\times10^{-8}$

Table 5-2: Magnetization at 5 K (FC-DC Susceptibility)

Field configuration	Magnetization (emu)
Parallel	$1.1\times10^{-4} \pm 5.8\times10^{-8}$
Transverse	$6.6\times10^{-5} \pm 1.0\times10^{-8}$
Perpendicular	$1.3\times10^{-5} \pm 1.6\times10^{-8}$

Table 5-3: Maximum Magnetization (DC Susceptibility)

Field configuration	FC Magnetization (emu)	ZFC Magnetization (emu)
Parallel	$4.5\times10^{-5} \pm 1.2\times10^{-8}$	$1.8\times10^{-5} \pm 5.6\times10^{-9}$
Transverse	$2.0\times10^{-5} \pm 7.6\times10^{-9}$	$4.4\times10^{-5} \pm 4.2\times10^{-9}$

length of the stripes (easy-axis) resulted in the highest overall magnetization as compared to other two field configurations. The reason for the lower magnetization in the stripes in the transverse configuration ($2.0\times10^{-5} \pm 7.6\times10^{-9}$ emu and $1.8\times10^{-5} \pm 5.6\times10^{-9}$ emu being the maximum for the FC and the ZFC measurement respectively) as compared to the stripes in the parallel configuration ($4.5\times10^{-5} \pm 1.2\times10^{-8}$ emu and $4.4\times10^{-5} \pm$

4.2×10^{-9} emu being the maximum for the FC and the ZFC measurement respectively) is that the stripes were perpendicular to the applied field and the magnetic material along the applied field was less than that in the case of the parallel configuration.

Consider the DC susceptibility measurement for the $Ni_{80}Fe_{20}$ and the $Ni_{80}Fe_{20}$/NiO near-pattern film. Since the overall moment at 400 K in both cases was comparable ($2.2\times10^{-4} \pm 1.4\times10^{-7}$ emu for the $Ni_{80}Fe_{20}$ and $2.2\times10^{-4} \pm 4.9\times10^{-8}$ emu for the $Ni_{80}Fe_{20}$/NiO near-pattern film), we can make a rough comparison between the two though we are not sure about the amount of $Ni_{80}Fe_{20}$ being the same in both cases. The maximum overall moment, however, in the case of the ZFC measurement for the $Ni_{80}Fe_{20}$/NiO near-pattern film ($2.50\times10^{-4} \pm 1.99\times10^{-8}$ emu) was smaller than that for the $Ni_{80}Fe_{20}$ near-pattern film ($2.55\times10^{-4} \pm 1.87\times10^{-7}$ emu) which may be because of the exchange interaction between the $Ni_{80}Fe_{20}$ and the NiO layer. Unlike the $Ni_{80}Fe_{20}$ near-pattern film, merging of the ZFC and the FC data in the case of the $Ni_{80}Fe_{20}$/NiO near-pattern film was not sharp for the same reason. The maximum in-phase AC susceptibility at the measuring frequency of 10 Hz was $2.4\times10^{-6} \pm 1.4\times10^{-8}$ emu/Oe for $Ni_{80}Fe_{20}$/NiO near-pattern film as compared to $1.9\times10^{-4} \pm 1.8\times10^{-7}$ emu/Oe for the $Ni_{80}Fe_{20}$ near-pattern film. The out-of-phase susceptibility showed no change until ~350 K as the thermal energy was not able to overcome the exchange coupling between the $Ni_{80}Fe_{20}$ and the NiO layers.

An interesting comparison between the $Ni_{80}Fe_{20}$ and $Ni_{80}Fe_{20}$/NiO nano-stripes is on the basis of the superparamagnetic blocking temperature (T_B). T_B for $Ni_{80}Fe_{20}$ near-pattern film was 50 K, while for the $Ni_{80}Fe_{20}$ nano-stripes in the parallel and the transverse field configuration it was ~270 K and 50 K, respectively. For $Ni_{80}Fe_{20}$ nano-

stripes in the perpendicular field configuration the magnetization remained blocked in the temperature range of the experiment, i.e. T_B was higher than 400 K. In the case of the $Ni_{80}Fe_{20}$/NiO nano-stripes, this change in magnetization from blocked to superparamagnetic was not observed in any configuration. The exchange coupling between $Ni_{80}Fe_{20}$ and NiO layers resulted in blocking of the magnetization and T_B was above the maximum temperature for the measurement. So the NiO layer resulted in an enhanced T_B.

On the basis of T_B from the AC and the DC susceptibility measurements, the hysteresis loops were optimized to extract the maximum information of the magnetic field range near the coercivity. A comparison of the hysteresis loop of the nano-stripes in parallel and transverse configurations and the near-pattern film will be helpful to understand the shape of the loops and hence the magnetization behaviour of the nano-stripes. Consider the hysteresis loops at 10 K (Fig. 5.4, 5.5). The first thing we observe from the hysteresis loops are enhanced coercivities in the case of the nano-stripes in the parallel configuration as compared to the nano-stripes in the transverse configuration and the near-pattern film. This increase is because of the magnetic coupling between the stripes and is in agreement with results in the literature [20-33]. As the nano-stripes in the parallel configuration were magnetized by the applied field, domains were formed along the easy axis, i.e. along the length of a stripe. Upon the reversal of the applied field, due to the coupling between the neighbouring stripes, the reversal of domains and their propagation along the stripe was blocked. Such a coupling did not exist in the case of near-pattern film [72]. In the case of the nano-stripes in the transverse configuration, the stripe width was too small to allow any domain motion along the direction of applied

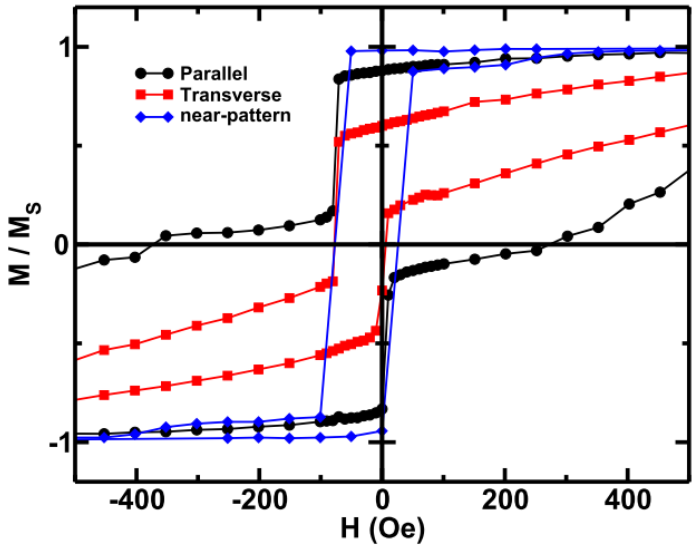

Figure 5.4: Hysteresis loops of the $Ni_{80}Fe_{20}$ near-pattern film and the nano-stripes in the parallel and the transverse field configuration at 10 K (error bars are smaller than the symbols)

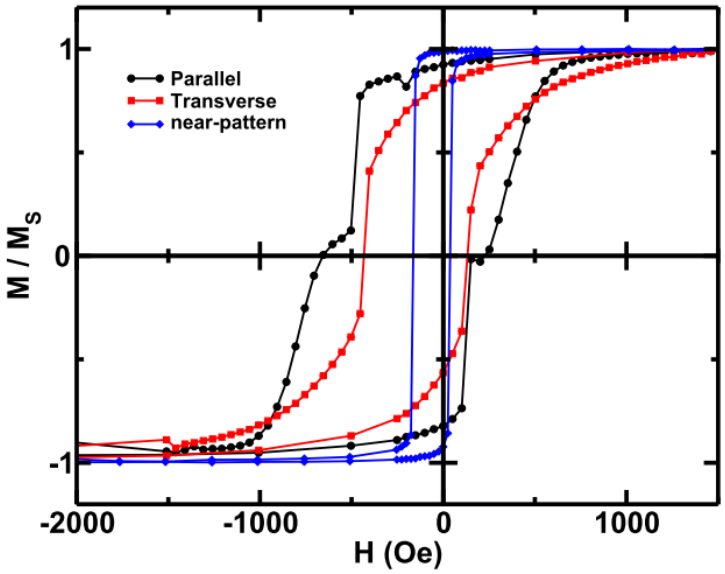

Figure 5.5: Hysteresis loops of the $Ni_{80}Fe_{20}$/NiO near-pattern film and the nano-stripes in the parallel and the transverse field configuration at 10 K (error bars are smaller than the symbols)

field. Hence the magnetization reversal process was dominated by the magnetization rotation of the domains [72]. The hysteresis loops showed the same behaviour at all temperatures until the coercivity reduced to zero.

From the hysteresis loops of the $Ni_{80}Fe_{20}$ nano-stripes and the near-pattern film (Fig. 3.8, 3.15, and 3.22) and the $Ni_{80}Fe_{20}$/NiO nano-stripes and the near-pattern film (Fig. 4.9, 4.17, and 4.25), we get some interesting information. For the nano-stripes in the parallel field configuration, magnetization reversal was not a one step process as we see in the case of the nano-stripes in the transverse and the perpendicular configuration and near-pattern film. This was because the film consisted of the stripes (along the field) and the surrounding unpatterned area (see Fig. 2.3 for a schematic of the patterned and unpatterned areas of the film). The magnetization behaviour of the unpatterned area was similar to that of the near-pattern film. However, this was not true for the stripes where the magnetic interaction between neighbouring stripes gave rise to the interesting phenomena like enhanced coercivity and increased exchange bias field as

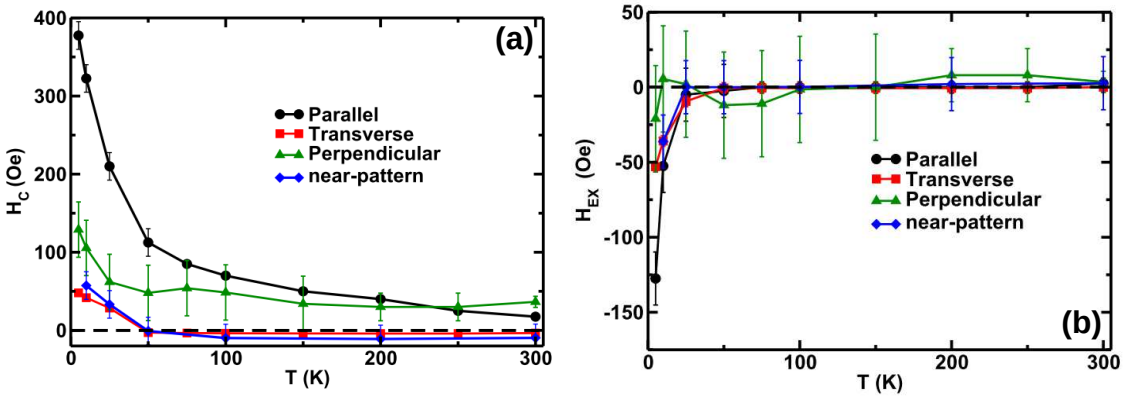

Figure 5.6: Temperature dependence of the (a) coercivity (H_C) and the (b) exchange bias field (H_{EX}) for the $Ni_{80}Fe_{20}$ nano-stripes and the near-pattern film (lines are a guide to the eye).

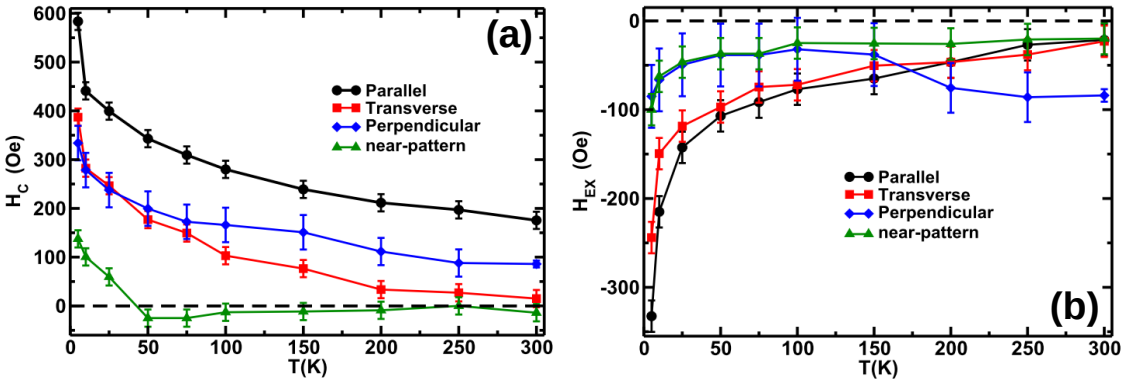

Figure 5.7: Temperature dependence of the (a) coercivity (H_C) and the (b) exchange bias field (H_{EX}) for the $Ni_{80}Fe_{20}$/NiO nano-stripes and the near-pattern film (lines are a guide to the eye)

compared to the near-pattern film (Fig. 5.6, and 5.7). Due to the exchange coupling between $Ni_{80}Fe_{20}$and NiO layers, the coercivity and exchange bias field for the $Ni_{80}Fe_{20}$/NiO nano-stripes were higher than that for $Ni_{80}Fe_{20}$ nano-stripes for respective configurations and temperatures. The same is true for the near-pattern film at respective temperatures.

The exchange coupling between the $Ni_{80}Fe_{20}$ and the NiO layers in the case of $Ni_{80}Fe_{20}$/NiO near-pattern film resulted in an enhanced coercivity as compared to the $Ni_{80}Fe_{20}$ near-pattern film i.e. 100 $\pm$ 18 Oe and 60 $\pm$ 18 Oe as compared to 57 $\pm$ 35 Oe and 33 $\pm$ 35 Oe at 10 K and 25 K respectively. The exchange coupling between the $Ni_{80}Fe_{20}$ and the NiO layer provided hindrance to the switching of the domain magnetization as the applied field switched its direction. The exchange coupling was also responsible, for the same reason, for enhanced exchange bias field as compared to the $Ni_{80}Fe_{20}$ near-pattern film i.e. -623 $\pm$ 18 Oe and -47 $\pm$ 18 Oe as compared to -36 $\pm$ 35 Oe and 0 $\pm$ 35 Oe at 10 K and 25 K respectively for the $Ni_{80}Fe_{20}$ near-pattern film. As

depicted by the T_B, the coercivity was not measurable at 50 K for both the $Ni_{80}Fe_{20}$ and the $Ni_{80}Fe_{20}$/NiO near-pattern film so the origin of the coercivity is believed to be the same, i.e. crystallite size distribution in the $Ni_{80}Fe_{20}$ layer. The exchange bias between the two layers in the $Ni_{80}Fe_{20}$/NiO near-pattern film played its role in enhancing the coercivity and the exchange bias field at the certain temperatures.

As far as the temperature dependence of the coercivity of $Ni_{80}Fe_{20}$ and $Ni_{80}Fe_{20}$/NiO nano-stripes in the parallel field configuration is concerned, the coercivity did not go to zero within the temperature range of measurement (10-400 K) in both samples. Since the nano-stripe width was 44 nm for $Ni_{80}Fe_{20}$ (Fig. 3.1) and 66 nm for $Ni_{80}Fe_{20}$/NiO (Fig. 4.1), the increased coercivity can not be attributed to the existence of a magnetic ripple structure in the stripe [72], which may be true for the wider stripes (with width of 1 μm or more) [14]. The reason for this increased coercivity as compared to the near-pattern film is that the nano-stripes were aligned along the applied field. A strong magnetic interaction seems to exist between the nano-stripes because the spacing between them was very small, i.e. ~25 nm for $Ni_{80}Fe_{20}$ (Fig. 3.1) and ~10 nm for $Ni_{80}Fe_{20}$/NiO. (Fig. 4.1) [75].

Figure 5.8 shows the hysteresis loops for the $Ni_{80}Fe_{20}$ near-pattern film and nano-stripes in the parallel configuration, where the near-pattern loop is superimposed for comparison. The magnetization reversal was a two step process. Within the range between the point 1 and the point 2 (in boxes), both hysteresis loops have the same coercivity within the range of experimental resolution. The same is true for the range between the point 4 and the point 5. This similarity between the two loops arises because of un-patterned area around the patterned area which behaves quite similar to the near-

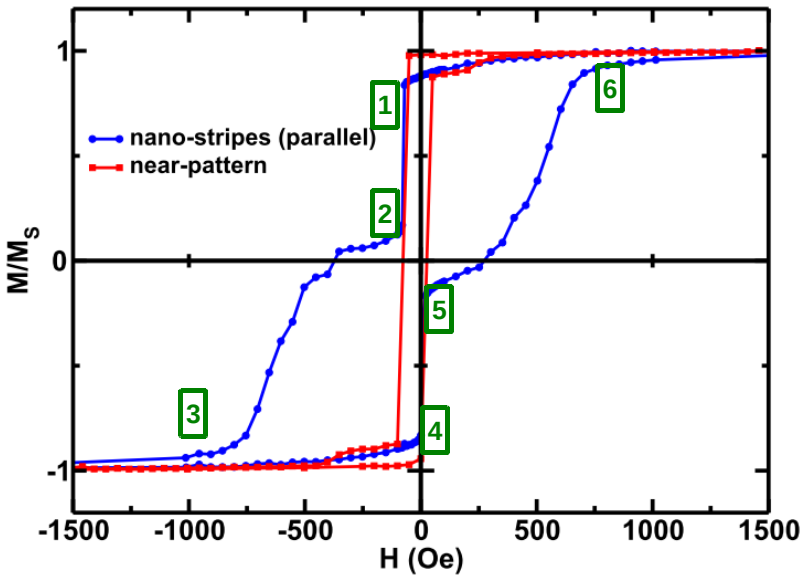

Figure 5.8: Comparison of hysteresis loops for the $Ni_{80}Fe_{20}$ near-pattern film and the nano-stripes in the parallel field configuration at 10 K over the applied field range ± 1500 Oe. (error bars are smaller than the symbols)

pattern film. The second step of the magnetization reversal stemmed from the switching events in the stripes [76]. Within the range between the point 2 and the point 3, a low magnetization in the applied field range +50 to –1000 Oe was observed. Since the neighbouring stripes were ~25 nm apart there should exist a strong interaction between the stripes. That is why, as the applied field direction reversed, the magnetization of the stripes did not follow the applied field immediately. Unlike the first magnetization reversal step, switching occurred over a wider field range because of the wide field distribution in Bloch line nucleation, which is necessary to initiate the switching [76]. Bloch line is an intermediate region in the domain wall which separates the section of different magnetization (sub-domains). The same explanation holds in the case of hysteresis loop shapes for the $Ni_{80}Fe_{20}$/NiO nano-stripes.

The hysteresis loops for the $Ni_{80}Fe_{20}$ nano-stripes in the parallel and the transverse field configurations (Fig. 5.9) showed that the saturation magnetization was almost the same because the amount of material to be magnetized remained unchanged as it was the same sample in two different field configurations. The same was true for the $Ni_{80}Fe_{20}$/NiO nano-stripes in the parallel and the transverse field configurations (Fig.

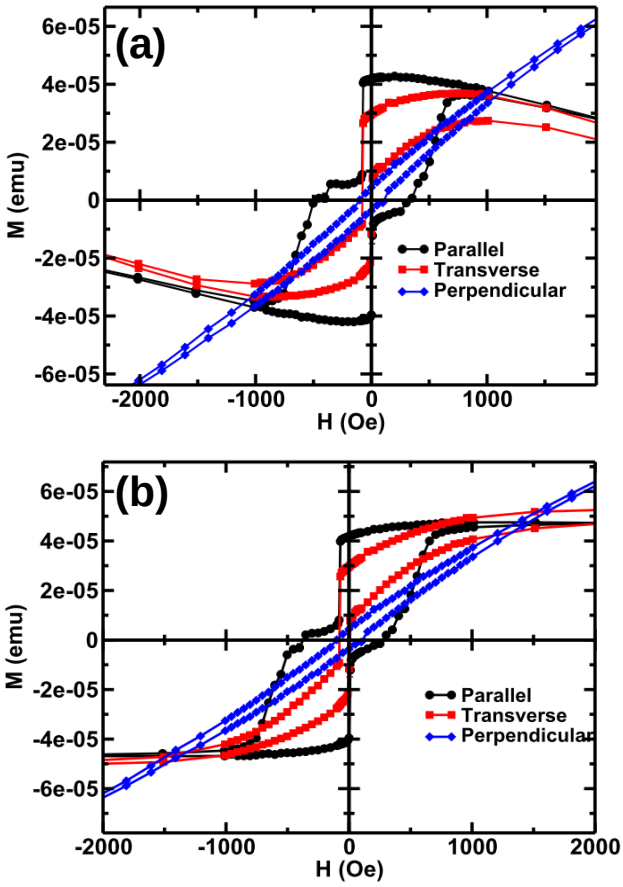

Figure 5.9: A comparison of the hysteresis loops for $Ni_{80}Fe_{20}$ nano-stripes at 10 K for the parallel, transverse and the perpendicular field configuration (a) before and (b) after subtracting the high field susceptibility over the applied field range $\pm$2000 Oe (error bars are smaller than the symbols)

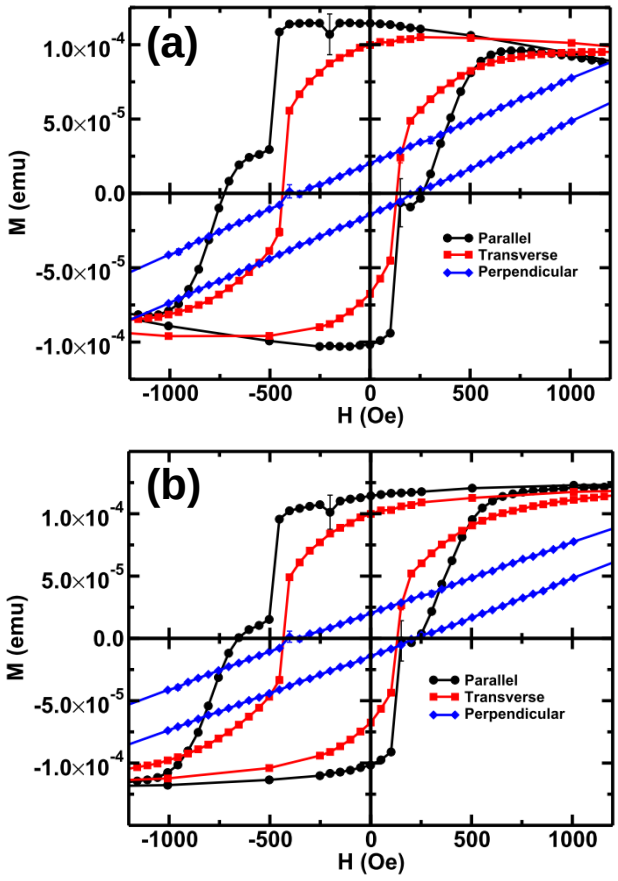

Figure 5.10: A comparison of the hysteresis loops at 10 K for the parallel, transverse and the perpendicular field configuration (a) before and (b) after subtracting the high field susceptibility over the applied field range ± 1500 Oe.

5.10). A low magnetization over the field range ±1000 Oe and low remanence magnetization in the transverse field configuration as compared to the parallel field configuration, for both samples, was because the stripes were not aligned along the applied magnetic field and hence the two-phase magnetization behaviour did not appear.

In the transverse field configuration, the demagnetization field was higher than that in the case of the parallel field configuration. Furthermore, the most important regions with respect to the magnetization behaviour in this field configuration were the

side regions of the stripes. The interaction between the side regions of the stripes offered resistance to the magnetization reversal though this coupling was not as strong as in the case of the parallel field configurations. Hence low remanence magnetization and asymmetric (along the magnetization axis) hysteresis loops were seen in the hysteresis loop for transverse field configuration. Due to the shape of the hysteresis loops, it was not possible to find the saturation magnetization in the case of the nano-stripes in the perpendicular configuration.

An interesting result was non-zero exchange bias field in $Ni_{80}Fe_{20}$ film. $Ni_{80}Fe_{20}$ is soft ferromagnetic material and is not supposed to show an exchange bias shift in the hysteresis loop. This non-zero exchange bias field appeared, most likely, because of the surface effect [34, 35]. At the surface, the low coordination number of the atoms results in a magnetization different than the bulk. However this non-zero exchange bias field appeared only at low temperatures (below 25 K) where thermal energy was smaller than the surface anisotropy energy.

Chapter Six: Conclusions

The $Ni_{80}Fe_{20}$ and the $Ni_{80}Fe_{20}$/NiO near-pattern films and the nano-stripes were characterized magnetically. The near-pattern films were characterized in the in-plane configuration only, and the nano-stripe films were characterized in the parallel, transverse and the perpendicular field configurations.

The existence of the nano-stripes and their orientation with respect to the applied field was found to have a profound effect on the magnetic properties. Depending on the orientation of the nano-stripes with respect to the applied field, differences in the superparamagnetic blocking temperature, coercivity, and exchange-bias field were observed mainly because of the difference in the demagnetization field.

The superparamagnetic blocking temperature T_B, in the case of $Ni_{80}Fe_{20}$, was the same (50 K) for the nano-stripes in the transverse configuration and the near-pattern film. However, T_B was considerably higher (270 K) for the nano-stripes in the parallel configuration because of the exchange interactions between the nano-stripes oriented with the applied field. This indicates a 5.4 times larger energy barrier to the magnetization reversal in the later case as compared to the former ones. This fact was

Table 6-1: Blocking Temperature (T_B)

	$Ni_{80}Fe_{20}$	**$Ni_{80}Fe_{20}$/NiO**
Near-Pattern	50 K	N/A
Parallel	270 K	N/A
Transverse	50 K	N/A
Perpendicular	N/A	N/A

supported by the highest coercivity and the highest exchange bias field in the case of the $Ni_{80}Fe_{20}$ nano-stripes in the parallel configuration as compared to the other configurations and the near-pattern film. However, in the case of the $Ni_{80}Fe_{20}$/NiO nano-stripes T_B was above the maximum temperature for the measurement.

In the case of the $Ni_{80}Fe_{20}$ near-pattern film, T_B = 50 K was obtained from the DC susceptibility data, AC susceptibility data and the temperature dependence of the coercivity. On the other hand, in the case of the $Ni_{80}Fe_{20}$ nano-stripes in the transverse configuration, both the coercivity and the AC susceptibility data showed T_B = 50 K which was not in agreement with the DC susceptibility data. In the case of the $Ni_{80}Fe_{20}$ nano-stripes in the parallel configuration, alignment of the nano-stripes along the applied magnetic field and the exchange coupling between the neighbouring nano-stripes made the difference of the nature (what is actually measured) of measurement techniques, i.e. DC susceptibility and AC susceptibility, more important. That is why, while the T_B was found to be the same for all three techniques in the case of the near-pattern film, it was different in the case of the nano-stripes which is in agreement with the literature [67].

As far as the coercivity and exchange bias field is concerned, without any exception, $Ni_{80}Fe_{20}$/NiO nano-stripes showed larger coercivity and exchange bias field as compared to the $Ni_{80}Fe_{20}$ nano-stripes in all applied field configurations (Fig. 6.1). This enhanced coercivity in case of $Ni_{80}Fe_{20}$/NiO nano-stripes appeared because of the exchange interaction between $Ni_{80}Fe_{20}$ and NiO layers as the exchange coupling between the $Ni_{80}Fe_{20}$ and NiO layer resisted the switching of the domain magnetization as the applied field switched its direction. Another important reason was the reduced distance between the $Ni_{80}Fe_{20}$/NiO stripes as compared to the $Ni_{80}Fe_{20}$ stripes. Because of the

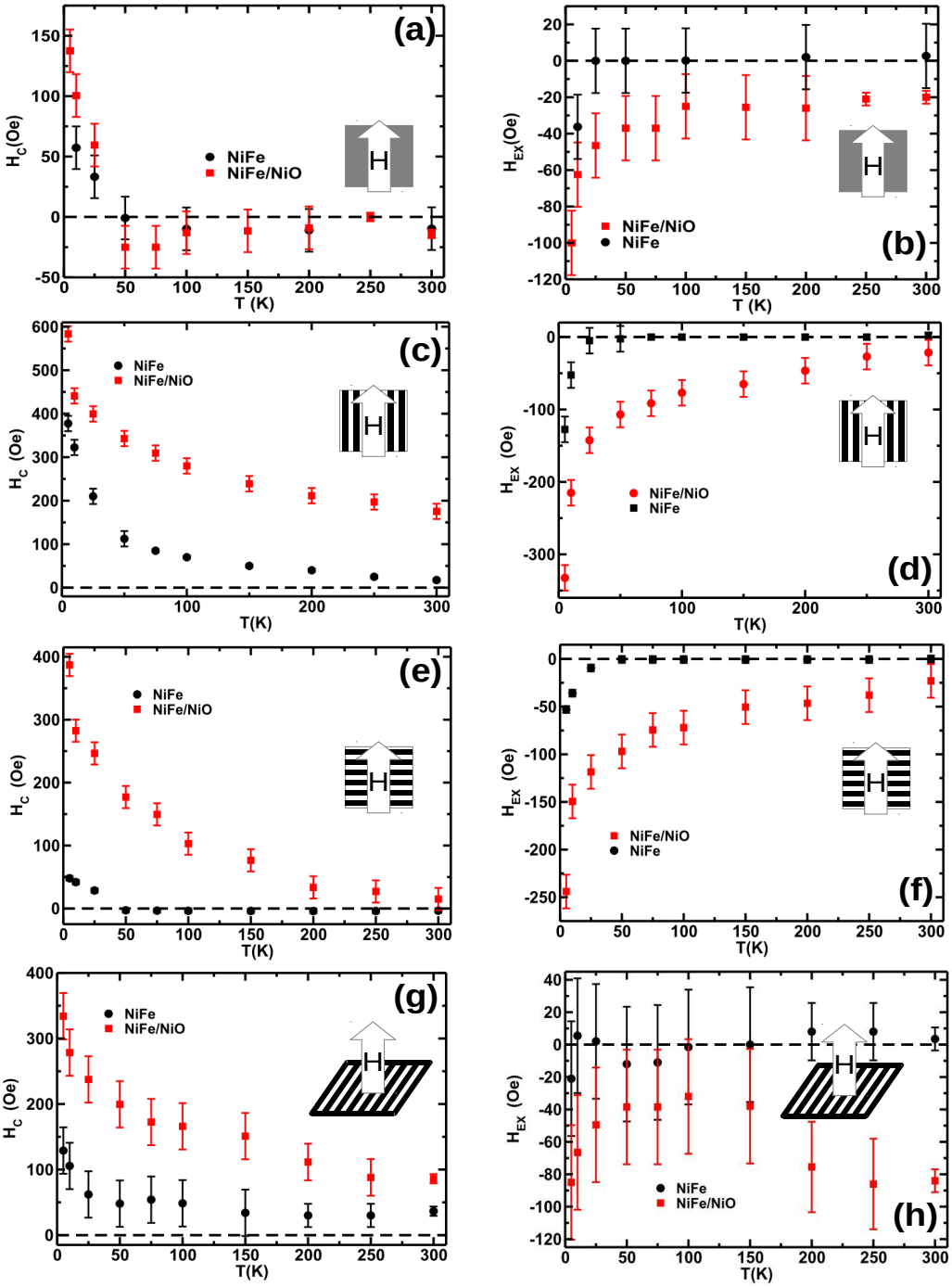

Figure 6.1: Coercivity (H_C) and exchange bias field (H_{EX}) for near-pattern films (a,b) and nano-stripes in parallel (c,d) transverse (e,f) and perpendicular (g,h) field configurations

increased thickness of the deposited material, the distance between the $Ni_{80}Fe_{20}$/NiO stripes was 10 nm, as compared to 25 nm for the $Ni_{80}Fe_{20}$ stripes. This reduced separation between the stripes resulted in a stronger magnetic coupling between them which, in turn, resulted in an increased coercivity. The same factors contributed to the enhanced exchange bias field for the same reasons.

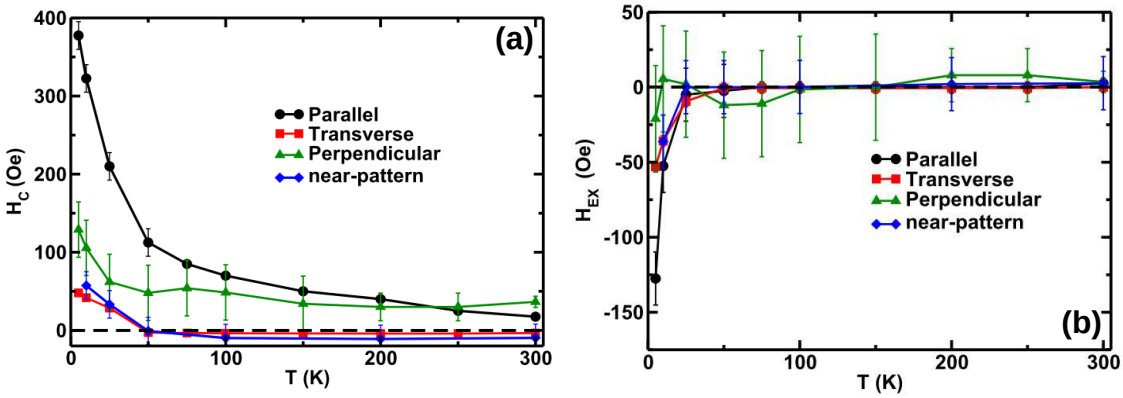

Figure 6.2: Temperature dependence of the (a) coercivity (H_C) and the (b) exchange bias field (H_{EX}) for the $Ni_{80}Fe_{20}$ nano-stripes and the near-pattern film. (lines are a guide to the eye)

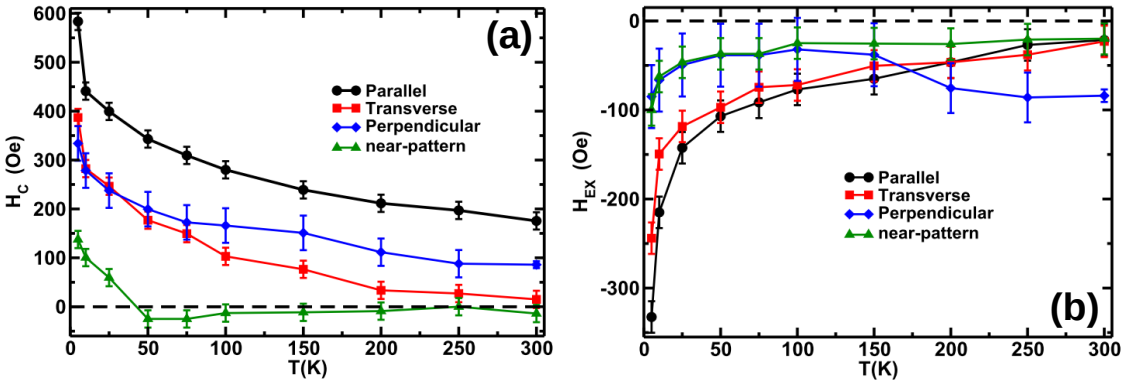

Figure 6.3: Temperature dependence of the (a) coercivity (H_C) and the (b) exchange bias field (H_{EX}) for the $Ni_{80}Fe_{20}$/NiO nano-stripes and the near-pattern film. (lines are a guide to the eye)

It was confirmed that the coercivity and the exchange bias field can be controlled, not only by using a patterned medium instead of a plane film, but also by the orientation of that pattern. The nano-stripes in the parallel configuration exhibited, overall, the largest coercivity and the exchange bias field among all three field configurations in the case of $Ni_{80}Fe_{20}$ (Table 6.2), as well as the $Ni_{80}Fe_{20}$/NiO (Table 6.3) nano-stripes.

As stated in the introductory chapter, a material with the minimum coercivity and the maximum exchange-bias field is of technological importance. Now we shall discuss the samples on the basis of this criterion.

The $Ni_{80}Fe_{20}$ near-pattern film showed a reasonably high T_B (50 K) and low coercivity but the very low exchange bias field places this sample at the bottom in the ranking. The $Ni_{80}Fe_{20}$ nano-stripes in the parallel configuration showed the highest T_B as well as the highest exchange bias field and the highest coercivity as well; however, the high coercivity is a drawback. The $Ni_{80}Fe_{20}$ nano-stripes in the transverse configuration showed impressive results with low coercivity and high exchange bias field, but a low T_B makes this configuration less useful for the high temperature applications. The $Ni_{80}Fe_{20}$ nano-stripes in the perpendicular configuration, due to the high demagnetization field, did not show any good results from the application point of view. Though it was not possible to pick a single configuration as the best, the nano-stripes in the transverse configuration are a good choice for applications where the temperature is lower than 50 K, while the nano-stripes in the parallel configuration are recommended for high magnetic field applications because of the high coercivity (Fig. 6.3a).

Table 6-2: The coercivity (HC) and the exchange bias field (HEX) for the Ni80Fe20 samples at 10 K

	H_C(Oe)	H_{EX}(Oe)
Near-pattern	57±189	-36±18
Parallel	323±18	-53±18
Transverse	42±4	-36±4
Perpendicular	106±35	5.5±35

Table 6-3: The coercivity (H_C) and the exchange bias field (H_{EX}) for the $Ni_{80}Fe_{20}$/NiO samples at 10 K

	H_C (Oe)	H_{EX}(Oe)
Near-pattern	101±18	-63±18
Parallel	441±18	-215±18
Transverse	283±18	-150±18
Perpendicular	279±35	-67±35

In the case of the $Ni_{80}Fe_{20}$/NiO near-pattern film and the nano-stripes, T_B was always higher than the maximum temperature of the measurement. Although the nano-stripes in the parallel configuration showed the maximum exchange bias field, coercivity was also the highest in this case. The nano-stripes in the transverse configuration came out to be the best with a reasonably high exchange bias field and low coercivity.

Magnetization per unit volume was 494±109 emu/cm^3 for $Ni_{80}Fe_{20}$ near-pattern film, as compared to 800 emu/cm^3 for a bulk specimen [10]. This indicates the effect of

reduced dimensions and a surface effect. Magnetization for the $Ni_{80}Fe_{20}$ nano-stripes in the parallel configuration was 302±118 emu/cm^3 which may be because of the increased surface contribution as a result of pattern. Demagnetization field resulted in even lower magnetization in the $Ni_{80}Fe_{20}$ nano-stripes in the transverse (296±116 emu/cm^3) field configuration. The magnetization per unit volume for the $Ni_{80}Fe_{20}$/NiO near-pattern film (313±66 emu/cm^3) was lower than that for the $Ni_{80}Fe_{20}$ near-pattern film. The reason for this reduced magnetization was that, in addition to the factors described in the case of the $Ni_{80}Fe_{20}$ near-pattern film, the pinning of the $Ni_{80}Fe_{20}$ crystallites by the NiO layer was another important factor. Magnetization per unit volume was essentially the same for the $Ni_{80}Fe_{20}$/NiO nano-stripes in the parallel (119±27 emu/cm^3) and the transverse (116±27 emu/cm^3) configuration. Both these values were smaller than that for the near-pattern film for the same reasons described in the case of the $Ni_{80}Fe_{20}$ samples. These values are smaller that those for respective $Ni_{80}Fe_{20}$ nano-stripes configurations as well because of the possible pinning of the $Ni_{80}Fe_{20}$ domains at the $Ni_{80}Fe_{20}$-NiO interface.

Future Work

- Detailed analysis of the data with an applicable model (e.g. Landau-Lifshitz-Gilbert model) will provide a deeper insight in the magnetism of the samples.
- Neutron reflectometery can provide more information about the atomic and magnetic structure of the samples.

Appendix A: MultiVu Script for the AC Susceptibility

```
1:  ----- Xac
2:  Magnet Reset
3:  Set Temperature 400.000K at 10.000K/min.
4:  Waitfor Temp:Stable Delay:0secs
5:  Set Temperature 100.000K at 10.000K/min.
6:  Waitfor Temp:Stable Delay:0secs
7:  Set Temperature 30.000K at 10.000K/min.
8:  Waitfor Temp:Stable Delay:0secs
9:  Set Temperature 10.000K at 5.000K/min.
10:  Waitfor Temp:Stable Delay:120secs
11:  Set Temperature 5.000K at 2.000K/min.
12:  Waitfor Temp:Stable Delay:0secs
13:  Scan AC Frequency from 9.99893 Hz to 1000.00 Hz in 3 steps
(495.001 Hz/step)
14:     Measure AC: 2.5000 Oe, 250.000 Hz, 3 meas, 2 blks, 0.0001
Null, x 1, 0 s, AutoRng, track:Yes, diag:No, raw:No
15:  End Scan
16:  Scan Temp from 10.00K to 400.0K at 2.500K/min in 10K
increments (40 steps) Settle
17:     Scan AC Frequency from 9.99893 Hz to 1000.00 Hz in 3
steps (495.001 Hz/step)
18:         Measure AC: 2.5000 Oe, 250.000 Hz, 3 meas, 2 blks,
0.0001 Null, x 1, 0 s, AutoRng, track:Yes, diag:No, raw:No
19:     End Scan
```

```
20:  End Scan
21:  ----- shutdown
22:  Set Temperature 30.000K at 10.000K/min.
23:  Waitfor Temp:Stable Delay:0secs
24:  Set Driver 1 Output Power to 0.000
25:  Set Driver 2 Output Power to 0.000
```

Appendix B: MultiVu Script for the DC Susceptibility

```
1:  ----- M vs T  ZFC and FC 100 Oe-----
2:  Set Temperature 400.000K at 10.000K/min.
3:  Waitfor Temp:Stable Delay:0secs
4:  Set Temperature 100.000K at 10.000K/min.
5:  Waitfor Temp:Stable Delay:0secs
6:  Set Temperature 30.000K at 10.000K/min.
7:  Waitfor Temp:Stable Delay:0secs
8:  Set Temperature 10.000K at 10.000K/min.
9:  Waitfor Temp:Stable Delay:120secs
10:  Set Temperature 5.000K at 2.000K/min.
11:  Waitfor Temp:Stable Delay:0secs
12:  Set Magnetic Field 100.00 Oe, No Overshoot, Hi Res Enabled
13:  Waitfor Field:Stable Delay:0secs
14:  Set Temperature 5.000K at 2.000K/min.
15:  Waitfor Temp:Stable Delay:0secs
16:  Measure RSO: 5.00 cm, 5 cyc, 3 meas, 1.0 Hz, Center,
AutoRng, Long, Iterative Reg., track:Yes, raw:No, diag:No
17:  Scan Temp from 10.00K to 400.0K at 5.000K/min in 10K
increments (40 steps) Settle
18:     Measure RSO: 5.00 cm, 5 cyc, 3 meas, 1.0 Hz, Center,
AutoRng, Long, Iterative Reg., track:Yes, raw:No, diag:No
19:  End Scan
20:  Scan Temp from 390.0K to 10.00K at 5.000K/min in -10K
increments (39 steps) Settle
```

21: Measure RSO: 5.00 cm, 5 cyc, 3 meas, 1.0 Hz, Center, AutoRng, Long, Iterative Reg., track:Yes, raw:No, diag:No

22: End Scan

23: Set Temperature 5.000K at 2.000K/min.

24: Waitfor Temp:Stable Delay:0secs

25: Measure RSO: 5.00 cm, 5 cyc, 3 meas, 1.0 Hz, Center, AutoRng, Long, Iterative Reg., track:Yes, raw:No, diag:No

26: Set Magnetic Field 0.00 Oe, No Overshoot, Hi Res Enabled

27: Waitfor Field:Stable Delay:0secs

Appendix C: MultiVu Script for the Hysteresis Loops

```
28:  -----  MvsH FC 400 K 20 kOe
29:  Set Temperature 400.000K at 10.000K/min.
30:  Waitfor Temp:Stable Delay:0secs
31:  Set Magnetic Field 20000.00 Oe, No Overshoot, Hi Res Enabled
32:  Waitfor Field:Stable Delay:0secs
33:  Set Temperature 100.000K at 10.000K/min.
34:  Waitfor Temp:Stable Delay:0secs
35:  Set Temperature 30.000K at 10.000K/min.
36:  Waitfor Temp:Stable Delay:0secs
37:  Set Temperature 10.000K at 5.000K/min.
38:  Waitfor Temp:Stable Delay:0secs
39:  -----  MvsH 5 K
40:  Set Temperature 5.000K at 2.000K/min.
41:  Waitfor Temp:Stable Delay:0secs
42:  Scan Field from 20000.00Oe to 10000.00 Oe in -2500.00 Oe
increments (5 steps), Hysteresis Mode, Hi Res Disabled
43:     Measure RSO: 5.00 cm, 5 cyc, 3 meas, 1.0 Hz, Center,
AutoRng, Long, Iterative Reg., track:Yes, raw:No, diag:No
44:  End Scan
45:  Scan Field from 9000.00Oe to 3000.00 Oe in -1000.00 Oe
increments (7 steps), Hysteresis Mode, Hi Res Disabled
46:     Measure RSO: 5.00 cm, 5 cyc, 3 meas, 1.0 Hz, Center,
AutoRng, Long, Iterative Reg., track:Yes, raw:No, diag:No
47:  End Scan
```

48: Scan Field from 2500.00Oe to -500.00 Oe in -250.00 Oe increments (13 steps), Hysteresis Mode, Hi Res Disabled

49: Measure RSO: 5.00 cm, 5 cyc, 3 meas, 1.0 Hz, Center, AutoRng, Long, Iterative Reg., track:Yes, raw:No, diag:No

50: End Scan

51: Scan Field from -550.00Oe to -950.00 Oe in -50.00 Oe increments (9 steps), Hysteresis Mode, Hi Res Enabled

52: Measure RSO: 5.00 cm, 5 cyc, 3 meas, 1.0 Hz, Center, AutoRng, Long, Iterative Reg., track:Yes, raw:No, diag:No

53: End Scan

54: Scan Field from -1000.00Oe to -2500.00 Oe in -250.00 Oe increments (7 steps), Hysteresis Mode, Hi Res Disabled

55: Measure RSO: 5.00 cm, 5 cyc, 3 meas, 1.0 Hz, Center, AutoRng, Long, Iterative Reg., track:Yes, raw:No, diag:No

56: End Scan

57: Scan Field from -3000.00Oe to -9000.00 Oe in -1000.00 Oe increments (7 steps), Hysteresis Mode, Hi Res Disabled

58: Measure RSO: 5.00 cm, 5 cyc, 3 meas, 1.0 Hz, Center, AutoRng, Long, Iterative Reg., track:Yes, raw:No, diag:No

59: End Scan

60: Scan Field from -10000.00Oe to -20000.00 Oe in -2500.00 Oe increments (5 steps), Hysteresis Mode, Hi Res Disabled

61: Measure RSO: 5.00 cm, 5 cyc, 3 meas, 1.0 Hz, Center, AutoRng, Long, Iterative Reg., track:Yes, raw:No, diag:No

62: End Scan

63: Scan Field from -17500.00Oe to -10000.00 Oe in 2500.00 Oe increments (4 steps), Hysteresis Mode, Hi Res Disabled

64: Measure RSO: 5.00 cm, 5 cyc, 3 meas, 1.0 Hz, Center, AutoRng, Long, Iterative Reg., track:Yes, raw:No, diag:No

65: End Scan

66: Scan Field from -9000.00Oe to -3000.00 Oe in 1000.00 Oe increments (7 steps), Hysteresis Mode, Hi Res Disabled

67: Measure RSO: 5.00 cm, 5 cyc, 3 meas, 1.0 Hz, Center, AutoRng, Long, Iterative Reg., track:Yes, raw:No, diag:No

68: End Scan

69: Scan Field from -2500.00Oe to -250.00 Oe in 250.00 Oe increments (10 steps), Hysteresis Mode, Hi Res Disabled

70: Measure RSO: 5.00 cm, 5 cyc, 3 meas, 1.0 Hz, Center, AutoRng, Long, Iterative Reg., track:Yes, raw:No, diag:No

71: End Scan

72: Scan Field from -200.00Oe to 200.00 Oe in 50.00 Oe increments (9 steps), Hysteresis Mode, Hi Res Enabled

73: Measure RSO: 5.00 cm, 5 cyc, 3 meas, 1.0 Hz, Center, AutoRng, Long, Iterative Reg., track:Yes, raw:No, diag:No

74: End Scan

75: Scan Field from 250.00Oe to 2500.00 Oe in 250.00 Oe increments (10 steps), Hysteresis Mode, Hi Res Disabled

76: Measure RSO: 5.00 cm, 5 cyc, 3 meas, 1.0 Hz, Center, AutoRng, Long, Iterative Reg., track:Yes, raw:No, diag:No

77: End Scan

78: Scan Field from 3000.00Oe to 9000.00 Oe in 1000.00 Oe increments (7 steps), Hysteresis Mode, Hi Res Disabled

79: Measure RSO: 5.00 cm, 5 cyc, 3 meas, 1.0 Hz, Center, AutoRng, Long, Iterative Reg., track:Yes, raw:No, diag:No

80: End Scan

81: Scan Field from 10000.00Oe to 20000.00 Oe in 2500.00 Oe increments (5 steps), Hysteresis Mode, Hi Res Disabled

82: Measure RSO: 5.00 cm, 5 cyc, 3 meas, 1.0 Hz, Center, AutoRng, Long, Iterative Reg., track:Yes, raw:No, diag:No

83: End Scan

84: Set Magnetic Field 0.00 Oe, No Overshoot, Hi Res Enabled

85: Waitfor Field:Stable Delay:0secs

86: ----- MvsH 10 K

87: Set Temperature 10.000K at 2.000K/min.

88: Waitfor Temp:Stable Delay:0secs

89: Scan Field from 20000.00Oe to 10000.00 Oe in -2500.00 Oe increments (5 steps), Hysteresis Mode, Hi Res Disabled

90: Measure RSO: 5.00 cm, 5 cyc, 3 meas, 1.0 Hz, Center, AutoRng, Long, Iterative Reg., track:Yes, raw:No, diag:No

91: End Scan

92: Scan Field from 9000.00Oe to 3000.00 Oe in -1000.00 Oe increments (7 steps), Hysteresis Mode, Hi Res Disabled

93: Measure RSO: 5.00 cm, 5 cyc, 3 meas, 1.0 Hz, Center, AutoRng, Long, Iterative Reg., track:Yes, raw:No, diag:No

94: End Scan

95: Scan Field from 2500.00Oe to -500.00 Oe in -250.00 Oe increments (13 steps), Hysteresis Mode, Hi Res Disabled

96: Measure RSO: 5.00 cm, 5 cyc, 3 meas, 1.0 Hz, Center, AutoRng, Long, Iterative Reg., track:Yes, raw:No, diag:No

97: End Scan

98: Scan Field from -550.00Oe to -950.00 Oe in -50.00 Oe increments (9 steps), Hysteresis Mode, Hi Res Enabled

99: Measure RSO: 5.00 cm, 5 cyc, 3 meas, 1.0 Hz, Center, AutoRng, Long, Iterative Reg., track:Yes, raw:No, diag:No

100: End Scan

101: Scan Field from -1000.00Oe to -2500.00 Oe in -250.00 Oe increments (7 steps), Hysteresis Mode, Hi Res Disabled

102: Measure RSO: 5.00 cm, 5 cyc, 3 meas, 1.0 Hz, Center, AutoRng, Long, Iterative Reg., track:Yes, raw:No, diag:No

103: End Scan

104: Scan Field from -3000.00Oe to -9000.00 Oe in -1000.00 Oe increments (7 steps), Hysteresis Mode, Hi Res Disabled

105: Measure RSO: 5.00 cm, 5 cyc, 3 meas, 1.0 Hz, Center, AutoRng, Long, Iterative Reg., track:Yes, raw:No, diag:No

106: End Scan

107: Scan Field from -10000.00Oe to -20000.00 Oe in -2500.00 Oe increments (5 steps), Hysteresis Mode, Hi Res Disabled

108: Measure RSO: 5.00 cm, 5 cyc, 3 meas, 1.0 Hz, Center, AutoRng, Long, Iterative Reg., track:Yes, raw:No, diag:No

109: End Scan

110: Scan Field from -17500.00Oe to -10000.00 Oe in 2500.00 Oe increments (4 steps), Hysteresis Mode, Hi Res Disabled

111: Measure RSO: 5.00 cm, 5 cyc, 3 meas, 1.0 Hz, Center, AutoRng, Long, Iterative Reg., track:Yes, raw:No, diag:No

112: End Scan

113: Scan Field from -9000.00Oe to -3000.00 Oe in 1000.00 Oe increments (7 steps), Hysteresis Mode, Hi Res Disabled

114: Measure RSO: 5.00 cm, 5 cyc, 3 meas, 1.0 Hz, Center, AutoRng, Long, Iterative Reg., track:Yes, raw:No, diag:No

115: End Scan

116: Scan Field from -2500.00Oe to -250.00 Oe in 250.00 Oe increments (10 steps), Hysteresis Mode, Hi Res Disabled

117: Measure RSO: 5.00 cm, 5 cyc, 3 meas, 1.0 Hz, Center, AutoRng, Long, Iterative Reg., track:Yes, raw:No, diag:No

118: End Scan

119: Scan Field from -200.00Oe to 200.00 Oe in 50.00 Oe increments (9 steps), Hysteresis Mode, Hi Res Enabled

120: Measure RSO: 5.00 cm, 5 cyc, 3 meas, 1.0 Hz, Center, AutoRng, Long, Iterative Reg., track:Yes, raw:No, diag:No

121: End Scan

122: Scan Field from 250.00Oe to 2500.00 Oe in 250.00 Oe increments (10 steps), Hysteresis Mode, Hi Res Disabled

123: Measure RSO: 5.00 cm, 5 cyc, 3 meas, 1.0 Hz, Center, AutoRng, Long, Iterative Reg., track:Yes, raw:No, diag:No

124: End Scan

```
125:  Scan Field from 3000.00Oe to 9000.00 Oe in 1000.00 Oe
increments (7 steps), Hysteresis Mode, Hi Res Disabled
126:     Measure RSO: 5.00 cm, 5 cyc, 3 meas, 1.0 Hz, Center,
AutoRng, Long, Iterative Reg., track:Yes, raw:No, diag:No
127:  End Scan
128:  Scan Field from 10000.00Oe to 20000.00 Oe in 2500.00 Oe
increments (5 steps), Hysteresis Mode, Hi Res Disabled
129:     Measure RSO: 5.00 cm, 5 cyc, 3 meas, 1.0 Hz, Center,
AutoRng, Long, Iterative Reg., track:Yes, raw:No, diag:No
130:  End Scan
131:  Set Magnetic Field 0.00 Oe, No Overshoot, Hi Res Enabled
132:  Waitfor Field:Stable Delay:0secs

[code for higher temperatures omitted]

556:  ----- shutdown
557:  Set Temperature 30.000K at 10.000K/min.
558:  Waitfor Temp:Stable Delay:0secs
559:  Set Driver 1 Output Power to 0.000
560:  Set Driver 2 Output Power to 0.000
```

References

[1]. A. P. Guimarães, “Principles of Nanomagnetism” Springer-Verlag Berlin Geidelberg (2009)

[2]. J. Stöhr, H. C. Siegmann, “Magnetism from Fundamentals to Nanoscale Dynamics”, Springer-Verlag, Berlin Heidelberg (2006)

[3]. R. Tilley, “Understanding Solids”, John Wiley & Sons, USA (2004)

[4]. M. Volmer, M. Avram, Rev. Adv. Mater. Sci., **15,** 220 (2007)

[5]. S. Chikazumi. “Physics of Ferromagnetism”, Oxford University Press, New York (1997)

[6]. A. E. Berkowitz, K. Takano, J. Magn. Magn. Mater. **200** 552 (1999)

[7]. A. Hubert, R. Schafer, “Magnetic Domains: The analysis of magnetic microstructures”, Springer-Verlag, Berlin Heidelberg (1998)

[8]. B. D. Cullity, C. D. Graham, “Introduction to Magnetic Materials”, Wiley, USA (2009). Copyright © 2009 by the Institute of Electrical and Electronics Engineers, Inc.

[9]. M. Getzlaff, “Fundamentals of Magnetism”, Springer-Verlag, Berlin Heidelberg (2008)

[10]. R. C. O’Handley, “Modern Magnetic Materials: Principles and Application”, John Wiley & Sons, USA (2000)

[11]. M. McElfresh, “Fundamentals of Magnetism and Magnetic Measurements”, Quantum Design, USA (1994)

[12]. K. H. J. Buschow, F. R. De Boer, “Physics of Magnetism and Magnetic Materials”, Kluwer Academic Publishers, New York (2004)

[13]. H. Kronmüller, S. Parkin, “Handbook of Magnetism and Advanced Magnetic Materials: Vol. 4”, Wiley (2007)

[14]. C. A. F. Vaz, J. A. C. Bland, G. Lauhoff, Rep. Prog. Phys. **71** 056501 (2008)

[15]. J. McCord, L. Shultz, J. Fassbender, Adv. Mater. **20** 2090 (2008)

[16]. J. Fassbender, T. Strache, M. O. Liedke, D. Markó, S. Wintz, K. Lenz, A. Keller, S. Facsko, I. Mönch, J. McCord, New J. Phys. **11** 125002 (2009)

[17]. A. O. Adeyeye, M. K. Husain, V. Ng, J. Magn. Magn. Mater. **248** 355 (2002)

[18]. S. Goolaup, A. O. Adeyeye, N. Singh, G. Gubbiotti, J. Appl. Phys. **103** 07D528 (2008)

[19]. K. Theis-Bröhl, M. Wolff, A. Westphalen, H. Zabel, Phys. Rev. B **73** 174408 (2006)

[20]. M. H. Kryder, K. Y. Ahn, N. J. Mazzeo, S. Schwarzl and S. M. Kane, IEEE Trans. Magn. **16** 99 (1980)

[21]. S. Goolaup, N. Singh, A. Adeyeye, V. Ng and M. B. A. Jalil, IEEE Trans. Nanotech. **1** 471 (2004)

[22]. M. Vélez, R. Morales, J. M. Alameda, J. I. Martín, J. L. Vicent, F. Briones, J. Appl. Phys. **87** 5654 (2000)

[23]. A. Maeda, M. Kume, T. Ogura, K. Kuroki, T. Yamada,M. Nishikawa, Y. Harada, J. Appl. Phys. **76** 6667 (1994)

[24]. C. Shearwood, S.J. Blundell, M.J. Baird, J.A.C. Bland, M. Gester, H. Ahmed, H.P. Hughes, J. Appl. Phys. **75** 5249 (1994)

[25]. A. O. Adeyeye, J.A.C. Bland, C. Daboo, J. Lee, U. Ebels, H. Ahmed, J. Appl. Phys. **79** 6120 (1996)

[26]. S. P. Li, A. Lebib, D. Peyrade, M. Natali, Y. Chen, Appl. Phys. Lett. **77** 2743 (2000)

[27]. M. Kume, A. Maeda, T. Tanuma, K. Kuroki, J. Appl. Phys. **79** 6402 (1996)

[28]. A. Maeda, T. Tanuma, M. Kume, Mater. Sci. Eng. A **217–218** 203 (1996)

[29]. S.J. Blundell, C. Shearwood, M. Gester, M.J. Baird, J.A.C. Bland, H. Ahmed, J. Magn. Magn. Mater. **135** L17 (1994)

[30]. A.O. Adeyeye, G. Lauhoff, J.A.C. Bland, C. Daboo, D.G. Hasko, H. Ahmed, Appl. Phys. Lett. **70** 1046 (1997)

[31]. A.O. Adeyeye, J.A.C. Bland, C. Daboo, D.G. Hasko, H. Ahmed, J. Appl. Phys. **82** 469 (1997)

[32]. J.I. Martín, J.L. Costa-Krämer, F. Briones, J.L. Vicent, J. Magn. Magn. Mater. **221** 215 (2000)

[33]. Y. Nozaki, T. Ono, K. Motohashi, H. Miyajima, T. Kinoshita, J. Magn. Magn. Mater. **177–181** 1271 (1998)

[34]. G. C. Bailey, C. Vittoria, Phys. Rev. B **8**, 3247 (1973)

[35]. P. Weinberger, L. Szunyogh, C. Blass, C. Sommers, P. Entel, Phys. Rev. B **63**, 094417 (2001)

[36]. W. H. Meiklejohn, C. P. Bean, Phys. Rev. **105** 904 (1957)

[37]. J. Nogues, I. K. Schuller, J. Magn. Magn. Matr. **192**, 203 (1999)

[38]. A. E. Berkowitz, K. Takano, J. Magn. Magn. Matr. **200** 552 (1999)

[39]. T. Zhao, F. K. Zhang, T. Kai, Phys. Rev. B **65** 014431 (2001)

[40]. W. H. Meiklejohn, C. P. Bean, Phys. Rev. **102** 1423 (1956)

[41]. A. P. Malozemoff, Phys. Rev. B **35** 3669 (1987)

[42]. A. P. Malozemoff, Phys. Rev. B **37** 7673 (1988)

[43]. D. Mauri, H. C. Siegmann, P. S. Bagus, E. Kay, J. Appl. Phys **62** 3047 (1987)

[44]. Z. B. Guo, K. B. Li, G. C. Han, Z. Y. Liu, P. Luo, Y. H. Wu, J. Magn. Magn. Mater. **251** 323 (2005)

[45]. J. Ding, J. G. Zhu, J. Appl. Phys. **79** 5892 (1996)

[46]. J. Sort, B. Dieny, M. Fraune, C. Koening, F. Lunnebach, B. Beschoten, G. Güntherodt, Appl. Phys. Lett. **84** 3696 (2004)

[47]. M. Fraune, U. Rüdiger, G. Güntherodt, C. Cardoso, P. Freitas, Appl. Phys. Lett. **77** 3815 (2000)

[48]. Y. Shen, Y. Wu, H. Xie, K. Li, J. Qiu, Z. Guo, J. Appl. Phys. **91** 8001 (2000)

[49]. A. Nemoto, Y. Otani, S. G. Kim, K. Fukamichi, Appl. Phys. Lett. **74** 4026 (1999)

[50]. T. Ambrose, C. L. Chien, J. Appl. Phys. **83** 7222 (1998)

[51]. C. Tsang, N. Heiman, K. Lee, J. Appl. Phys. **52** 2471 (1981)

[52]. D. Bedau, "Domain wall dynamics in magnetic nanostructures", PhD thesis, University of Konstanz (2008)

[53]. J. Briaire, "1/f noise in Permalloy", PhD thesis, Eindhoven University of Technology (2000)

[54]. C. Kittel, "Introduction to Solid State Physics", John Wiley & Sons (2005) page 342

[55]. G. H. Yu, C. L. Chai, F. W. Zhu, J. M. Xiao, W. Y. Lai, Appl. Phys. Lett. **78** 1706 (2001)

[56]. D. H. Han, J. G. Zhu, J. H. Judy, M. Sivertsen, J. Appl. Phys. **81** 4996 (1997)

[57]. D. B. Williams, C. B. Carter, “Transmission Electron Microscopy: A Textbook for Material Science”, Springer (2009)

[58]. P. M. Martin, “Handbook of Deposition Technologies for Thin Films and Coatings”, Elsvier Inc. USA (2005)

[59]. R. F. Egerton, “Physical Principles of Electron Microscopy”, Springer, USA (2005)

[60]. “Magnetic properties measurement system: Reciprocating Sample Option User’s Manual; 1090-100C”, Quantum Design, USA

[61]. J. Clarke, A. I. Braginski, “The SQUID Handbood Vol. 1”, Wiley VCH, Weinheim (2004)

[62]. S. Tumanski, “Handbook of Magnetic Measurements”, CRC Press (2011)

[63]. J. G. Webster, “The Measurement Instrumentation and Sensors Handbook” CRC Press (1999)

[64]. M. McElfresh, “Fundamentals of Magnetism and Magnetic Measurements”, Quantum Design, USA (1994)

[65]. “Variation of Magnetic Field over the Scan Length 1014-204”, Quantum Design, USA

[66]. “MPMS MultiVu Application User’s Manual” Quantum Design, USA

[67]. Y. Liu, D. J. Sellmyer, D. Shindo, “Handbook of Advanced Magnetic Materials: Vol. 1”, Springer, USA (2006)

[68]. D. Martien, “Introduction to AC Susceptibility”, Quantum Design, USA

[69]. V. Stanciu, I. L. Soroka, J. Lu, B. Hjörvarsson, P. Nordblad, J. Magn. Magn. Mater. **286** 446 (2005)

[70]. X. G. Zheng, C. N. Xu, K. Nishikubo, K. Nishiyama, W. Higemoto, W. J. Moon, E. Tanaka, E. S. Otabe, Phys. Rev. B **72** 014464 (2005)

[71]. M. Molina-Ruiz, A. F. Lopiandía, F. Pi, D. Givord, O. Bourgeois, J. Rodríguez-Viejo, Phys. Rev. B **83** 140407 (2011)

[72]. J. I. Martín, J. Nogués, Kai Liu, J. L. Vicent, I. K. Schuller, J. Magn. Magn. Mater. **256** 449 (2003)

[73]. A. Yamaguchi, A. Hirohata, T. Ono, H. Miyajima J. Phys.: Condens. Mater. 24 024201 (2012)

[74]. J. Nogués, J. Sort, V. Langlais, V. Skumryev, S. Suriñach, J. S. Munoz, M. D. Baró, Phys. Reps. **422**, 65 (2005)

[75]. B. K. Kuanr, , V. Veerakumar, L. M. Malkinski, A. V. Kuanr, R. E. Camley, Z. Celinski, IEEE Trans. Magn. **45** 3550 (2009)

[76]. J. McCord, L. Schultz, J. Fassbender, Adv. Mater. **20** 2090 (2008)